

POLITECNICO DI TORINO



Master's Degree in Aerospace Engineering
Department of Mechanical and Aerospace Engineering

MASTER'S DEGREE THESIS

Development of a tool for thermal analysis of small spacecraft

Candidate:

Francesco Lucia

Thesis Supervisor:

Prof. Sabrina Corpino

July 2023

Abstract

Recent years have seen a growing interest in space missions involving small satellites. This attraction is due to their relative ease of production, low cost and short development time, making them accessible to a wide range of organizations, including universities, research institutes and commercial entities.

Ensuring the reliability of these systems is becoming increasingly important, with thermal analysis and thermal design, in particular, playing a crucial role in all phases of project development to keep each satellite component within temperature limits to ensure proper operation.

This thesis aims to develop a tool implemented in the MATLAB® environment, known as the Small Satellites Thermal Tool (S2T2), created by the Department of Mechanical and Aerospace Engineering at the Politecnico di Torino. The tool provides support for both thermal analysis and design in the early phases of a space project.

In particular, this thesis focuses on the Geometric Math Model (GMM), whose scope is to provide a geometric representation of the satellite, defining its surfaces, and node distribution, assigning optical and mechanical properties to each component and calculating the radiative coupling between the spacecraft surfaces. The GMM is the first step in building the satellite's thermal model.

To make the tool comparable with commercial software, several improvements have been made to the GMM. New 2D and 3D geometries were implemented and the capability to model deployable solar panels has been introduced. This expansion enables a more comprehensive representation of the satellite's configuration, supporting detailed thermal analyses.

To improve the accuracy of radiative heat exchange calculations between surfaces, the concept of reflection has been introduced within the Monte Carlo Ray-Trace method for determining the view factors.

In addition, efforts were made to make the code modular and more efficient, facilitating integration with future work. The GUI of the GMM module was also modified to improve ease of use.

To verify its reliability, the tool was tested and compared with results obtained from Thermal Desktop by Cullimore & Ring Technology, a commercial software widely used in the space industry. As a case study, the tool was used in the early stages of the Spei Satelles space mission to support design decisions.

Contents

1. Introduction.....	13
What is a small spacecraft?	13
What is the thermal control system?.....	14
Objectives	15
2. Thermal Analysis.....	18
Thermal-Electrical Analogy	19
Conduction.....	21
Radiation.....	23
General Heat Transfer Equation	24
Finite-Difference Method (FDM).....	25
View Factor Calculation.....	28
Monte Carlo Ray-Trace Method.....	29
Gebhart's method.....	32
Monte Carlo Ray-Trace with reflection.....	33
Environmental Analysis	35
Solar Direct.....	35
Albedo.....	36
Planet IR and spacecraft IR emission	38
3. Small Satellite Thermal Tool (S2T2).....	39
Software Architecture.....	39
GMM Updates	41
GMM Layout.....	42

Structure Tab.....	43
Solar panels and boards tab.....	44
Parallelepipeds Tab.....	46
Cylinder tab.....	47
Preview and Update GMM Button	49
Calculate View Factor Button	59
MCRT New Version First Iteration	61
MCRT New Version Second Iteration.....	66
MCRT Reflection Tab	68
Introduction of Reflection.....	69
Comparison with the previous version	70
4. Validation and Case Study.....	74
Comparison with Thermal Desktop.....	74
Board.....	75
Parallelepiped.....	78
Solar Panel	84
Spei-Satelles Mission	88
Mission Objectives	88
Mission Phases	88
Spacecraft Architecture and Configuration	90
Thermal Analysis.....	93
Requirement Temperatures.....	93
Cold Case and Hot Case	93
Optical/Thermophysical Properties	95
S2T2 Additional Conduction/Dissipations Plot.....	98
Comments and Results	99
Design Optimization.....	104
Final Iteration with TD and Results	109

Data from Orbit	113
5. Conclusions.....	119
6. References.....	123

List of Figures

Figure 1: SmallSats in Context, Spacecraft Launched 2013 – 2022, by Mass Class [3]	14
Figure 2: SmallSats in Context, Smallsats 2013 – 2022, by Mass Class [3] ..	14
Figure 3: Main function in the thermal analysis process	18
Figure 4: Nodalization.....	20
Figure 5: Passage from GMM to TMM	21
Figure 6: Conduction conductor [7]	22
Figure 7: Example of multiple conductors' thermal path [7].....	22
Figure 8: Serial path equivalent conductance [8].....	23
Figure 9: Parallel path equivalent conductance [8].....	23
Figure 10: Radiation conductor.....	24
Figure 11: 1D computational molecule (up), 2D computational molecule (down).....	26
Figure 12: Radiation between two surfaces	28
Figure 13: Ray tracing, N is the number of rays emitted, m is the number of rays absorbed	29
Figure 14: Definition of a plane surface [9]	30
Figure 15: The disposition of the radiation incident on surface.....	31
Figure 16: The diffuse reflection model [9]	34
Figure 17: Fence problem [12].....	34
Figure 18: Gebhart method (left), MCRT with reflection (right) [12].....	34
Figure 19: Environmental heat fluxes	35
Figure 20: Aphelion and Perihelion heat flux	36
Figure 21: Solar and room-temperature-body spectral distribution [7]	36
Figure 22: Albedo factor values	38
Figure 23: S2T2 architecture.....	40

Figure 24: GMM high-level Architecture	41
Figure 25: GMM structure module Layout	44
Figure 26: Solar Panels Tab Layout	45
Figure 27: Default 2D Surface Definition.....	45
Figure 28: Boards Tab Layout	46
Figure 29: Parallelepipeds Tab Layout	47
Figure 30: Cylinder Tab Layout.....	48
Figure 31: Cylinder Default Representation	49
Figure 32: Cylinder areas calculation.....	49
Figure 33: GMM flowchart.....	50
Figure 34: GMM All items	51
Figure 35: Node Creator Flowchart	52
Figure 36: Example of Node Cases.....	53
Figure 37: Lexicographic Sorting 2D.....	53
Figure 38: Example of connectivity matrix.....	58
Figure 39: Examples of nodal connection box (left), board (right)	58
Figure 40: Examples of nodal connection parallelepiped (left), cylinder (right)	59
Figure 41: MCRT Wait bar	60
Figure 42: MCRT Evolution	60
Figure 43: Single emission point (left), random emission points (right)	62
Figure 44: Random points within surface	63
Figure 45: Ray direction definition [14]	63
Figure 46: Hemispherical distribution, non-uniform (left), uniform (right) ...	64
Figure 47: Spherical distribution, non-uniform (left), uniform (right)	65
Figure 48: Left the point is inside; Right the point is outside [14]	65
Figure 49: MCRT New Version First Iteration Flowchart.....	66
Figure 50: MCRT New Version Second Iteration Flowchart	67

Figure 51: MCRT with Reflection Tab Layout.....	68
Figure 52: MCRT with Reflection Flowchart	70
Figure 53: GMM Model for MCRT Comparison	71
Figure 54: Orbit representation S2T2 (left), TD (right).....	75
Figure 55: Board comparison S2T2 (left), TD (right).....	75
Figure 56: Board temperature trend comparison.....	76
Figure 57: Board with dissipation comparison S2T2 (left), TD (right)	76
Figure 58: Board with dissipation temperature trend comparison	76
Figure 59: Board with additional conduction comparison S2T2 (left), TD (right)	77
Figure 60: Board with additional conduction temperature trend comparison.	77
Figure 61: Board with dissipation and additional conduction temperature trend comparison.....	77
Figure 62: Parallelepiped comparison S2T2 (left), TD (right).....	78
Figure 63: Parallelepiped temperature trend comparison	79
Figure 64:Parallelepiped with dissipation comparison S2T2 (left), TD (right)	79
Figure 65: Parallelepiped with dissipation temperature trend comparison	79
Figure 66: Parallelepiped with additional conduction comparison S2T2 (left), TD (right).....	80
Figure 67: Parallelepiped with additional conduction temperature trend comparison.....	80
Figure 68: Parallelepiped with dissipation and additional conduction temperature trend comparison	80
Figure 70:Cylinder comparison S2T2 (left), TD (right)	81
Figure 71: Cylinder temperature trend comparison	82
Figure 72: Cylinder with dissipation comparison S2T2 (left), TD (right).....	82
Figure 73: Cylinder with dissipation temperature trend comparison.....	82
Figure 74: Cylinder with additional conduction comparison S2T2 (left), TD (right)	83

Figure 75: Cylinder with additional conduction temperature trend comparison	83
Figure 76: Cylinder with dissipation and additional conduction temperature trend comparison.....	84
Figure 77: Solar panel comparison S2T2 (left), TD (right)	84
Figure 78: Solar panel temperature trend comparison	85
Figure 79: Solar panel with dissipation comparison S2T2 (left), TD (right)..	85
Figure 80: Solar panel with dissipation temperature trend comparison.....	85
Figure 81: Solar panel with additional conduction comparison S2T2 (left), TD (right)	86
Figure 82: Solar panel with additional conduction comparison S2T2 (left), TD (right)	86
Figure 83: Solar panel with dissipation and additional conduction temperature trend comparison.....	86
Figure 84: Spei Satelles operations timeline	90
Figure 85: Final configuration of SPEISAT	90
Figure 86: Spei Satelles architecture	91
Figure 87: Internal view of faces -Y (left), +Y (central), +X (right)	92
Figure 88: Cold Case Orbit (left), Hot Case Orbit (right).....	94
Figure 89: Lateral face with each layer modelled	96
Figure 90: In-plane verses Out-plane	97
Figure 91: Additional conduction (left), Cold case dissipation (middle), Hot case dissipations (right)	99
Figure 92: Temperature trends comparisons, cold case (left) and hot case (right)	100
Figure 93: External heat map, Cold case (left), Hot case (right)	103
Figure 94: Internal heat map, Cold case (left), Hot case (right).....	103
Figure 95: External-Internal view heat map, Cold case (left), Hot case (right)	103

Figure 96: First two objectives (distance from optimal temperatures and total heater power) of the final Pareto fronts generated by RVEA, MOEA/D and RSA in the SpeiSat optimization.	105
Figure 97: Performance metrics of the 3 algorithms used in the SpeiSat design optimization.	106
Figure 98: 2-dimensional representation of the approximated true Pareto front for the SpeiSat design optimization. The data points correspond to the non-dominated solutions, across all algorithms.	107
Figure 99: 3-dimensional representation of the approximated true Pareto front for the SpeiSat design optimization. The data points correspond to the non-dominated solutions, across all algorithms.	107
Figure 100: Project phases for TCS	109
Figure 101: TD model for last iteration, external (left), internal (right)	111
Figure 102: Comparison between TD model (left) and CAD model (right) about primary and secondary structure	111
Figure 103: Min-Max results, Cold case (left), Hot case (right).....	112
Figure 104: Temperature trends for Cold case.....	113
Figure 105: Temperature trends for Hot case.....	113
Figure 106: Telemetry data point received from SpeiSat between June 25, 2023, and July 12, 2023.	114
Figure 107: Temperature difference between the battery and its secondary structure support elements	115
Figure 108: Temperature difference between C&DH1 and its secondary structure support element.	115
Figure 109: Temperature difference between C&DH2 and its secondary structure support element.	116
Figure 110: Temperature trends of SpeiSat Battery and Battery Stiffener. Data recorded on July 13, 2023.....	116
Figure 111: Temperature trends of SpeiSat C&DH1 and C&DH1 Shelf. Data recorded on July 13, 2023.....	117
Figure 112: Temperature trends of SpeiSat C&DH2 and C&DH2 Shelf. Data recorded on July 13, 2023	117

Figure 113: Temperature trends of SpeiSat ComSys1 and ComSys2. Data recorded on July 13, 2023117

List of Tables

Table 1: Thermal-Electrical analogy [7]	19
Table 2: Typical Orbit-Average Earth IR and Albedo values [13]	37
Table 3: Item properties	42
Table 4: Structure face numbering	43
Table 5: Examples of three board cases	54
Table 6: Item cases	57
Table 7: Numbering of conductive areas	57
Table 8: Environment Parameters for MCRT Comparison	71
Table 9: GMM Parameters for MCRT Comparison	71
Table 10: Comparison in MCRT Run Time.....	72
Table 11: Comparison of all the MCRT algorithm version with TD.....	72
Table 12: Orbit parameters for item comparison	74
Table 13: Board results	78
Table 14: Parallelepiped results	81
Table 15: Cylinder results	84
Table 16: Solar panel results	87
Table 17: SPEI SATELLES High-level ConOps.....	89
Table 18: List of components.....	92
Table 19: Temperature requirements	93
Table 20: Cold case and Hot case environment and attitude data.....	94
Table 21: Recharge and Payload modes power consumption.....	95
Table 22: Materials optical properties.....	96
Table 23: Material mechanical properties	97
Table 24: Materials assigned to each component.....	98
Table 25: Modelled items with S2T2.....	98

Table 26: Cold case results.....	101
Table 27: Hot case results	102
Table 28: Optical properties of the final optimized solution chosen for SpeiSat.	108
Table 29: Heater power in the final optimized solution chosen for SpeiSat.	108
Table 30: Difference between S2T2 and TD models	110

List of Acronym

BoL	Beginning of Life
CNR	Consiglio Nazionale Delle Ricerche (National Research Council)
C&DH	Command & Data Handling
CoM	Centre of Mass
ComSys	Communication System
ConOps	Concept of Operations
DC	Duty Cycle
DET	Direct Energy Transfer
EPS	Electrical Power System
FDM	Finite Difference Model
FR4	Flame Retardant Level 4
GMM	Geometric Math Model
GMT	Greenwich Mean Time
GUI	Graphical User Interface
HL	Hard Limit
HR	Hypervolume Ratio (metric)
HV	Hypervolume
IGD	Inverted Generational Distance (metric)
ID	Identifier
IMU	Inertial Measurement Unit
IR	Infrared
LB	Lower Bound
LEO	Low Earth Orbit
LV	Launch Vehicle
MCC	Mission Control Centre
MCRT	Monte Carlo Ray Tracing
MOEA/D	Multi-objective Evolutionary Algorithm based on Decomposition (algorithm)
MOO	Multi-Objective Optimization
MOOP	Multi-Objective Optimization Problem
MOPSO	Multi-Objective Particle Swarm Optimization (algorithm)
MPFE	Maximum Pareto Front Error (metric)
MS	Maximum Spacing (metric)
NGSA	Non-dominated Sorting Genetic Algorithm (algorithm)
PCB	Printed Circuit Board
RSA	Reference point based archived many objective simulated annealing (algorithm)
RVEA	Reference Vector Guided Evolutionary Algorithm for Many-Objective Optimization (algorithm)
SL	Soft Limit
SP	Spacing (metric)
S/C	Spacecraft
S2T2	Small Satellite Thermal Tool
TCS	Thermal Control System

TD	Thermal Desktop
TMM	Thermal Math Model
UB	Upper Bound
UI	User Interface

List of Symbols

\dot{Q}_p	Planet heat rate
\dot{Q}_s	Solar heat rate
\dot{Q}_{sp}	Heat rate dissipated to the space
C_p	Specific Heat
C_s	Solar constant
\dot{Q}	Heat-rate
F_{ecl}	Eclipse factor
F_p	Spacecraft to Planet View Factor
F_{sp}	Spacecraft to Space View Factor
A	Area
B	Grey body view factor
C	Capacitance
e	Eccentricity
F	Geometric view factor
G	Conductor
i	Inclination
K	Conductivity
L	Length or Distance
P	Power consumption
Q	Heat
T	Temperature
t	time
V	Volume
α	Absorptivity coefficient
ε	Emissivity coefficient
ρ	Density
σ	Stefan-Boltzmann constant
Ω	Ray Direction
ξ	Random number
ζ	Radiation exchange between two surfaces

Chapter 1

Introduction

What is a small spacecraft?

Small satellites are a class of artificial satellites that are small in size and weight. Typically, these satellites measure from a few centimetres to a few meters in length and can weigh from a few grams to 600 kilograms. Despite their compact size, small satellites offer numerous opportunities and advantages in various fields, including scientific research, space engineering and space economy [1].

From the point of view of scientific research, small satellites make it possible to conduct experiments in space at significantly lower costs than conventional large satellites. This opens the way to greater accessibility for researchers worldwide, allowing them to conduct research and observations in various fields such as astronomy, Earth observation, climatology and biology. In addition, the use of fleets of small satellites can enable more comprehensive global coverage to monitor natural phenomena, environmental changes and disasters.

From a space engineering perspective, small satellites offer the possibility of testing new technologies and methods at reduced costs. Their compact size simplifies the design, development and launch process, allowing engineers to test innovative solutions in a shorter time. This encourages the rapid iteration and evolution of space technologies, contributing to the continued growth and development of the aerospace industry [2].

In terms of space economics, small satellites have been a key factor in making space an accessible environment for small businesses and start-ups. Lower launch costs and evolving technologies have enabled emerging companies to develop and put into orbit constellations of small satellites to provide innovative services such as global telecommunications, natural resource monitoring, Internet connectivity and more. This growing commercial space industry is generating new job opportunities and contributing to the creation of a sustainable space economy.

This trend is supported by recent data, looking at Figure 1 it is evident how a very high share of the current spacecraft upstream sector is devoted to the design. Launch and operation of Small Sats, with few commercial constellations giving the highest contribution to these numbers [3].

Figure 2 analyses in more detail the distribution of the total SmallSats by Mass Class. The Starlink and OneWeb constellations make up the majority of satellites, with spacecraft in the range of a few hundred kilograms of mass.

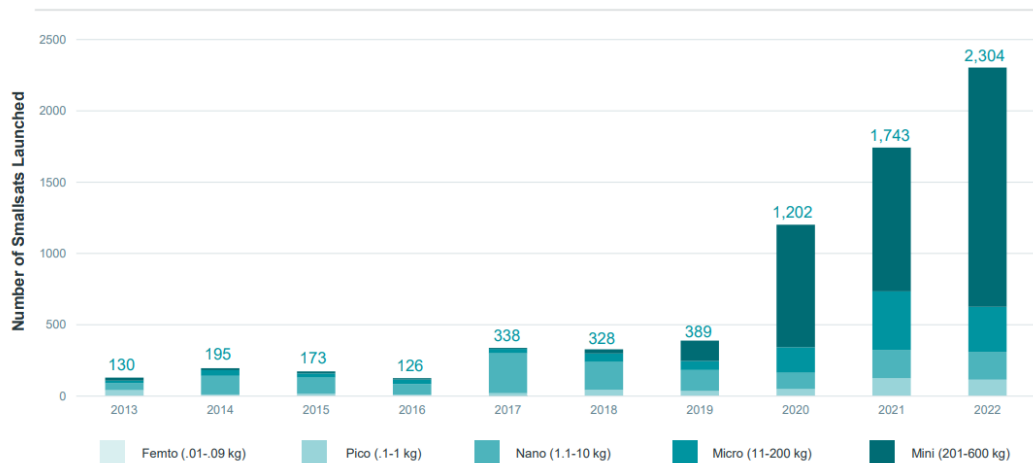


Figure 1: SmallSats in Context, Spacecraft Launched 2013 – 2022, by Mass Class [3]

In summary, small satellites offer several significant advantages. Their compact size, low cost and operational flexibility make them valuable tools for exploring our planet, conducting scientific experiments, developing new space technologies and stimulating economic growth in space [2].

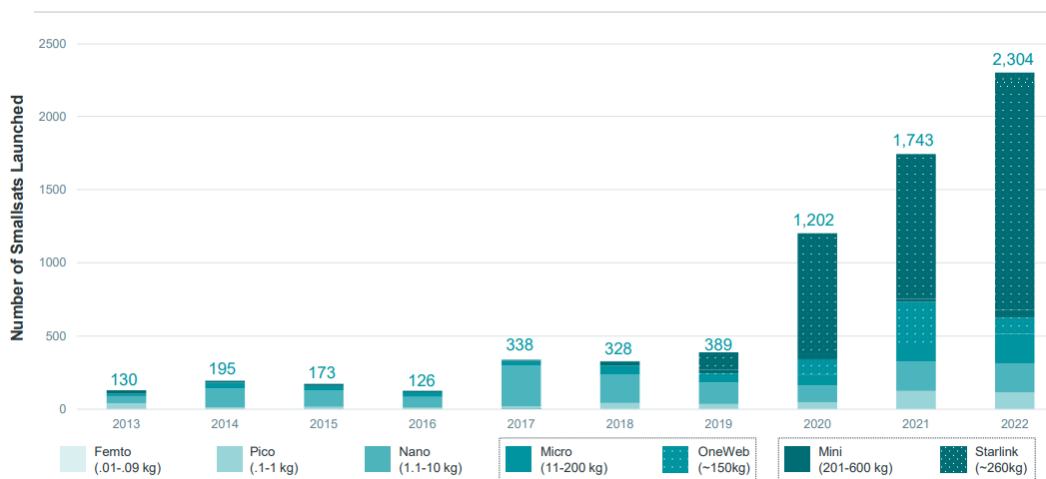


Figure 2: SmallSats in Context, Smallsats 2013 – 2022, by Mass Class [3]

What is the thermal control system?

The thermal control system is responsible for implementing temperature control, it is present on board all satellites and spacecraft in general, it is necessary to keep the equipment, especially the electronics, within certain temperature ranges so that they can operate efficiently and reliably. In addition, it is necessary to control temperatures to prevent structural stresses due to the different coefficients of thermal expansion of materials.

Implementing thermal control of a system means making an energy balance, i.e., seeking an equilibrium between the heat absorbed from the outside, and possibly that generated by the system itself, and that emitted to the outside.

The first step is to define the thermal requirements and any existing constraints for our design, which derive from the thermal requirements of the various components installed on board and the characteristics of the satellite, as well as the mission phases in which the satellite operates. We then move on to determine the thermal environment, i.e., calculate all the heat flows that the satellite will receive from the external environment.

The next step is the definition of the thermal system architecture and all the design choices to be implemented in the system design.

All the previous steps are then iterated to converge and define the optimal design for the thermal control system. So, the thermal engineer deals with three macro areas:

- **Analysis:** downstream of the knowledge of all the components of the system and the space environment in which it operates, calculate the temperatures that the subsystems and the structure reach and compare them with the limits imposed by requirements and constraints.
- **Design:** design of the thermal control system, looking for solutions that allow the components to operate within their operative ranges.
- **Verification:** in the initial stages of the project, this is carried out through analysis and simulations, while the subsequent stages are carried out experimentally to qualify and accept the system for launch. These phases are typically costly and require special facilities to be carried out, such as vacuum chambers and thermal cycling chambers.

The thermal control system must be able to manage the system's temperatures during all phases of the mission, which cover not only all on-orbit operations but also all pre-launch phases and even the launch phase itself.

Objectives

The importance of small satellites in the world of scientific research and space engineering is currently growing, and with it also the complexity of space systems and also of the missions themselves, which require increasingly complex payloads with ever more stringent requirements [1].

In this context, the work of the engineer is, therefore, crucial to ensure the maximum reliability of these platforms. One of the areas in which technological research is investing is precisely thermal management. The increasingly complex technologies with which small satellites are equipped have increasingly restrictive thermal requirements [2].

To support thermal analysts in this work, many tools have been developed and have become indispensable in the design cycle of a space product. Among the most important and widely used are

ESATAN-TMS® and THERMAL DESKTOP®. Both allow the creation of very accurate and detailed thermal models that achieve a high degree of accuracy in temperature calculations. Using these software packages, however, is not always straightforward, their operation takes some time to learn, and even a simple model still requires a certain amount of work to be implemented. Information and data are often scarce, especially in the early stages of a space project, this does not allow the full potential of the above-mentioned tools to be exploited. Being commercial products, high license costs are required to use these software packages.

It is precisely to address all these disadvantages and to support the analyst in the early design stages of a thermal system that the software called 'Small Satellite Thermal Tool' or S2T2 was created. The creator of this tool is Daniele Calvi, who worked on its development during his PhD thesis. The objectives of his work were:

1. To develop a thermal analysis tool tailored to small space platforms, for the early design stage of a space mission.
2. To develop solutions for the thermal management system of small platforms driven by the thermal analysis results.

The tool was entirely developed in the MATLAB® environment and allows the user, with a few preliminary data, to perform an accurate thermal analysis, and proposes, through optimization algorithms, passive design solutions for the thermal control system. The software features a graphical interface and is very intuitive and easy to use. In Daniele Calvi's PhD thesis [4], there are numerous case studies for which he uses this tool with excellent results.

The first version of this tool, however, had several limitations:

- The form factor that could be implemented to represent the spacecraft structure was only the standard CubeSat form factor, proposed by the CubeSat Design Specification [5].
- The implementable geometries for constructing the model were limited to only two-dimensional board-type elements.
- The calculation of the radiative coupling between the surfaces had a certain degree of error due to the algorithm for calculating the view factors.
- The objective function implemented within the code was inefficient and took too long to execute.
- The design techniques used were not those suggested by the state of the art.

The work set out in this thesis has the above-mentioned limitations as its starting points, and aims to develop a new version of S2T2, including the following improvements:

1. Allowing the user to arbitrarily decide the size of the satellite structure.
2. Introduce new geometries in the code that also allow elements outside the spacecraft to be represented.
3. To improve the calculation of view factors by also introducing the reflection phenomenon.

Secondary objectives are, on the other hand, to improve the usability of the tool by intervening on the graphical interface, and to reduce the waiting time for obtaining results, thus carrying out optimization work on some of the algorithms implemented within the code.

The remaining points will be dealt with in another thesis, parallel to this one, whose author is Davide Cosenza [6].

Chapter 2

Thermal Analysis

The purpose of this chapter is to provide the main mathematical and theoretical instruments useful for carrying out the thermal analysis of a satellite. The purpose of thermal analysis is to determine the temperatures on board the spacecraft by solving the heat transfer equation.

The general process of thermal analysis can be schematized in Figure 3.

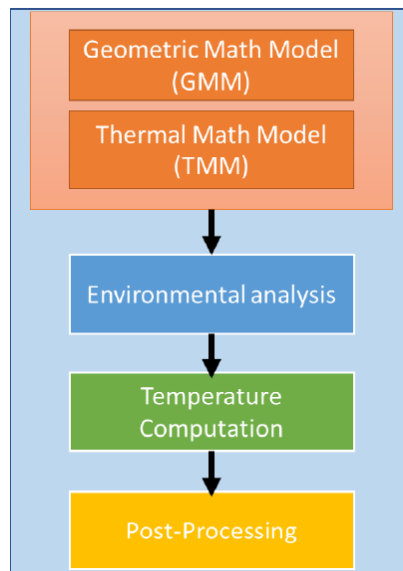


Figure 3: Main function in the thermal analysis process

The first step is the creation of two models, the Geometric Math Model (GMM) and the Thermal Math Model (TMM). The first model represents the geometry of the system with also the subdivision into nodes, the second model, using the thermo-electric analogy, defines the thermal paths that heat follows.

The environmental analysis allows the heat fluxes from outside the satellite to be determined. It will be explained below how each external contribution depends on specific factors.

Once these inputs are collected, the heat equation is solved using the finite difference method (FDM), whereby partial derivatives are approximated by finite differences using Taylor series development.

Thermal-Electrical Analogy

The purpose of this subchapter is to introduce the concepts on which thermal modelling is based; in particular, a good model achieves a high degree of accuracy but with a low computational cost. To do this, it is necessary to introduce the concept of analogy between two different systems, specifically the thermal system and the electrical system. Two systems are said to be analogous when they are described by similar equations and boundary conditions. In this case, it is possible to use the characteristic equations of one of the systems to describe the other simply by changing the symbols of the variables [7].

Table 1 groups the analogous equations for the two systems.

Quantity	Thermal System	Electrical System
Potential	T	E
Flow	\dot{Q}	I
Resistance	R	R
Conductance	G	1/R
Capacitance	C	C
Ohm's Law	$\dot{Q} = GT$	$I = E/R$

Table 1: Thermal-Electrical analogy [7]

This analogy makes it possible to use some basic electrical laws such as Ohm's law and Kirchoff's law to solve temperature distributions and gradients of complex physical thermal networks.

The starting point for creating a thermal network is the concept of the node. The thermal system is divided into a series of sub-volumes called nodes and all thermal properties present within the sub-volume are concentrated in the node [7].

Each node is characterized by two quantities:

- The temperature, T, or potential in the thermal system, represents the average temperature of the sub-volume.
- The thermal mass, C, or the capacitance, is derived from the thermophysical properties of the material constituting the sub-volume.

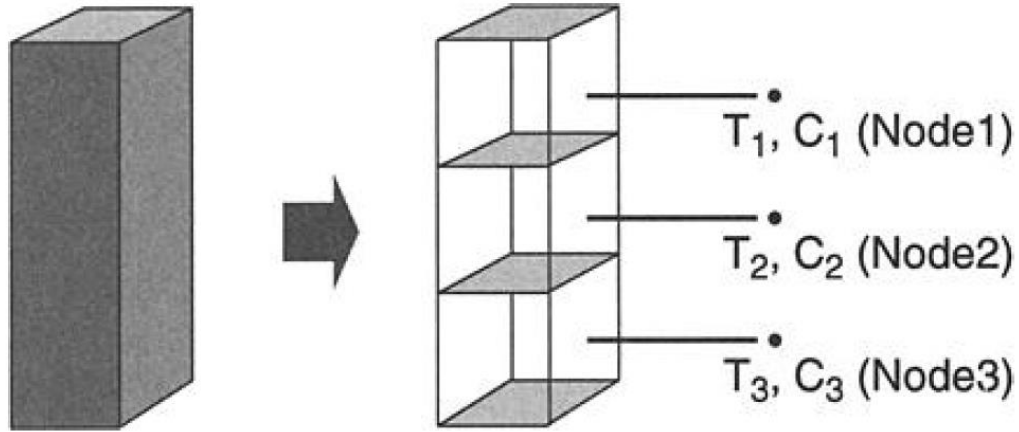


Figure 4: Nodalization

At this point, it is necessary to define the types of nodes needed to define the thermal network [7]:

- Diffusion node with a finite thermal mass
- Arithmetic node with zero thermal mass
- Boundary node with infinite thermal mass

The diffusion node is used to represent normal material, its temperature can either increase or decrease depending on the capacity, the net heat flux entering the node and the time it takes for the heat flux to enter the node. Mathematically is defined by this expression:

$$\sum \dot{Q} - \frac{C\Delta T}{t} = 0 \quad (1)$$

Arithmetic nodes have no real physical meaning, they can be used to represent elements of the system that have a negligible heat capacity compared to others. The temperature of an arithmetic node responds instantaneously to its surroundings. They have the following mathematical expression:

$$\sum \dot{Q} = 0 \quad (2)$$

The boundary node is used to represent the elements in the model that have a much greater heat capacitance than the others, their temperature does not vary even though they exchange heat with other nodes in the model. In particular satellite thermal models, they used to represent the deep-space sink temperature or the planet's surface temperature. Mathematically they are defined as:

$$T = constant \quad (3)$$

The heat capacitance of diffusive nodes can be calculated using the following formula:

$$C = \rho * V * C_p \quad (4)$$

Where ρ is the density [kg/m^3], V is the volume [m^3] and C_p is the specific heat [$J/(kg^\circ C)$].

The last concept to be introduced is the conductor, which is the mathematical representation of the heat flow paths through which energy is transferred from one node to another.

The three processes by which heat passes from a region with a higher temperature to regions with a lower temperature are conduction, convection, and radiation. In most thermal models inherent in the study of satellites, the prevailing heat transfer mechanisms are conduction and radiation, since in space fluids, if present, are confined within tanks.

Figure 5 shows the transition from a geometric representation of nodes, expressed by the GMM, to a thermal network representation, expressed by the TMM.

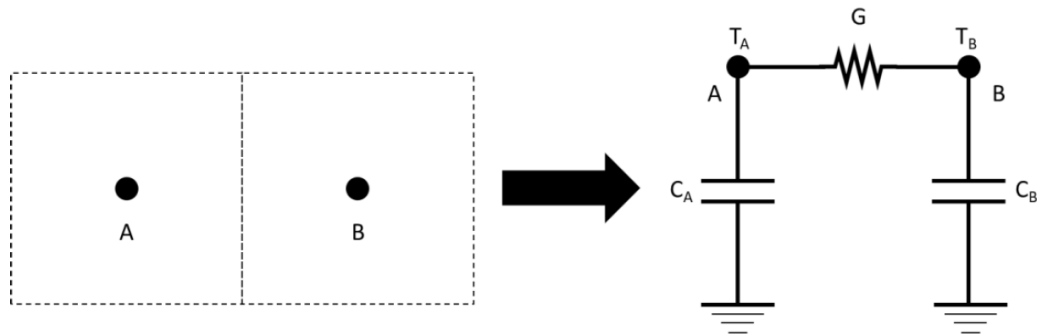


Figure 5: Passage from GMM to TMM

Conduction

Conduction is the process by which heat flows within a medium or between different mediums in direct physical contact, and the heat is transmitted by molecular communication.

Conductors that represent conduction paths are referred to as linear conductors because, for those paths, the heat-flow rate is a function of the temperature difference between nodal temperatures to the first power.

$$\dot{Q} = G_{ij}(T_i - T_j) \quad (5)$$

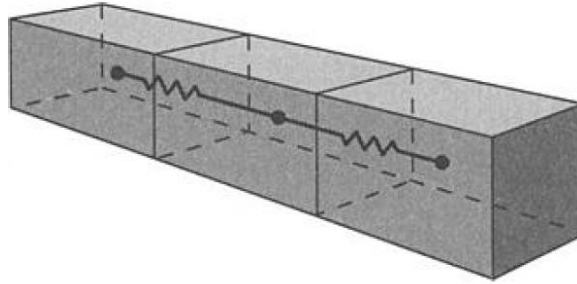


Figure 6: Conduction conductor [7]

The thermal conductance G [$W/^\circ C$] can be calculated through the following formula

$$G = \frac{k * A}{L}$$

(6)

Where k is the thermal conductivity of the material [$K/(m * K)$], A is the cross-section through which heat flows from one node to another [m^2], L is the length of the path that the heat makes [m].

In the case of heat paths formed by multiple materials in contact with each other, as shown in Figure 7, the analogy with electrical circuits can be used to identify an equivalent conductivity [8].

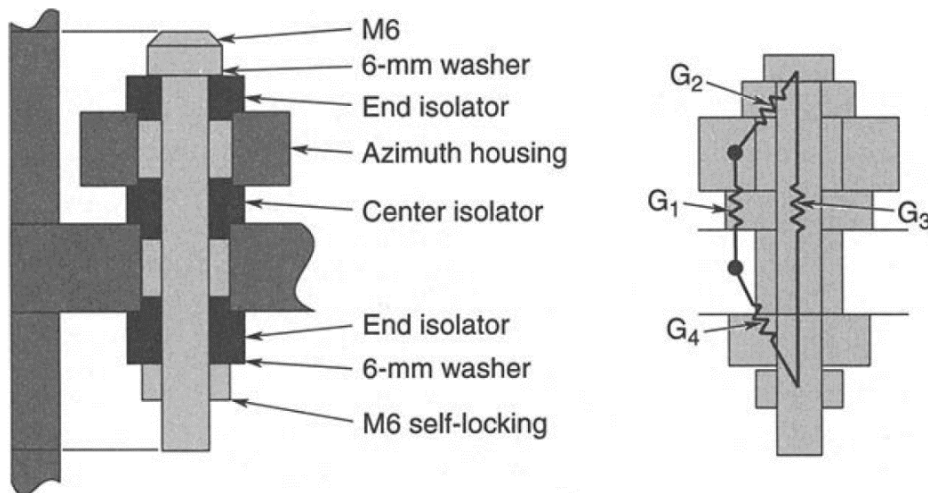


Figure 7: Example of multiple conductors' thermal path [7]

Serial paths:

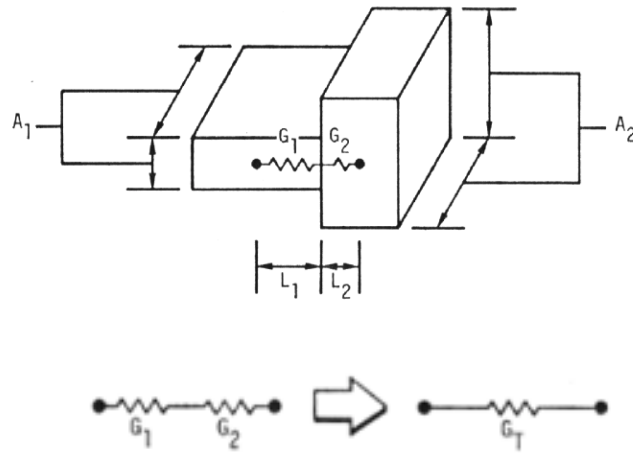


Figure 8: Serial path equivalent conductance [8]

$$\frac{1}{G_T} = \frac{1}{G_1} + \frac{1}{G_2} + \dots + \frac{1}{G_i}$$

(7)

Parallel paths

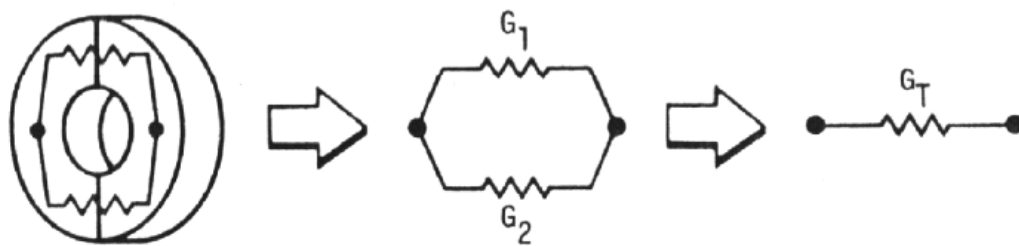


Figure 9: Parallel path equivalent conductance [8]

$$G_T = G_1 + G_2 + \dots + G_i$$

(8)

Radiation

Radiation, through the phenomenon of electromagnetic waves, is a process of energy transfer between two separate bodies in space as shown in Figure 10. Conduction by radiation is a nonlinear phenomenon the heat flow between two surfaces depends on the difference in temperatures elevated to the fourth power [7].

$$\dot{Q} = G_{ij}(T_i^4 - T_j^4)$$

(9)

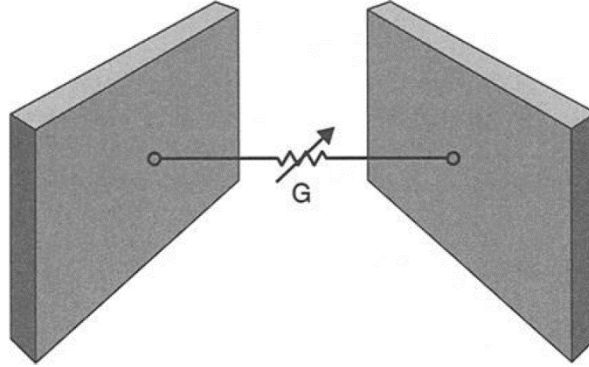


Figure 10: Radiation conductor

Radiative conductance can be written through two expressions:

$$G_{1-2} = A_1 * \varepsilon_1 * F_{1-2} * \sigma \text{ for radiation to a blackbody}$$

(10)

$$G_{1-2} = A_1 * \varepsilon_1 * B_{1-2} * \sigma \text{ for radiation between grey surfaces}$$

(11)

Where σ is the Stefan-Boltzmann constant with a value of $5.669 \times 10^{-8} [W/(m^2 * K^4)]$, ε_1 is the emittance of surface 1, A_1 is the radiative area of the surface 1 [m^2], F_{1-2} is the geometric view factor without reflection and B_{1-2} is the gray-body radiation view factor

It is now necessary to linearize equation (9) to ensure the analogy of the thermal system with the electrical system, in particular the term $(T_i^4 - T_j^4)$ is factored into $(T_i^3 + T_i T_j^2 + T_i^2 T_j + T_j^3)$ and $(T_i - T_j)$. Then the term $(T_i^3 + T_i T_j^2 + T_i^2 T_j + T_j^3)$ is evaluated by the computer code for each time-step using the current values of T_i and T_j . The quantity thus obtained is then multiplied by the input value of the radiation conductor, thus reducing the radiation equation to a linear form [7].

General Heat Transfer Equation

Solving the general heat-transfer equation is the purpose of all thermal-analysis codes in the spacecraft industry. The general partial differential equation of heat conduction with source term for a stationary heterogeneous, anisotropic solid is [7]:

$$\rho C_p \frac{\partial T}{\partial t} = \nabla * (K * \nabla T) + \dot{Q}(T, t)$$

(12)

Where ρ is the material density [kg/m^3], C_p is the material specific heat [$J/(kg * K)$], K is the material conductivity [$K/(m * K)$], T is the temperature [$^{\circ}K$], it is a scalar quantity and it can vary with position $T = (x, y, z, t)$, t is the time [s], \dot{Q} is the source term [W/m^3], it contains both the power dissipated by the internal components and the satellite's heat exchanges with the external environment and $q = -K * \nabla T$ is the Fourier conduction law.

During a space mission, the satellite can only exchange heat with the external environment through radiative heat fluxes. On the other hand, the internal components can also exchange heat with each other through conduction.

As Daniele Calvi explains in his doctoral thesis [4], the S2T2 software solves equation (12) through the finite difference method (FDM), as this numerical method is compatible with the type of "primitive" geometries by which the satellite can be modelled.

Finite-Difference Method (FDM)

These codes define the solution to a finite-difference model that approximates the physical object. The nodes or sub-volumes are assumed to be isothermal and physical properties are assumed to be constant within a node. The nodes are linked by conduction and/or radiation. The governing partial differential equation is converted into a system of finite-difference equations by constructing an FDM mesh [7]. The basis for this step is the Taylor series approximation.

If we consider a one-dimensional Taylor series expansion, it has the following expression:

$$T(x_0 + \Delta x) = T(x_0) + \left. \frac{\partial T}{\partial x} \right|_{x=x_0} * \Delta x + \left. \frac{\partial^2 T}{\partial^2 x} \right|_{x=x_0} * \frac{\Delta x^2}{2!} + \dots \quad (13)$$

It follows that the first derivative and the second derivative can be approximated in the following way:

$$\left. \frac{\partial T}{\partial x} \right|_{x=x_0} = \frac{T(x_0 + \Delta x) - T(x_0)}{\Delta x} + O(\Delta x) \quad (14)$$

$$\left. \frac{\partial^2 T}{\partial^2 x} \right|_{x=x_0} = \frac{\frac{T(x_0 + \Delta x) - T(x_0)}{\Delta x} - \frac{T(x_0) - T(x_0 - \Delta x)}{\Delta x}}{\Delta x} + O(\Delta x^2) \quad (15)$$

where $O(\Delta x)$ and $O(\Delta x^2)$ are a means of expressing the order of the truncation error associated with the approximation.

At this point, it is appropriate to introduce the concept of a computational molecule, which considers each node in the mesh plus the nodes near it that influence it.

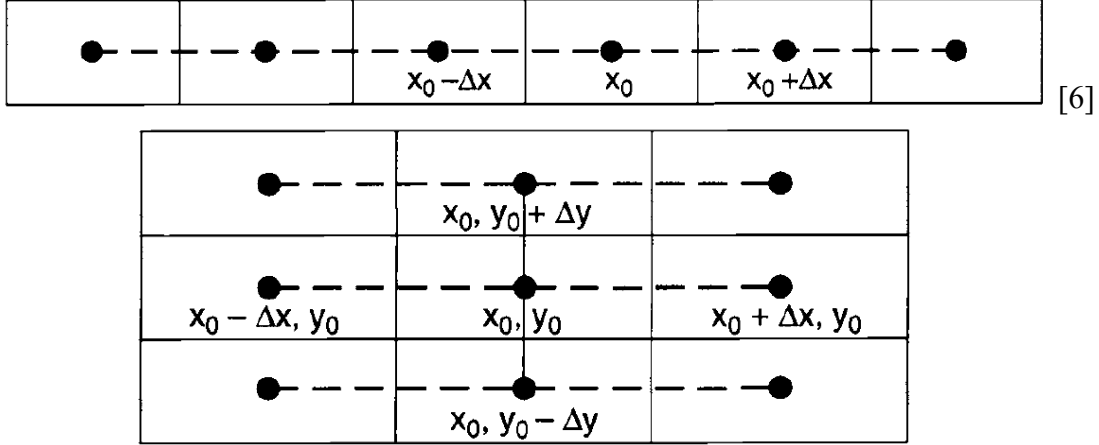


Figure 11: 1D computational molecule (up), 2D computational molecule (down)

Equation (12) can be written, for a heterogeneous and anisotropic solid in the following form:

$$\rho C_p \frac{\partial T}{\partial t} = \frac{\partial}{\partial x} \left[k_x(T) \frac{\partial T}{\partial x} \right] + \frac{\partial}{\partial y} \left[k_y(T) \frac{\partial T}{\partial y} \right] + \frac{\partial}{\partial z} \left[k_z(T) \frac{\partial T}{\partial z} \right] + \dot{Q}(T, t) \quad (16)$$

Considering the 1D computational molecule, the x-partial derivative $\frac{\partial}{\partial x} \left[k_x(T) \frac{\partial T}{\partial x} \right]$ can be written as:

$$\left[k_x(\delta^+) * \left(\frac{T_{n+1}(x + \Delta x, y, z) - T_n(x, y, z)}{\Delta x} \right) - k_x(\delta^-) * \left(\frac{T_n(x, y, z) - T_{n-1}(x - \Delta x, y, z)}{\Delta x} \right) \right] / \Delta x \quad (17)$$

Where n is the node number about which the Taylor series is applied.

The term k, since a heterogeneous and anisotropic solid has been considered, depends on the temperature and it is evaluated exploiting the mean temperature between nodes n and n±1:

$$\delta^\pm = \frac{T_n(x, y, z) - T_{n\pm 1}(x \pm \Delta x, y, z)}{2} \quad (18)$$

Multiplying equation (17) by the volume $V = \Delta x * A$, obtains

$$A * k_x(\delta^+) * \frac{(T_{n+1} - T_n)}{\Delta x} - A * k_x(\delta^-) * \frac{(T_n - T_{n-1})}{\Delta x} \quad (19)$$

The coefficient $A * k_x(\delta^\pm)/\Delta x$ is the conductance G defined in the previous paragraph. So, the equation (19) becomes

$$G_{n+1,n} * (T_{n+1} - T_n) - G_{n,n-1} * (T_n - T_{n-1}) \quad (20)$$

Where $G_{n+1,n} = A * k_x(\delta^+)/\Delta x$ and $G_{n,n-1} = A * k_x(\delta^-)/\Delta x$.

The radiation term, that in the equation (12) is contained in the term $\dot{Q}(T, t)$ can be made express as:

$$\sigma A \zeta_{n,n+1} (T_n^4 - T_{n+1}^4) \quad (21)$$

Where σ is the Stefan-Boltzmann constant, A is the radiating surface area and $\zeta_{n,n+1}$ represents the net radiation exchange between two surfaces, including all possible reflection. The term $A \zeta_{n,n+1}$ is the radiative conductance between two nodes.

The term $\frac{\partial T}{\partial t}$ of equation (16) can be approximated as follows:

$$T(t + \Delta t) = T(t) + \theta * \left. \frac{\partial T}{\partial t} \right|_{t+\Delta t} * \Delta t + (1 - \theta) * \left. \frac{\partial T}{\partial t} \right|_t * \Delta t \quad (22)$$

Where θ is a variable-weighted implicit factor. Multiplying equation (12) by the volume $\Delta x * A$ it can be observed that the coefficient for $\frac{\partial T}{\partial t}$ becomes

$$C_n = \rho * C_p * \Delta x * A \quad (23)$$

Where C_n is the node capacitance. Mixing equations (20), (21) and (22) the equation (16) becomes

$$\begin{aligned} & C_n \frac{T_n(t + \Delta t) - T_n(t)}{\Delta t} \\ &= \theta \left[\sum_{j=1}^N G_{jn} (T_j - T_n) + \sigma \sum_{j=1}^N A_n \zeta_{jn} (T_j^4 - T_n^4) + Q_n(T_n, t) \right]_{t+\Delta t} \\ &+ (1 - \theta) \left[\sum_{j=1}^N G_{jn} (T_j - T_n) + \sigma \sum_{j=1}^N A_n \zeta_{jn} (T_j^4 - T_n^4) + Q_n(T_n, t) \right]_t \end{aligned} \quad (24)$$

The last equation contains the parameter θ that assumes different values depending on the numerical method used to solve the equation in the time domain, as explained in Calvi's work Crank-Nicolson's method was chosen to be used so $\theta = 1/2$ [4].

From equation (24) we derive a system of n algebraic equations, where n is the number of nodes, which can be solved by either iterative techniques, matrix-inversion schemes or decomposition procedures. Usually, the system of equations is written as

$$T_{new} = [A] * T_{old} \tag{25}$$

Where $[A]$ is a nxn matrix and T is a nx1 column matrix. For thermal models of ten or more finite-difference nodes, $[A]$ is typically a sparse matrix because each node is normally connected to a small subset of the total number of nodes in the model [7].

Finally, to solve equation (25) it is necessary to introduce a boundary node that represents the space and it is set at temperature of 0°K.

View Factor Calculation

If two finite surfaces of area A_A and A_B are considered with normal vectors θ_A and θ_B measured with respect to the segment joining the two surfaces, as shown in Figure 12, then the view factor of surface A with respect to surface B is given by the following formula

$$F_{A-B} = \frac{1}{A_A} \int_{A_A} \int_{A_B} \frac{\cos\theta_A \cos\theta_B}{\pi L^2} dA_A dA_B \tag{26}$$

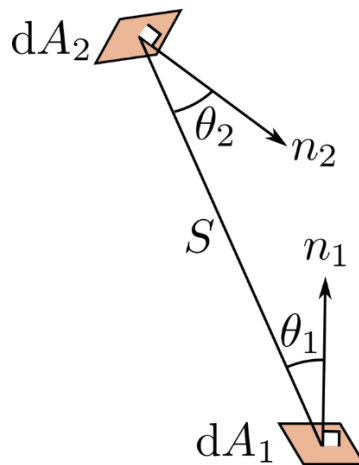


Figure 12: Radiation between two surfaces

The geometric view factor is a number between 0 and 1 that, given two surfaces, represents how much one surface is facing the other. In the case of calculating radiative exchange between two surfaces, the view factor represents the percentage of radiation emitted by one surface that reaches the other.

Monte Carlo Ray-Trace Method

The Monte Carlo Ray-Trace method (MCRT) is a numerical technique that allows the calculation of view factors using a statistical approach. Each radiative surface of each node emits a large number of light rays, the directions of which, however, are generated randomly. Each ray interacts with the surfaces of the system and can be either absorbed or reflected.

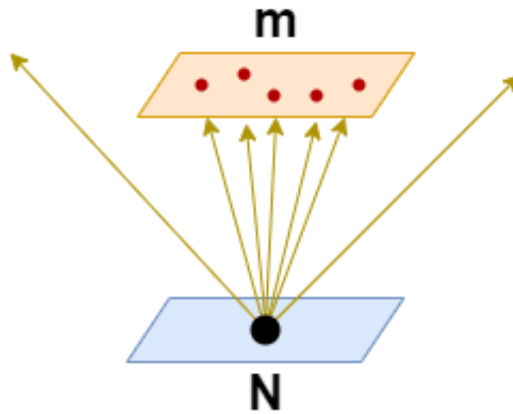


Figure 13: Ray tracing, N is the number of rays emitted, m is the number of rays absorbed

Consider two surfaces, between which to determine the view factor, Figure 13, emits a number of rays equal to N, surface 2 receives a number of rays equal to m, then the view factor of surface 1 to surface 2 is:

$$F_{1-2} = \frac{m}{N}$$

It is appropriate to introduce some mathematical concepts that are useful for understanding how the MCRT method works [9].

Consider two points in space P_0 and P_1 whose coordinates are, respectively (x_0, y_0, z_0) and (x_1, y_1, z_1) . The vector connecting P_0 with P_1 has the following expression:

$$\mathbf{V} = (x_1 - x_0)\mathbf{i} + (y_1 - y_0)\mathbf{j} + (z_1 - z_0)\mathbf{k}$$

(27)

And its magnitude is:

$$t \equiv \sqrt{|\mathbf{V} * \mathbf{V}|} = \sqrt{(x_1 - x_0)^2 + (y_1 - y_0)^2 + (z_1 - z_0)^2} \quad (28)$$

Where i, j and k are the unit vector direction along x, y and z respectively. The unit vector in direction of \mathbf{V} is:

$$\mathbf{v} \equiv \frac{\mathbf{V}}{t} = \Omega_x \mathbf{i} + \Omega_y \mathbf{j} + \Omega_z \mathbf{k} \quad (29)$$

Where $\Omega_x, \Omega_y,$ and Ω_z are the direction cosines, which are defined as:

$$\Omega_x \equiv \mathbf{v} \cdot \mathbf{i} = \cos \alpha, \quad \Omega_y \equiv \mathbf{v} \cdot \mathbf{j} = \cos \beta, \quad \Omega_z \equiv \mathbf{v} \cdot \mathbf{k} = \cos \gamma \quad (30)$$

Where α, β and γ are the angles between the unit vector \mathbf{v} and the axes x, y and z . equations (27) and (29) can be combined to define the equation for the line segment connecting P_0 to P_1

$$\frac{(x_1 - x_0)}{\Omega_x} = \frac{(y_1 - y_0)}{\Omega_y} = \frac{(z_1 - z_0)}{\Omega_z} = t \quad (31)$$

The equation to define a surface in cartesian coordinates is:

$$S(x, y, z) = 0 \quad (32)$$

In particular, if the surface is a plane, it is possible to derive its equation considering the plane normal vector n as shown in Figure 14.

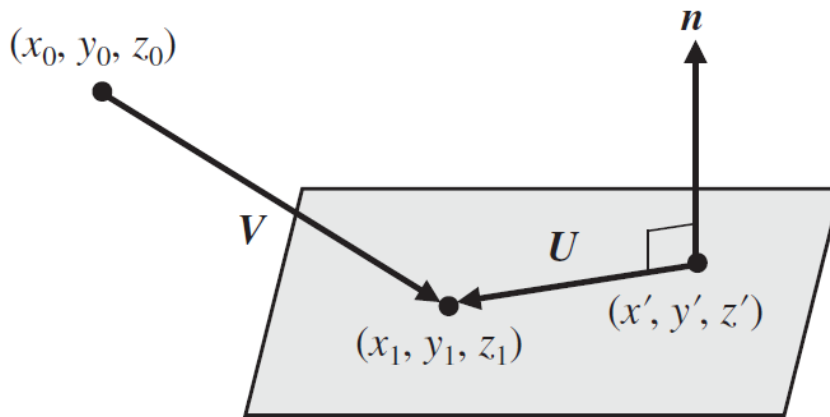


Figure 14: Definition of a plane surface [9]

Then the equation of the plane can be expressed:

$$\begin{aligned}
 S(x_1, y_1, z_1) &= \mathbf{n} * \mathbf{U} \\
 &= \mathbf{n} * [(x_1 - x')\mathbf{i} + (y_1 - y')\mathbf{j} + (z_1 - z')\mathbf{k}] \\
 &= n_x(x_1 - x') + n_y(y_1 - y') + n_z(z_1 - z') = 0
 \end{aligned}
 \tag{33}$$

To find the intersection between ray segment and the plane, equation (31) is introduced into equation (33):

$$n_x (x_0 + \Omega_x t - x') + n_y (y_0 + \Omega_y t - y') + n_z (z_0 + \Omega_z t - z') = 0
 \tag{34}$$

Solving for t:

$$t = \frac{n_x (x_0 - x') + n_y (y_0 - y') + n_z (z_0 - z')}{n_x \Omega_x + n_y \Omega_y + n_z \Omega_z}
 \tag{35}$$

Then it represents the distance between the point from which the ray is emitted and the point where it intersects the target surface. The line containing the ray, however, may intersect several surfaces in the enclosure, and each of them is characterized by a specific value of t. Therefore, to identify the first surface that the ray intersects, that is the first one illuminated by the radiation, the surface associated with the lowest value of t is selected for the evaluation of m.

The discussion, however, considers all surfaces as black bodies, i.e., each surface absorbs all the rays that reach it.

In reality, the energy incident on a surface is then broken down into three contributions, absorbed energy, reflected energy and transmitted energy as shown in Figure 15.

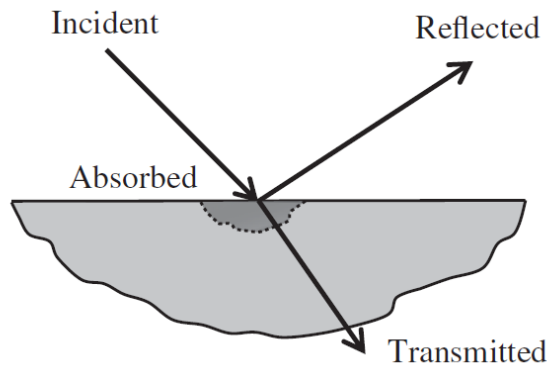


Figure 15: The disposition of the radiation incident on surface

The following expression can be derived:

$$Incident = Absorbed + Reflected + Transmitted \quad (36)$$

Dividing both members by the incident energy results in:

$$1 = \frac{Absorbed}{Incident} + \frac{Reflected}{Incident} + \frac{Transmitted}{Incident} \quad (37)$$

The three terms on the right-hand side of equation (37) are referred to, respectively, the absorptivity α , the reflectivity ρ and the transmissivity τ .

$$\alpha \text{ (or } \varepsilon) + \rho + \tau = 1 \quad (38)$$

For the Kirchoff law $\alpha_{IR} = \varepsilon_{IR}$, where α_{IR} and ε_{IR} are the absorbance and emissivity in the infrared wavelength respectively [9].

A surface is said opaque if its transmissivity for radiation incident from all directions and all wavelengths is zero.

$$\rho = 1 - \alpha = 1 - \varepsilon \text{ (Opaque surfaces)} \quad (39)$$

At this point, therefore, it is necessary to make the following distinction:

- F_{ij} represents the matrix of view factors considering all surfaces as black bodies.
- B_{ij} represents the matrix of view factors considering surfaces as grey bodies.

Before presenting the two methods implemented in the code for calculating the matrix B_{ij} , it is necessary to make the assumption of grey-diffuse surfaces [7]. This assumption implies:

- The temperature is uniform over the entire surface.
- The absorbance, or emittance, of a surface is independent of wavelength and direction
- All energy from a surface is reflected diffusely
- The incident and reflected energy flux is uniform over each surface

Gebhart's method

This method allows surfaces to be considered as grey bodies by taking as input the F_{ij} matrix, calculated with the MCRT method, and applying to it a correction based on the emissivity value of each surface [10] [11]. In this regard, the Gebhart factor is defined as follows [12]

$$B_{ij} = \frac{\text{Energy absorbed at surface } A_j \text{ originating as emission at } A_i}{\text{Total radiation emitted at } A_i} \quad (40)$$

Where A_i and A_j are the surface areas of, respectively, the i-th and the j-th nodes.

Thanks to the following general formula, for N_s surfaces in the enclosure

$$B_{ij} = \varepsilon_j F_{ij} + \sum_{k=1}^{N_s} ((1 - \varepsilon_k) F_{ik} B_{kj}) \quad (41)$$

For a generic surface i:

$$\sum_{j=1}^{N_s} B_{ij} = 1 \quad (42)$$

The equation (41) can be written in matrix form:

$$([\mathbf{I}] - [\mathbf{F}] \text{diag}(1 - \varepsilon))[\mathbf{B}] = [\mathbf{F}] \text{diag}(\varepsilon) \quad (43)$$

Monte Carlo Ray-Trace with reflection

In the MCRT method view, absorbability is interpreted as the probability that a beam of light incident on a surface is absorbed. This means that if a surface has an absorptivity of 0.5, a ray incident on it has a 50% possibility of being absorbed and a 50% possibility of being reflected [9].

The MCRT method interprets diffuse reflection as the portion of the incident energy that is redistributed in a hemispherical space above the point of intersection into a large but finite number of rays each of which has the same amount of energy, as shown in Figure 16: The diffuse reflection model

As far as the direction of the reflected ray is concerned, it is determined by the same statistical laws that govern the distribution of rays in the case of diffusive emission [9].

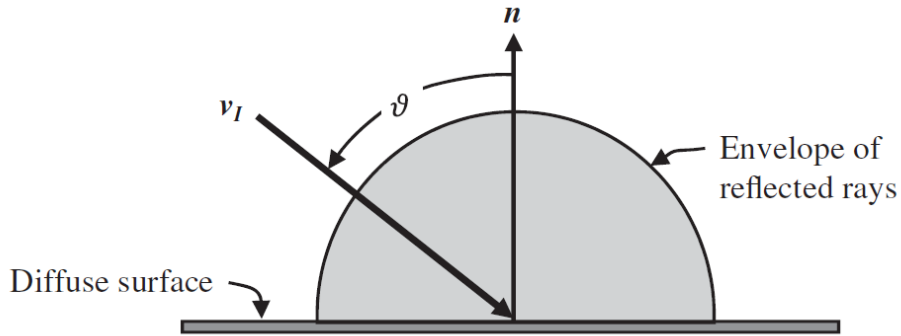


Figure 16: The diffuse reflection model [9]

The difference between the two methods is exposed through the fence problem. The geometry, shown in Figure 17, is formed by a fence at the middle point (red) of the long base rectangle which represents a single node. Node 1 is not radiatively coupled with node 2.

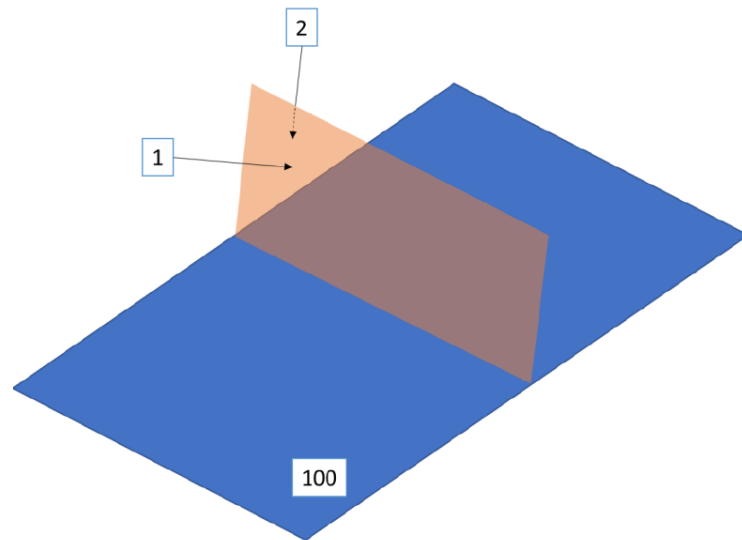


Figure 17: Fence problem [12]

Figure 18 shows how by the Gebhart method the ray incident onto the base rectangle is distributed and re-reflected from the entire area. With the MCRT method with reflection, the ray incident onto the base is reflected locally. Then, with Gebhart's method, the view factor between nodes 1 and 2 results greater than zero, also if this value should be null, as correctly obtained with the Monte Carlo method [12].

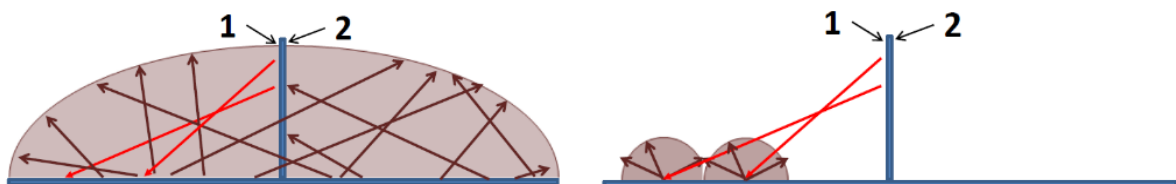


Figure 18: Gebhart method (left), MCRT with reflection (right) [12]

In conclusion, the MCRT method with reflection achieves more accurate results than Gebhart's method, but with a higher computational cost. In fact, by introducing reflection, the speed of calculation of view factors is highly dependent on surface finishes.

Environmental Analysis

The environment analysis consists of determining the value of all the heat fluxes that the satellite exchanges with the space environment surrounding it.

Figure 19 shows the various contributions to the heat fluxes entering and leaving the spacecraft, i.e., all the contributions of the \dot{Q} vector of the heat equation (12).

The individual contributions will be shown, in Figure 19, but it should be noted that these heat fluxes are only applied to the nodes defined as "external", i.e., all those nodes that interface with the space environment.

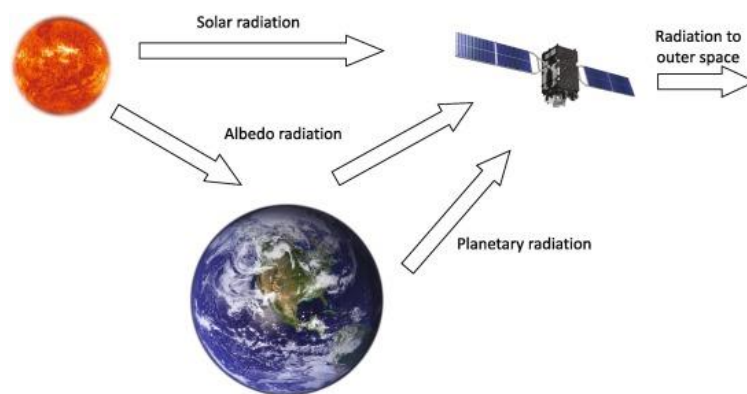


Figure 19: Environmental heat fluxes

Solar Direct

Solar radiation is the main source of heat for most low-earth orbit satellites. The intensity of solar radiation depends on the square of the distance from the sun, so since the orbit of the earth, and of all the other planets in the solar system, is elliptical, there will be a period of the year when solar radiation is maximum and a period when it is minimum. Specifically about the earth's orbit, we have the minimum value around the summer solstice, about 1322 W/m^2 , and the maximum value around the winter solstice, 1414 W/m^2 , as shown in the Figure 20.

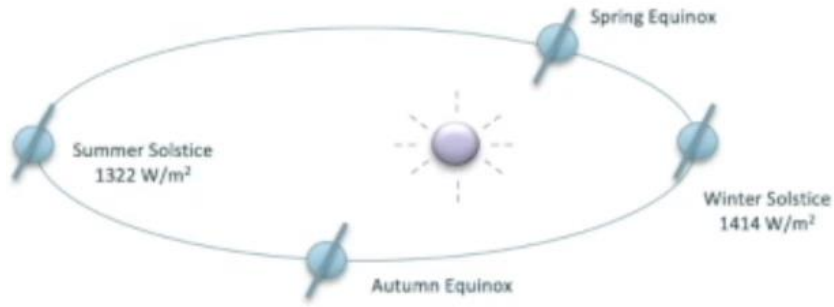


Figure 20: Aphelion and Perihelion heat flux

The intensity of solar radiation also varies according to wavelength, in particular, the energy distribution is 7% ultraviolet, 46% visible and 47% near-IR. Figure 21 represents both the solar spectrum and the spectrum emitted by a room-temperature body. It can be seen that the sun emits in the IR spectrum at a shorter wavelength. This behaviour allows, by appropriately selecting the satellite's external finish, to maximize the emission of S/C radiation while minimizing the absorption of solar radiation. The heat flow that each node receives is therefore:

$$\dot{Q}_{s,i} = C_s * \alpha_i * A_i * \cos\theta_i * F_{ecl} \quad (44)$$

Where C_s is the solar constant [W/m^2], A_i is the nodal radiative surface [m^2], α_i is the solar absorptivity, θ_i is the angle between the normal of the node surface with the sun vector [deg] and F_{ecl} is the eclipse factor, which is 1 when the node is illuminated and 0 when it is in shadow [7].

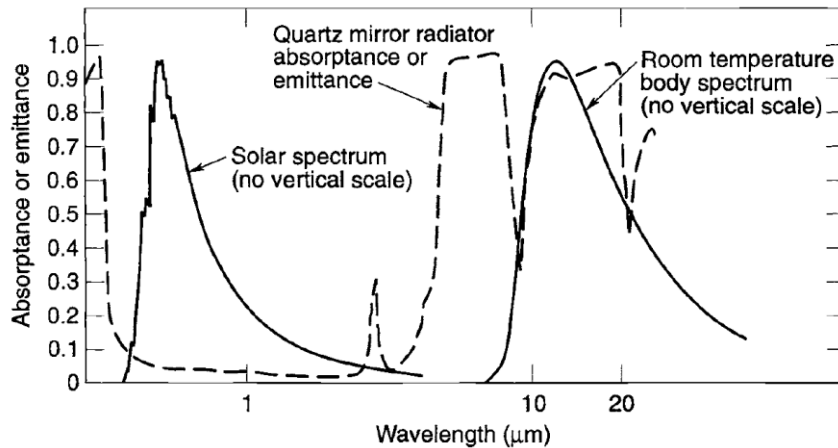


Figure 21: Solar and room-temperature-body spectral distribution [7]

Albedo

The albedo is defined as indirect solar radiation, i.e., that portion of solar radiation that once it hits a celestial body is then reflected back into space. Its value is given by the ratio of reflected solar radiation from the planet to incident solar radiation.

The albedo is characterized by great variability. It depends on what portion of the planet's surface reflects the solar radiation. Usually, reflected radiation is greater in continental areas than in oceanic regions, and increases with the presence of ice, snow or clouds, as shown in Figure 22.

The albedo value also depends on the incidence of solar radiation on the planet's surface. From Table 2: Typical Orbit-Average Earth IR and Albedo values it can be seen that the value increases with increasing latitude. The heat flow at each node is expressed as:

$$\dot{Q}_{A,i} = a * C_s * \alpha_i * A_i * \cos\beta_i * F_{i,p} \tag{45}$$

Where a is the albedo coefficient, which indicates the ratio between reflected and incident solar radiation, β is the angle between the line joining the centre of the planet with the surface of the node and the line joining the centre of the planet with the sun and $F_{i,p}$ is the view factor of the node surface with the planet [7].

Inclination [deg]	Angle of Sun out of orbit plane [deg]	Emitted radiation [W/m^2]		Albedo [%]	
		Min	Max	Min	Max
0-30	0	228	275	18	28
	90	228	275	45	55
30-60	0	218	257	23	30
	90	218	257	50	57
60-90	0	218	244	23	30
	90	218	244	30	57

Table 2: Typical Orbit-Average Earth IR and Albedo values [13]

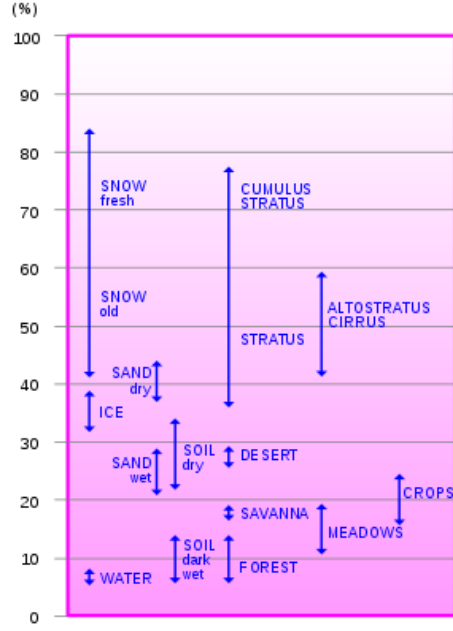


Figure 22: Albedo factor values

Planet IR and spacecraft IR emission

Any body with a temperature greater than 0°K emits radiation, so both the celestial body, around which the satellite orbits, and the satellite itself emit radiation. In particular, given the low temperatures involved, both emit in the infrared wavelength. The Earth has an average temperature of -18°C and therefore emits in a spectrum very close to that of the satellite; in Figure 21 they are represented by the same curve. It follows that unlike direct solar radiation; heat absorption cannot be minimized by the choice of special surface finishes.

As in the case of albedo, infrared radiation also depends on latitude but in this case, it increases towards lower latitudes as shown in Table 2.

$$\dot{Q}_{IR,i} = \sigma * \varepsilon_i * A_i * F_{i,P} * (T_P^4 - T_i^4)$$

(46)

Where T_p is the reference temperature of the planet [°C], T_i is the nodal temperature of the i-th node [°C], $F_{i,P}$ is the view factor of the node with the planet, ε_i is the IR emissivity of the node and σ is the Stefan-Boltzmann constant [$W/(m^2 * K^4)$],

The heat flux that each node emits to space has the following expression:

$$\dot{Q}_{sp,i} = \sigma * \varepsilon_i * A_i * (1 - F_{i,P}) * (T_{sp}^4 - T_i^4)$$

(47)

Where $(1 - F_{i,P})$ is the view factor between the node and the space and T_{sp} is the reference temperature of the space which is set to 3°K [7].

Chapter 3

Small Satellite Thermal Tool (S2T2)

In this subsection, the code developed during this thesis work is presented. The tool called Small Satellite Thermal Tool (S2T2) was developed in the MATLAB® environment.

The software is divided into the following modules:

1. Environment analysis: Its purpose is to analyze the space environment surrounding the satellite. In particular, this section, based on user inputs, retrieves the satellite's position vector along the entire orbit, identifies the direction of the sun vector, determines the period, and provides information regarding the spacecraft's attitude.
2. Geometrical Math Model module: This module is the focus of this thesis work. Its purpose is to create the satellite's geometry and calculate view factors. This information is then translated into data structures, which will be the input for subsequent modules.
3. Thermal Math Model module: Its purpose is to introduce additional connections between nodes in the model and incorporate dissipation for each node. This is done to create conduction and radiation matrices.
4. Analysis: This module takes input from the previous sections and calculates heat sources, which are then applied to each node of the model. This allows the software to determine the temperature of each node and present it to the user through both the "temperature trend" and the "heat map."
5. Design: This module aims to optimize the thermal design by modifying surface finishes and introducing thermal straps and heaters into the model. By the use of various optimization algorithms, it provides the user with alternative designs based on different objectives.

In this thesis, the main focus will be on the GMM module and the updates applied to this section. As for the Environment module and TMM module, they are extensively explained in the PhD thesis that inspired this work [4]. Regarding the design module, it is the subject of study in another thesis work [6].

Software Architecture

The first version of S2T2's code was effective but simple and did not handle input sequences other than nominal well, with many inconsistencies when backtracking and entering data already entered.

To allow the user to make real-time changes to the model, improving the usability of S2T2, the graph of possible user paths was greatly expanded and modified to allow for more robust backtracking of user input. Figure 23 shows the complete graph of all allowed usage paths, complete with non-nominal use cases (dashed lines).

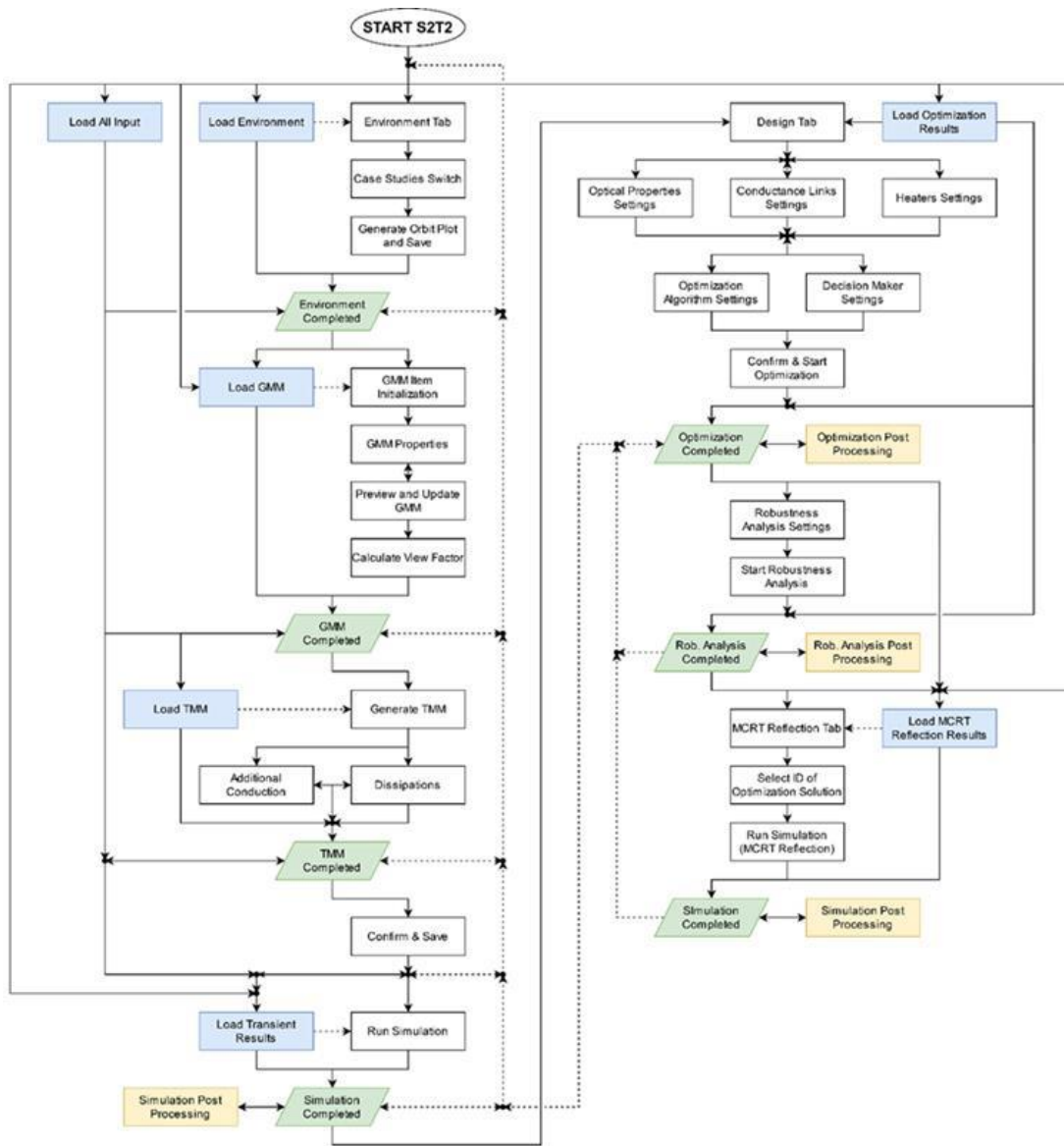


Figure 23: S2T2 architecture

In this new version of the code, the user can navigate more easily between the various paths, he can proceed to enter new data or review values already entered and make changes to them.

When the user takes a backtracking action, he must follow the dotted lines in the direction specified by the arrows.

The white rectangle in Figure 23 illustrates the buttons that the user must press to navigate between tabs and reach new milestones. It is important that the user follows the order shown by the arrows.

On the other hand, the yellow rectangles show the various graphic outputs that the code generates. Finally, the blue rectangles illustrate how and where it is possible to import data saved in '.mat' files from a previous work session. Typically, '.mat' files are automatically created in the main application folder when a milestone is reached.

During the development and testing of the software, the new user paths made it easier to navigate between input fields and manage data more freely, saving the time previously spent restarting the programme from the beginning after an incorrect user input. These improvements will also be useful for future non-expert users.

GMM Updates

In this subsection, updates made to the GMM module are presented. The high-level architecture of this module is depicted in Figure 24.

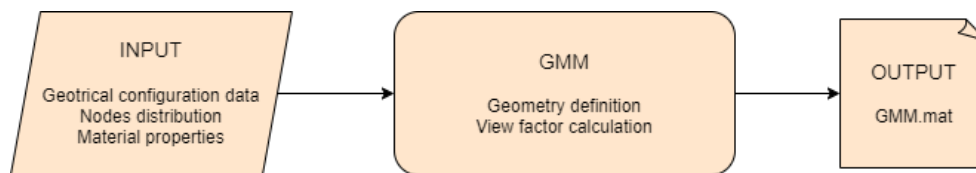


Figure 24: GMM high-level Architecture

This thesis work is inspired by the conclusions of Calvi's PhD thesis, specifically:

- Introduce new implementable geometries, particularly three-dimensional geometries.
- Allow users to choose the dimensions of the satellite structure.
- Introduce reflection within the Ray Tracing method for calculating view factors.
- Optimize the implemented algorithms in the code to speed up the execution.

Regarding the first point, the previous version of the code only allowed the modelling of internal satellite components using two-dimensional geometries, such as “boards”. Many subsystem components of the satellite can be represented with this type of geometry, such as electronic boards. However, this geometry becomes limiting when modelling a battery pack or a specific payload, for example.

Another limitation of the previous version of the code is that only objects internal to the satellite can be implemented. This restricts the modelling as it doesn't allow to represent deployable solar panels or antennas.

The software now includes solid geometries, such as parallelepipeds, which can represent objects where the third dimension is not negligible compared to the other two, as well as cylinders, which allow for the representation of reaction wheels or cameras, for example.

The code now also allows for the implementation of external appendages to the satellite, these new items are called "solar panels," and they can be used to represent objects external to the satellite.

Another modification to the code lies in the fact that, with the previous version, the user could only choose standardized geometries for the external structure of the satellite, based on the CubeSat Design Specification, with predefined dimensions [5]. With this new version, the user is free to choose the dimensions of the "box" that defines the structure.

Another limitation of the previous software version relates to the calculation of view factors. Firstly, the Ray Tracing algorithm was significantly slow, resulting in increased waiting times for the preparation of a single model. Additionally, a significant limitation compared to commercial codes is that the software previously used the Gebhart method to consider surface radiation reflection, which implies a certain error, as discussed in Chapter 2. Software like THERMAL DESKTOP, for example, utilizes the Ray Tracing algorithm but also includes reflection.

GMM Layout

The purpose of this module is to define the surfaces of each element, to discretize each of them into a list of nodes, to define the optical and mechanical properties, to determine the connectivity matrix of the nodes and finally to calculate the view factor between each node. The items that the tool is able to implement now are:

- Board 2D internal shell board
- Solar 2D external shell board
- Empty box used to create the satellite structure; it is composed by 6 2D surfaces
- Full box3D 3D internal Parallelepiped
- Cylinder 3D internal prism with a regular polygon at its base, If the number of the polygon sides increases then it can be considered as a cylinder.

For each item, the user must define the properties summarized in Table 3.

Geometrical properties	Dimensions [mm] Number of nodes Centre [mm] Orientation [deg] Colour Item name
Mechanical properties	Start temperature [°K] Conductivity [W/(m*K)] Density [kg/m ³] Specific Heat [J/(kg*K)] Thickness [mm] (only for 2D items) Optimal minimum temperature [°C] Optimal maximum temperature [°C]
Optical properties	Alpha Epsilon (internal and external for the structure)

Table 3: Item properties

Another of the most important updates in this new version of the software is the graphical user interface. In the previous version, there was a single tab where the user had to enter all the GMM inputs. With the addition of new items in the code, it was necessary to create a dedicated tab for each of them. In this way, the user can progressively follow the construction of the model.

A good way to take advantage of the updates in this version is to focus on generating one type of item at a time, entering the required data, and pressing the "Preview and Update GMM" button to view the model generated up to that point. Each time the user presses the button he can see that the image in the bottom right corner, which is present in each item tab, changes according to the changes made.

The user can also add or delete new rows within the data tables using the "Initialization" and "Delete Item" buttons. The first creates a number of rows in the tables equal to the number present in the "spinner box", it is not possible to delete rows using this method, but it is necessary to use the second button, which deletes the last row of each table present in the tab. The "visibility slider" allows the user to vary the transparency of the selected item, the box below it. While the "show ID" button allows you to display the numbering of the nodes in the graph.

Structure Tab

The structure is defined as an empty parallelepiped. The user can define its dimensions, the number of nodes for each dimension and the properties of each face. The orientation is predefined as $[0,0,0]$, ensuring that the faces of the structure are parallel to the principal axes.

It can be observed that there are two tables in the tab. The table on the left collects data related to the geometry of the object, while the one on the right gathers optical and mechanical properties.

In the case of the structure, it is worth noting that by default, the right table has 6 rows, each of which will collect the properties of each face. The numbering of the faces is specified in Table 4.

Face Number	Orientation
1	-Y
2	+X
3	+Y
4	-X
5	-Z
6	+Z

Table 4: Structure face numbering

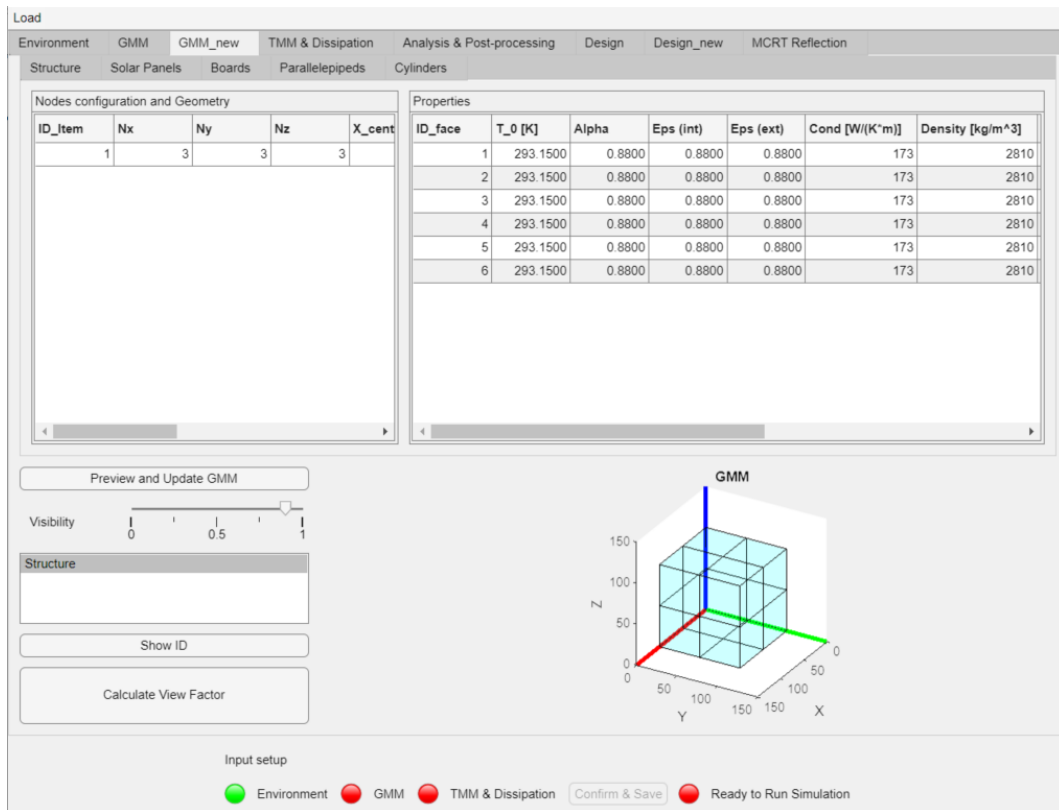


Figure 25: GMM structure module Layout

Solar panels and boards tab

Regarding the Solar Panels and Board tabs, they work similarly. Following the same logic used for the structure, the left table collects data regarding the geometric configuration of the item, while the right table gathers its properties

By default, every two-dimensional object is defined by the code as centred at the origin of the axes, with the normal vector pointing in the $-Z$ direction, as shown in t. With this information in mind, the user can manipulate the three variables, alpha, beta, and gamma, whose positive direction is shown in Figure 27. These variables respectively indicate the angle with concerning the X (red in the figure), Y (green in the figure), and Z (blue in the figure) axes by which the object will be rotated clockwise.

The difference between these items is that Solar Panels represent only external objects to the satellite, while boards represent only internal objects. In fact, solar panels, as in the case of the structure, receive heat flows from the environment.

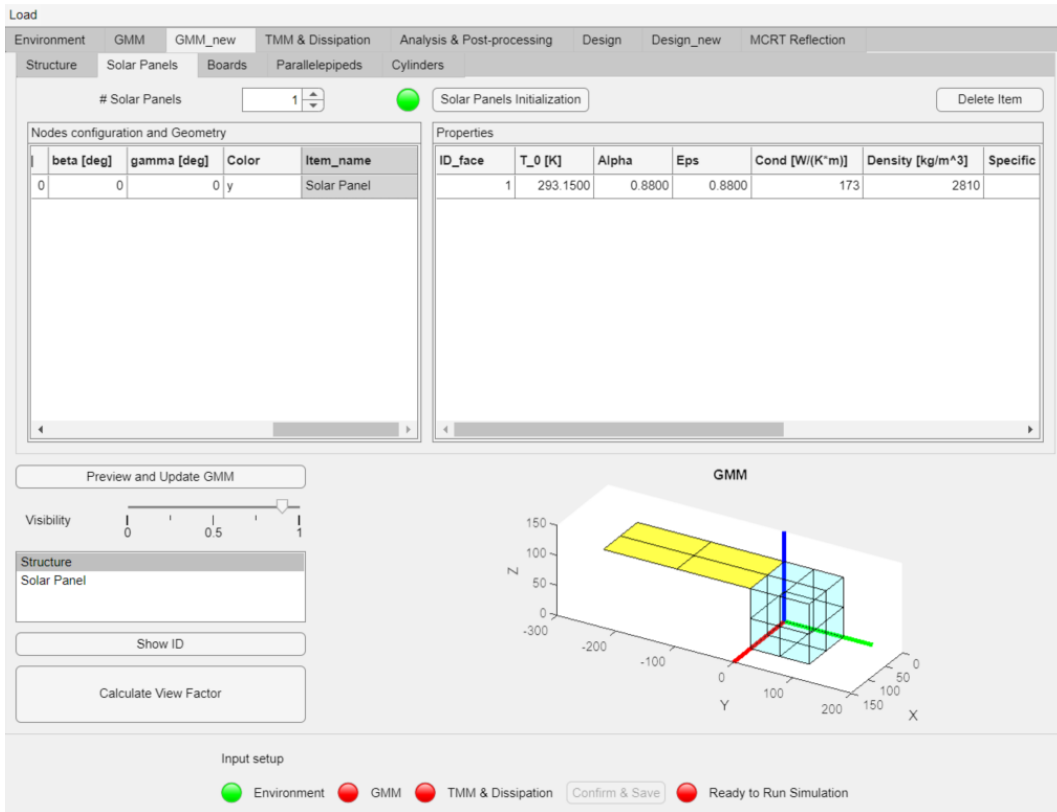


Figure 26: Solar Panels Tab Layout

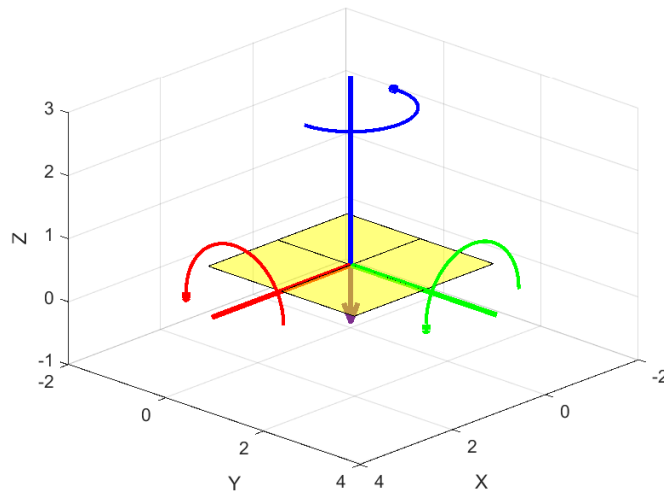


Figure 27: Default 2D Surface Definition

This item, introduced in the new version of the code, is only radiatively coupled with the structure, and for the calculation of the view factors between them, an external 'radiation group' was introduced into the code.

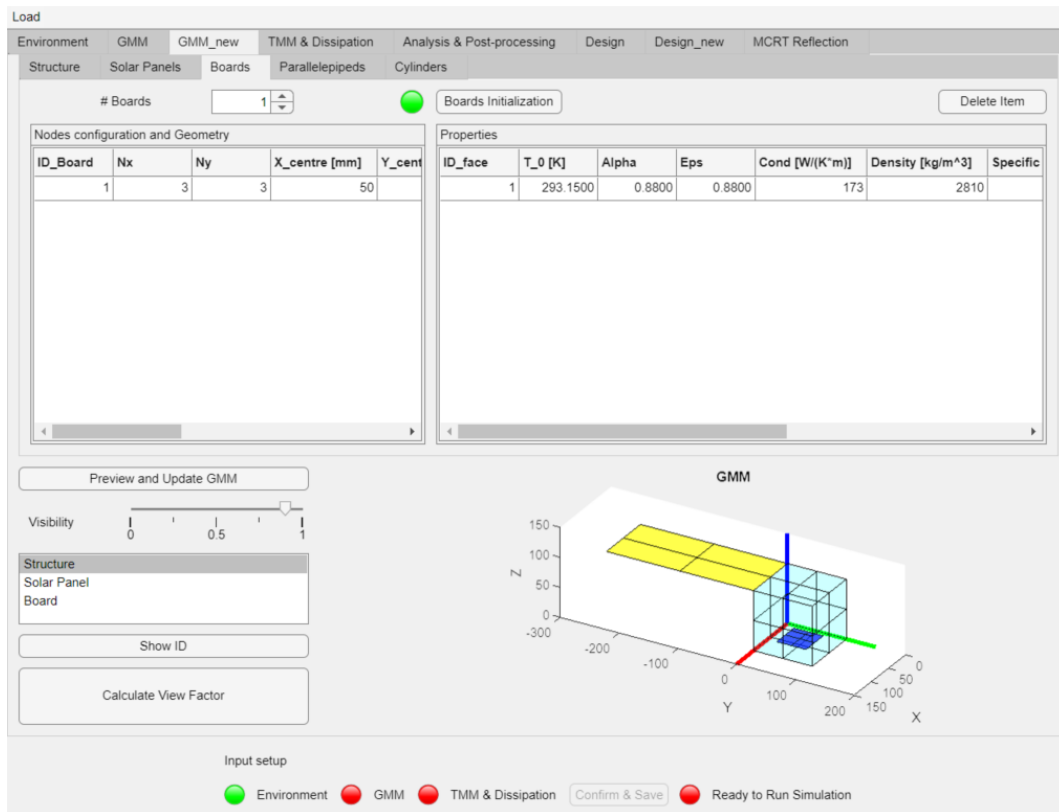


Figure 28: Boards Tab Layout

Parallelepipeds Tab

Parallelepipeds are the first three-dimensional objects introduced within the code. Similar to the previous tabs, the user can control the number of these objects to create using the spinner and the "Delete Item" button.

In this case, the tab presents three tables. The top-right table is used to define only the mechanical properties of the component, which will be unique to each parallelepiped. The third table, located in the bottom-right, allows the user to define the optical properties, specifically alpha and epsilon, for each of the parallelepiped's six faces.

Regarding the default definition of the parallelepiped, it is created with its geometric centre coinciding with the origin of the axes, and its faces are parallel to the principal axes with the normal vector of each face aligned with a fundamental axis. The faces follow the same numbering of the structure and alpha, beta and gamma are the same shown in Figure 27.

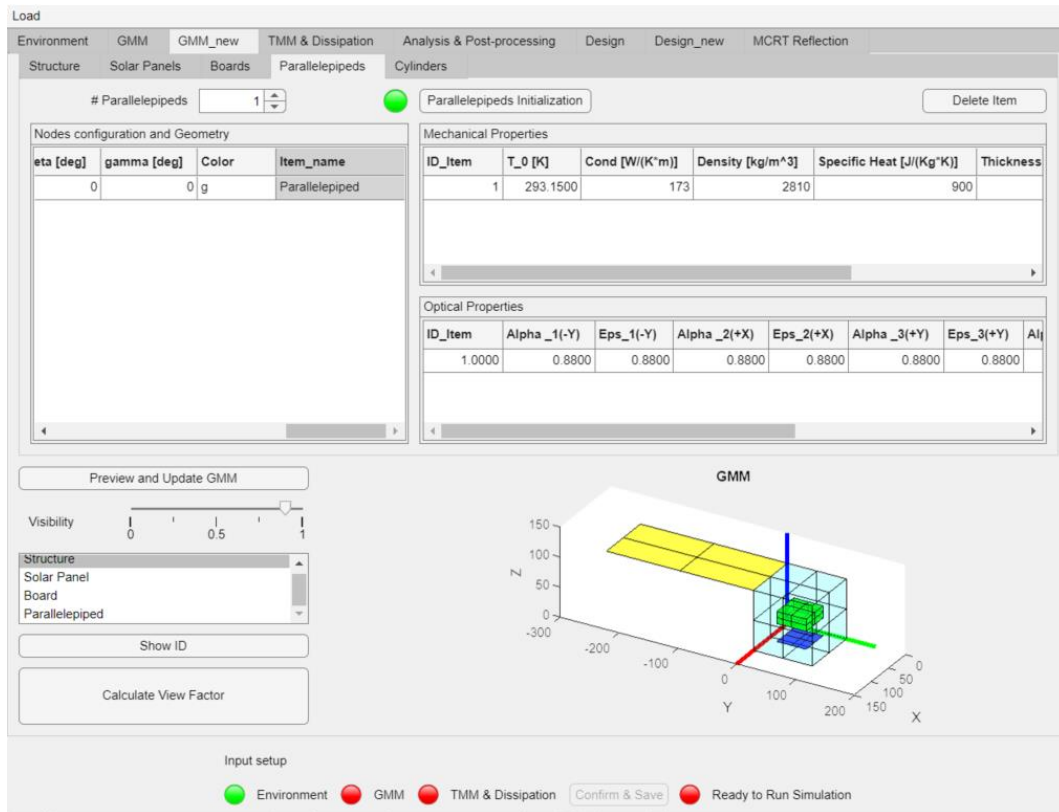


Figure 29: Parallelepipeds Tab Layout

Cylinder tab

Cylinders are actually implemented as prisms with a base composed of a regular polygon in the code. Users can use the left table to select the following options:

- Radius of the circle circumscribing the base polygon.
- Height of the prism.
- N_R the number of nodes along the radius (with a minimum of 2).
- N_t , the number of nodes along the circumference. Increasing this number will make the prism more closely resemble a cylinder.
- N_z the number of nodes along the length of the cylinder.

This way, users can define the dimensions and shape of the cylinder using these variables to achieve the desired precision.

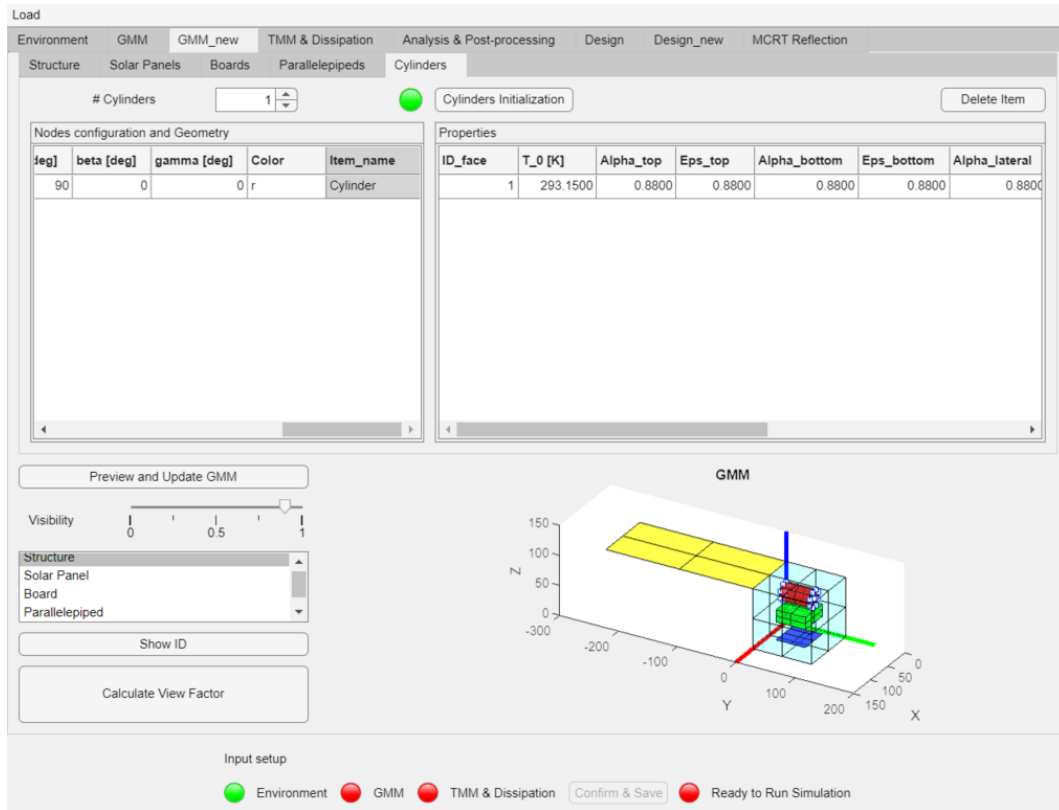


Figure 30: Cylinder Tab Layout

Regarding the other geometric data, the functioning is similar to the previous items. By default, the cylinder is created with its geometric center coinciding with the origin of the axes, and its faces pointing in the Z direction. Specifically, face number one will be the face pointing in the +Z direction, face number two will point in the -Z direction, and the remaining faces start from the position closest to the X axis and proceed with counterclockwise numbering with respect to Z. In Figure 31, the first lateral face is represented in green, while the last one is represented in cyan.

The white dots shown in the figure represent the surface nodes of the cylinder. They are highlighted to assist the user in defining additional conduction and nodal dissipation.

Figure 32 gives an idea of how the code calculates the areas of each cylinder node. It shows a slice of the top face of the cylinder defined by a single interval along the tangential direction, $\beta = 2\pi/N_r$. The nodes are indicated by red dots, R is the radius of the cylinder and $a = R/N_R$.

If $j = 1 \dots N_r$ is the counter along the radial coordinate then A_1 is equal to twice the area of the triangle defined by the segments a, b and c while the generic area $A_j = A_1 + 2 * (c * b) * j$. the area of the central node is equal to $A_1 * N_r$. using the same logic, we can calculate the areas of each node by calculating the length of each side of the trapezoids and multiplying it by dz, i.e., the height of the cylinder divided by the N_z .

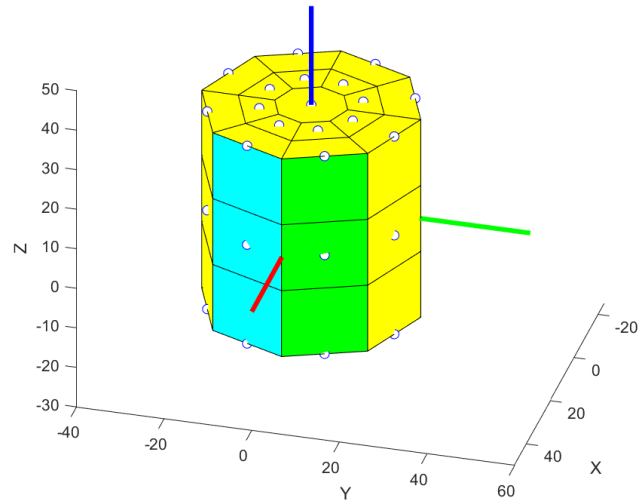


Figure 31: Cylinder Default Representation

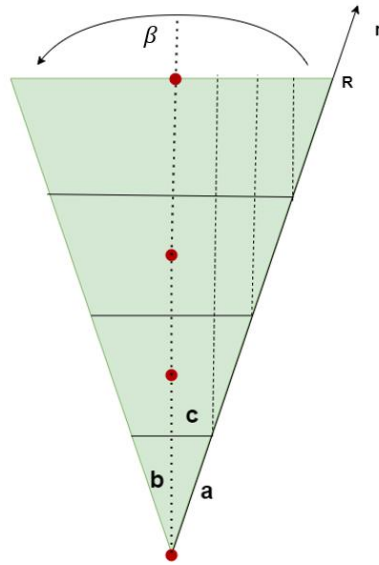


Figure 32: Cylinder areas calculation

Preview and Update GMM Button

When the user clicks on the "Preview and Update GMM" button, the code collects the data entered in the various tables and creates the GMM. The process of creating the GMM is expressed in the flowchart in Figure 33.

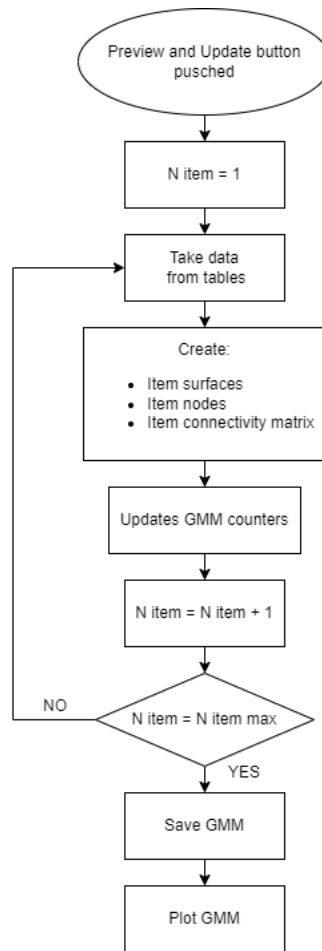


Figure 33: GMM flowchart

The logic of this algorithm is repeated for all objects in the satellite, both external and internal. Each new data created is added to the “sat” structure.

The task of GMM is to produce three types of data for each item:

- “Face”: a data structure which contains the info about the faces of every item, this structure, properly manipulated will be used to calculate the view factors.
- “Node”: a data structure which contains the info about the nodes
- “Connectivity”: a matrix that records the connections between nodes

One of the objectives of this thesis work is to make the code easily modular, facilitating the integration of any future work. Regarding the GUI, for example, adding a new geometry can be accomplished by adding a new tab to collect user input. Similarly, the function that generates the GMM, can be easily expanded by adding new specific functions for the new items. This modularity allows for flexibility and scalability in incorporating new features or components into the codebase. Figure 34 displays all the shapes implemented in the code.

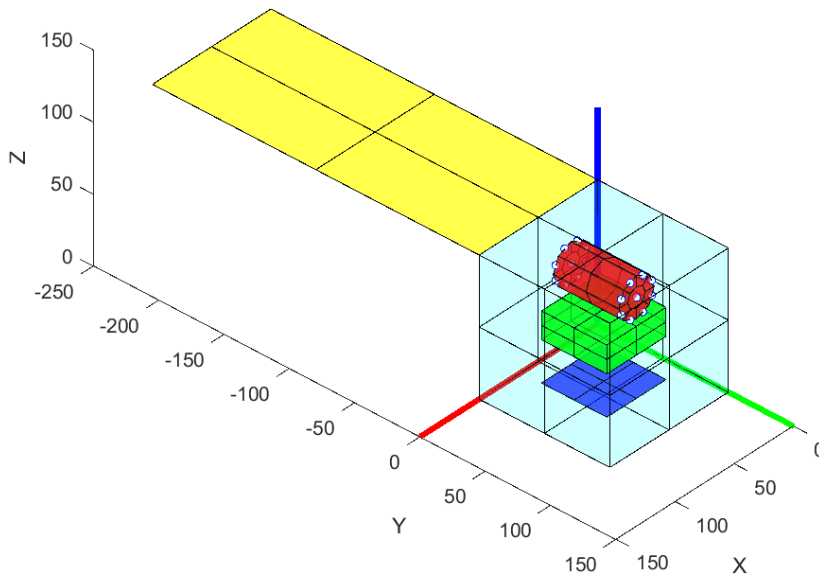


Figure 34: GMM All items

Once the geometries that make up the satellite have been defined, the GMM decomposes these primitive shapes into a series of nodes that will form the computational building blocks for temperature calculations.

Node creation

Each node has the following characteristics:

- The node type, which indicates how many surfaces converge on it. For example, in the case of a vertex node, three distinct surfaces converge on it. In the case of an edge node, there are two surfaces, while a central node has only one surface converging on it. In internal nodes, no surfaces converge.
- The coordinates of the node, which identify its location in space.
- The geometry of the node, which refers to the volume that characterizes that node.
- The radiative surfaces, which are the surfaces of the node that emit and transmit heat with radiation.
- The conductive surfaces, which are the surfaces through which the node exchanges conductive heat with the connected nodes.
- The item to which the node belongs.
- Whether the node is part of an external item, such as a structure or solar panels, or an internal item.

The logic by which each node is defined is expressed in Figure 35.

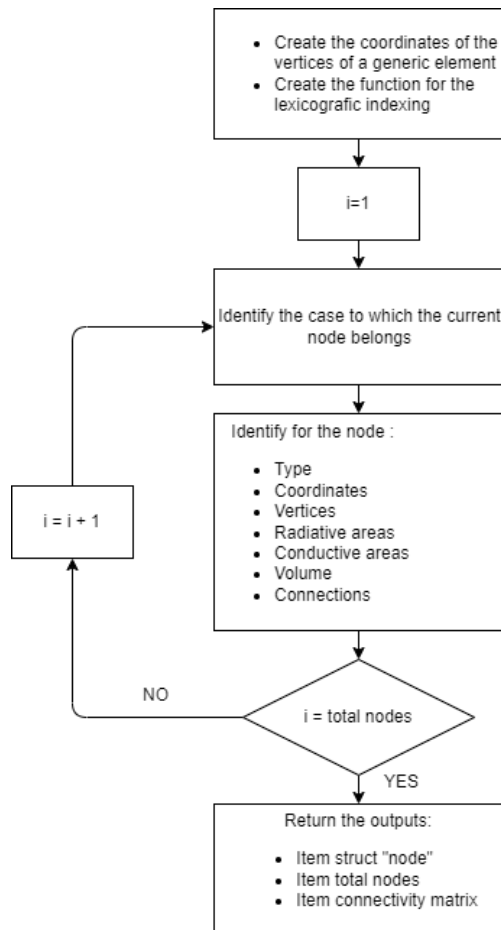


Figure 35: Node Creator Flowchart

For each item, once its dimensions and the number of nodes for each dimension are defined, all the properties of each node can be calculated beforehand. To explain this concept, in Figure 36, there is a 2D surface that will serve as the domain to be discretized into nodes. Let's assume that L_x represents the dimension of the surface along the x-axis, and L_y represents the dimension along the y-axis. L_x is divided into n_x nodes, while L_y is divided into n_y nodes. Therefore, the discretization steps in the two dimensions are $dx = L_x/n_x$ and $dy = L_y/n_y$.

The counter i , $1 < i < n_x$, iterate over the nodes in the x-direction, and j , $1 < j < n_y$, as iterates over the nodes in the y-direction. Thus, any node in the grid can be identified by the pair of values (i, j) , and their coordinates will be $x = i * dx$ and $y = j * dy$. This concept can also be extended to three-dimensional domains.

At this point, the concept of lexicographic ordering can be introduced. It allows to transition from an ordering based on two or more indices to an ordering based on a single index, as shown in Figure 37 using the following formula.

$$k(i, j) = i + (j - 1) * n_x$$

(48)

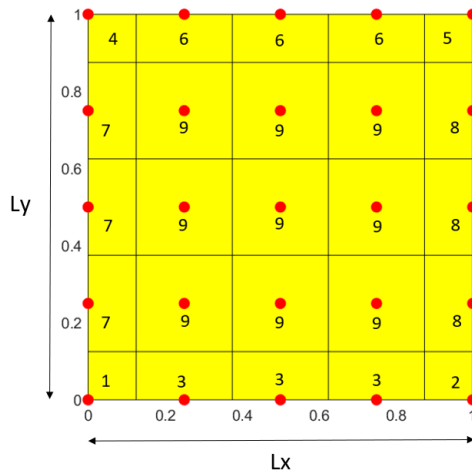


Figure 36: Example of Node Cases

This ordering is useful for determining which nodes are connected to the node under consideration. In the lexicographic ordering scheme, neighbouring nodes in the grid can be easily identified based on their indices. For example, the node (i, j) will have neighbouring nodes as follows:

- Left neighbor: $(i - 1, j)$
- Right neighbor: $(i + 1, j)$
- Upper neighbor: $(i, j + 1)$
- Lower neighbor: $(i, j - 1)$

Using this ordering, it becomes convenient to establish connections between nodes within the grid. The connectivity of a node can be determined by examining its neighbouring nodes based on the lexicographic ordering scheme.

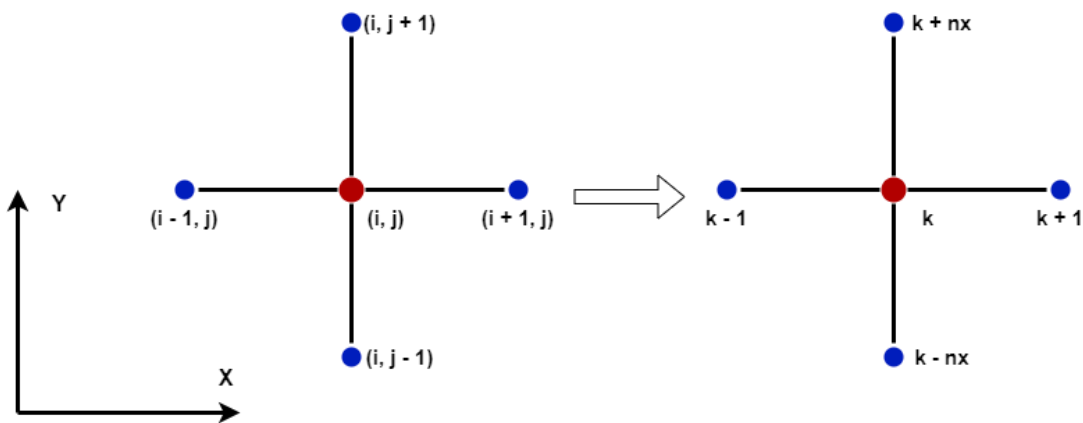


Figure 37: Lexicographic Sorting 2D

By observing Figure 36 the nodes can actually be grouped into 9 cases, indicated by the numbers assigned to them. Each of these cases has its own distinct characteristics. In

Table 5 three of these nine cases are listed.

<p>Case 1</p> $i = 1$ $j = 1$ $K = 1$	<ul style="list-style-type: none"> • <i>Node Coordinate</i> = $[xn, yn]$ • <i>Type: vertex</i> • $Af = dx/2 * dy/2$ • $Ac(+x) = dy/2 * th; Ac(-x) = none$ • $Ac(+y) = dx/2 * th; Ac(-y) = none$ • $V = Af * th$ • $Vert1 = [xn, yn]$ • $Vert2 = [xn + dx/2, yn]$ • $Vert3 = [xn + dx/2, yn + dy/2]$ • $Vert4 = [xn, yn + dy/2]$ • <i>Connection + X: K (i + 1, j)</i> • <i>Connection - X: none</i> • <i>Connection + Y: K (i, j + 1)</i> • <i>Connection - Y: none</i>
<p>Case 6</p> $1 < i < nx$ $j = ny$ $K = ny + (i - 1) * nx$	<ul style="list-style-type: none"> • <i>Node Coordinate</i> = $[xn, yn]$ • <i>Type: edge</i> • $Af = dx * dy/2$ • $Ac(+x) = dy/2 * th; Ac(-x) = dy/2 * th$ • $Ac(+y) = none; Ac(-y) = dx * th$ • $V = Af * th$ • $Vert1 = [xn - dx/2, yn]$ • $Vert2 = [xn - dx/2, yn - dy/2]$ • $Vert3 = [xn + dx/2, yn - dy/2]$ • $Vert4 = [xn + dx/2, yn]$ • <i>Connection + X: K (i + 1, j)</i> • <i>Connection - X: K (i - 1, j)</i> • <i>Connection + Y: none</i> • <i>Connection - Y: K (i, j - 1)</i>
<p>Case 9</p> $1 < i < nx$ $1 < j < ny$ $K = j + (i - 1) * nx$	<ul style="list-style-type: none"> • <i>Node Coordinate</i> = $[xn, yn]$ • <i>Type: central</i> • $Af = dx * dy$ • $Ac(+x) = dy * th; Ac(-x) = dy * th$ • $Ac(+y) = dx * th; Ac(-y) = dx * th$ • $V = Af * th$ • $Vert1 = [xn - dx/2, yn + dy/2]$ • $Vert2 = [xn - dx/2, yn - dy/2]$ • $Vert3 = [xn + dx/2, yn - dy/2]$ • $Vert4 = [xn + dx/2, yn + dy/2]$ • <i>Connection + X: K (i + 1, j)</i> • <i>Connection - X: K (i - 1, j)</i> • <i>Connection + Y: K (i, j + 1)</i> • <i>Connection - Y: K (i, j - 1)</i>

Table 5: Examples of three board cases

The underlying idea is that regardless of the length of the dimensions used to define a shape and the number of nodes into which it is divided, each node will always fall into a predetermined case that can be calculated beforehand. In fact, the algorithm used for defining the nodes leverages this

concept. It iterates over the indices of the different dimensions, identifies the case, and assigns the precalculated properties to the node.

This approach allows for the efficient and systematic assignment of properties to nodes, as the algorithm can determine the case of each node based on its position in the grid. By pre-calculating and organizing the properties according to the cases, the algorithm can rapidly assign the appropriate properties to each node during the node definition process.

Below the lexicographic ordering function K for the other object are reported.

Parallelepiped

$$X: 1 < j < nx \quad Y: 1 < l < ny \quad Z: 1 < h < nz$$

$$K(j, i, h) = j + (i - 1) * nx + (h - 1) * nx * nz$$

(49)

Empty Box

$$X: 1 < j < nx \quad Y: 1 < l < ny \quad Z: 1 < h < nz$$

$$K(j, i, h) = A(j, i, h) * (h = 1 || h = nz) + B(j, i, h) * (h \neq 1) +$$

$$C(j, i, h) * (h \neq 1 \& h \neq nz \& i \neq 1) +$$

$$D(j, i, h) * (NOT(h \neq 1 \& h \neq nz \& i \neq 1 \& i \neq ny \& j = nx)) +$$

$$E(j, i, h) * (h \neq 1 \& h \neq nz \& i \neq 1 \& i \neq ny \text{ AND } j = nx)$$

(50)

Where:

- $A(j, i, h) = (i - 1) * nx$
- $B(j, i, h) = nx * ny + ((nx - 1) * 2 + (ny - 1) * 2) * (h - 2)$
- $C(j, i, h) = 2 * (i - 2) + nx$
- $D(j, i, h) = j$
- $E(j, i, h) = 2$

Cylinder

$$\text{Angular: } 1 < i < Nt \quad \text{Radial: } 1 < j < Nr \quad Z: 1 < h < Nz$$

$$K(i, j, h) = (Nt * (Nr - 1) + 1) * (h - 1) + (j - 2) * Nt * (j > 1) + 1 + i * (j > 1)$$

(51)

For parallelepipeds, the lexicographic ordering is similar to the case of boards, with the addition of the third dimension. Each node is identified by a triplet of values (i, j, h) , representing its position

along the x, y, and z axes respectively. By incrementing or decrementing the values of i , j , or h , neighboring nodes can be determined.

As for boxes, the same grid structure as parallelepipeds is used, but certain conditions are applied to exclude internal nodes. These conditions ensure that only the surface nodes of the box are considered, while the internal nodes are excluded from the calculations. This allows for a more accurate representation of the box's shape within the grid.

Now, for cylinders, a special characteristic is observed when the radial component is equal to 1. In this case, all the nodes that would exist in the tangential direction coincide and form a central node. This means that instead of having separate triangular nodes in the tangential direction, there is a single central node.

By incorporating these specific considerations for parallelepipeds, boxes, and cylinders, the algorithm can appropriately define the nodes and their properties based on the unique characteristics of each shape.

In the case of cylinder, it is necessary to clarify the meaning of the names given, in

Table 6, to the various cases. The first adjective refers to the radial position, if $r = 1 \dots Nr$ is the counter along the radial coordinate, then central means $r = 1$, middle means $r = 2 \dots Nr - 1$ and external means $r = Nr$. The second adjective refers to the position along the height, if $z = 1 \dots Nz$ is the counter along the height of the cylinder, bottom means $z = 1$, intermediate means $z = 2 \dots Nz - 1$, and top means $z = Nz$. There are then three cases for each position "middle" and "external", because a further distinction is made based on the position along the tangential direction. if $\theta = 1 \dots Nt$ is the counter along the tangential coordinate then the first case is for $\theta = 1$, the second is for $\theta = 2 \dots Nt - 1$ and the third is for $\theta = Nt$.

Board (Solar Panels)	9 Cases	<ul style="list-style-type: none"> • 4 Vertex Nodes • 4 Edge Nodes • 1 Central Nodes
Empty Box	26 Cases	<ul style="list-style-type: none"> • 8 Vertex Nodes • 12 Edge Nodes • 6 Central Nodes
Parallelepipeds	27 Cases	<ul style="list-style-type: none"> • 8 Vertex Nodes • 12 Edge Nodes • 6 Central Nodes • 1 Internal Node
Cylinder	21Cases	<ul style="list-style-type: none"> • 1 Central Bottom • 3 Middle Bottom • 3 External Bottom • 1 Central Intermediate • 3 Middle Intermediate • 3 External Intermediate • 1 Central Top • 3 Middle Top • 3 External Top

Table 6: Item cases

Connectivity Matrix

In the context of connectivity matrices, the typical approach involves using an $N \times N$ matrix, where N represents the number of nodes. Each row of the matrix represents a node, and each column indicates whether there is a connection between nodes. Usually, a value of 1 is assigned where a connection exists, and 0 where there is no connection.

However, in the provided code, a different type of matrix has been implemented. Instead of containing only 1s and 0s, each column stores the index of the face through which a node is connected to the node identified by that column.

For example, $C(1, 2) = 3$, it means that node 1 is connected to node 2 through its conductive surface with index 3. Similarly, $C(2, 1) = 6$ implies that node 2 is connected to node 1 through its conductive surface with index 6. The numbering of conductive surfaces follows the order defined in the provided Table 7.

This modified approach allows for a more detailed representation of the connections between nodes by indicating the specific face or surface through which the connection is established.

Area Number	Orientation
1	+X (+Angular for cylinder)
2	+Y (+ Radial for cylinder)
3	+Z
4	-X (-Angular for cylinder)
5	-Y (- Radial for cylinder)
6	-Z

Table 7: Numbering of conductive areas

In addition, the conductive areas are stored within the node structure as a 6-component vector. Each component represents, according to the numbering in the provided table, the conductive area in a specific direction. This approach allows for the recording of both the information regarding the connection between two nodes and the conductive areas through which the nodes are connected in the TMM (Thermal Mathematical Model) matrix calculation. Figure 38 depicts an example of the global connectivity matrix for the entire satellite, while Figure 39 and Figure 40 illustrate how the nodes of various items connect to each other. The global connectivity matrix provides an overview of the connections between nodes throughout the satellite structure, while the second figure highlights the interconnections between the nodes of different items. These representations aid in understanding

the overall connectivity pattern and facilitate the analysis of thermal behaviour within the satellite system.

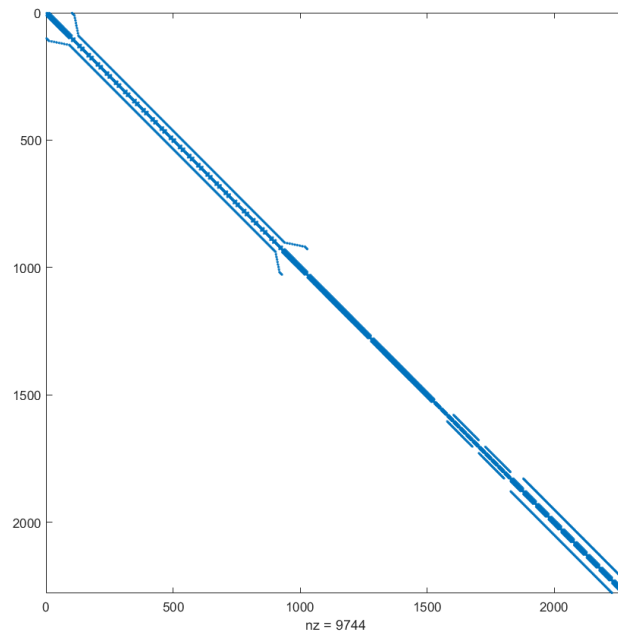


Figure 38: Example of connectivity matrix

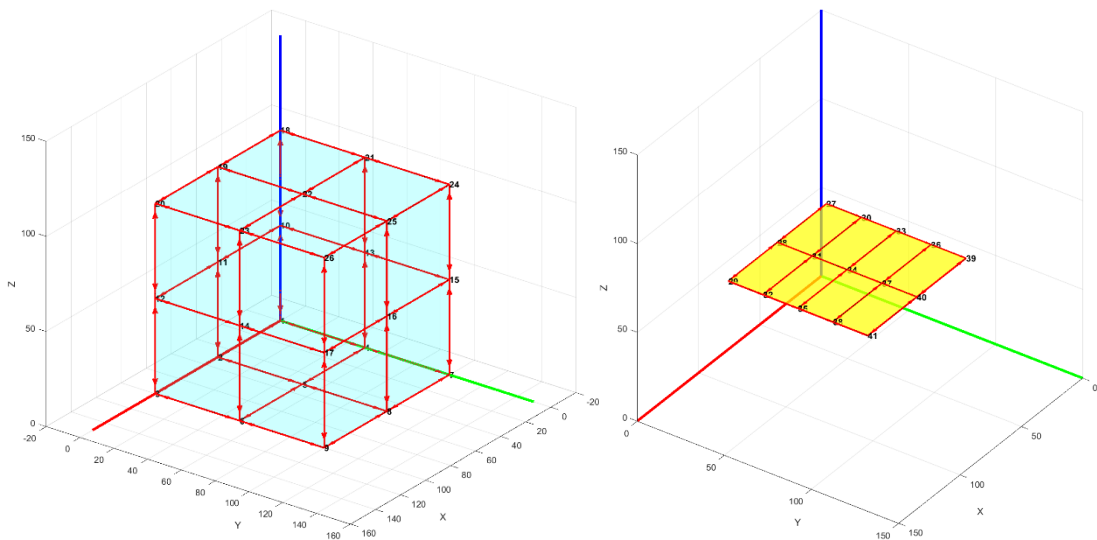


Figure 39: Examples of nodal connection box (left), board (right)

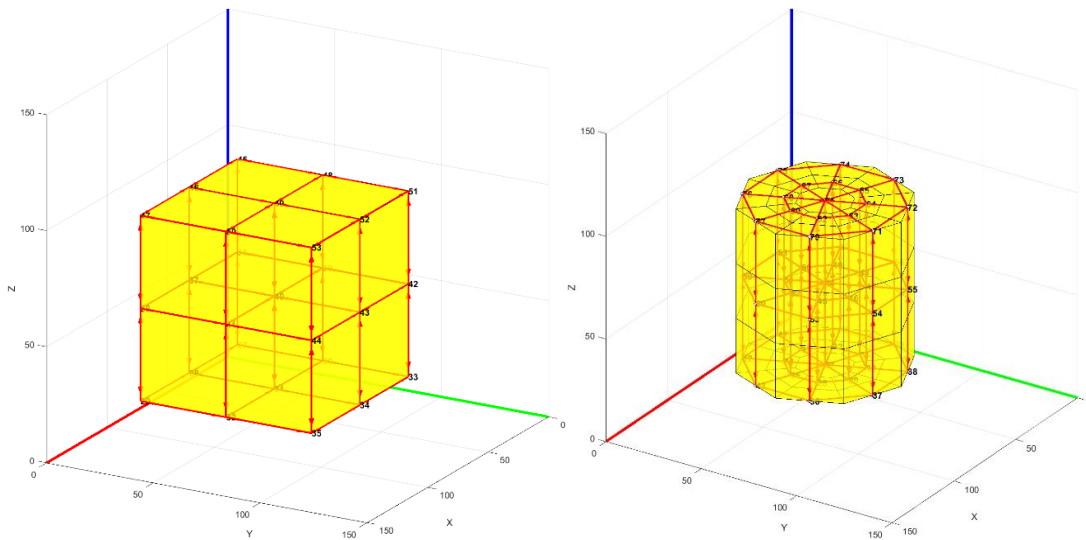


Figure 40: Examples of nodal connection parallelepiped (left), cylinder (right)

Calculate View Factor Button

Once the user has defined all the items the "View Factor" button can be pressed, which initiates the function for calculating view factors. Once the process is initiated, a loading bar appears within the button, indicating the percentage of surfaces that have been analyzed, as shown in Figure 41. The loading bar provides visual feedback on the progress of the view factor calculation. As the analysis proceeds and more surfaces are evaluated, the loading bar advances, indicating the completion percentage. This helps the user track the progress of the calculation and estimate the remaining time until completion. The view factor calculation is a crucial step in understanding the thermal interactions between surfaces and plays a significant role in determining heat transfer within the satellite system. The loading bar serves as a useful visual aid to keep the user informed about the ongoing calculation process.

The speed of the calculation process depends not only on the number of surfaces but also on the number of nodes into which the surfaces are divided. It is recommended to choose an appropriate number of nodes based on the desired level of detail for the analysis. However, it is important to strike a balance and avoid using an excessive number of nodes, as this can significantly increase the time required for calculating the view factors. Using a higher number of nodes allows for a more precise representation of the geometry and can capture finer details of the thermal interactions. However, it also increases the computational complexity and the time needed for the view factor calculations. Therefore, it is essential to find a balance between the desired level of detail and the computational efficiency of the analysis. It is advisable to perform some trial runs with different numbers of nodes to assess the impact on the calculation time. This way, the optimal number of nodes that provides an acceptable level of accuracy can be determined, without excessively prolonging the view factor calculation process.

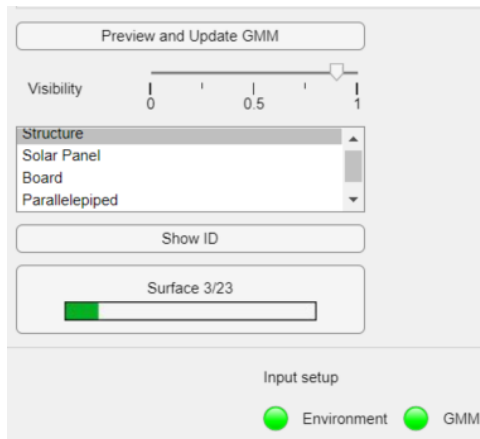


Figure 41: MCRT Wait bar

Figure 42 shows the evolution of the MCRT method from the first version, to those currently implemented in the code.

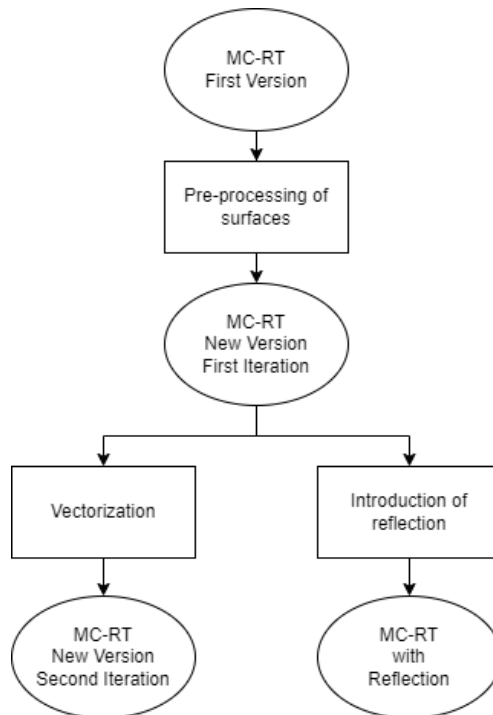


Figure 42: MCRT Evolution

MCRT New Version First Iteration

The first version of the code was essentially based on three nested loops. The outermost loop, the first one, defines the starting node from which the rays are emitted. The second loop, instead, defines the individual ray. Meanwhile, the innermost loop defines the destination node. Each node is treated as an independent surface, so for each satellite node, 5000 rays are emitted. For each of these rays, the intersection point is checked with each of the surfaces identified by each node of the spacecraft.

This coding approach leads to longer execution times due to the following reasons:

- Since the nodes of a surface are independent of each other, the algorithm may end up checking if the ray emitted from element i of surface $S1$, for example, intersects with element j of the same surface. The algorithm excludes j from the view factor calculation, but it still takes time to compute a solution that could have been discarded beforehand.
- Except for the structure, which emits rays inward, meaning the ray may intersect with another surface of the structure, for all other three-dimensional items, being convex solids, it is not possible for ray i emitted from surface $S1$ of a parallelepiped, for example, to intersect with surface $S2$ of the same parallelepiped.
- If a ray emitted from element i of surface $S1$ does not intersect with surface $S2$, in other words, it does not intersect the plane containing surface $S2$ within the polygon defined by its vertices, then that ray cannot intersect any of the nodes contained in $S2$.

To make the algorithm faster, the first technique used is to perform a pre-processing of all the surfaces by creating a dedicated data structure for calculating view factors with the MCRT method.

For each radiative surface of the spacecraft, the following characteristics are defined:

- A surface ID.
- The IDs of all the nodes that compose it.
- All the nodal surfaces that compose it.
- The vertices that define it.
- The centre.
- The normal vector.
- The area.
- The item to which it belongs.
- The IDs of the surfaces it can match with.

The pre-processing phase plays a crucial role in optimizing the view factor calculation process. It allows for the exclusion of surfaces that are not relevant to the view factor calculation for a particular node, reducing unnecessary computations and saving time. For instance, in the case of a cylinder, which typically has a larger number of faces compared to other items, avoiding the calculation of view factors between its constituent surfaces can lead to significant time savings. By excluding these unnecessary computations, the algorithm can focus on the relevant surfaces and expedite the calculation process. By implementing pre-processing techniques and excluding

irrelevant surface combinations, you can enhance the efficiency of the view factor calculation algorithm and reduce the overall computational time required for analyzing the thermal interactions within the satellite system.

Determine the location of the emission of the ray

In the previous version of the software the point of origin of the rays, emitted by a nodal surface, was the centre of the surface itself and was the same for each ray. However, this implied a certain error in the calculation of the view factors, which can be explained by the example shown in Figure 43. The two surfaces represent the faces of two nodes, the green surface is the starting surface and the blue surface is the target surface. They are placed perpendicular to each other and the target surface is positioned above the center of the green one. If the rays are all emitted from the centre the starting surface (on the left), the black point, then none of them will ever meet the target surface, but at most will be parallel to it. In the second case (on the right), on the other hand, they are emitted from random points within the starting surface. The figure shows how in this second case the view factor between the green and blue surfaces is non-zero.

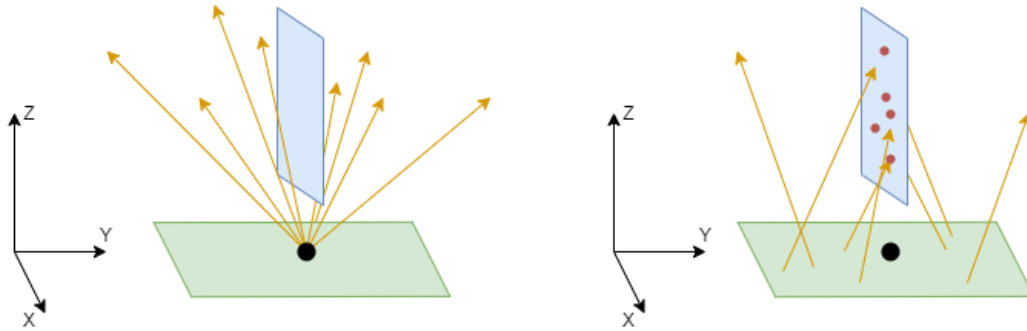


Figure 43: Single emission point (left), random emission points (right)

A simple way to select a random point of origin on the surface is to draw a circle placed in the center of the surface with a radius large enough to include the entire surface, and then select the starting point within the circle by randomly varying the radial distance and angle, as shown in Figure 44 [14].

The random point coordinates are calculated with the following expressions

$$x_i = x_0 + r_i * \cos(\phi_i) \qquad y_i = y_0 + r_i * \sin(\phi_i) \qquad (52)$$

Two random numbers, ξ_1 and ξ_2 , are generated using MATLAB's 'rand' function

$$\phi_i = 2\pi\xi_1 \qquad r_i = R * \sqrt{\xi_2}$$

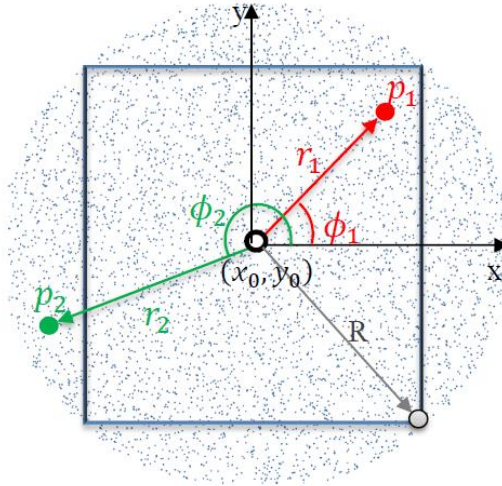


Figure 44: Random points within surface

(53)

ξ_2 is placed under the square rtor to have a uniform distribution of points along the radius. To avoid selecting a point outside the surface, a number of points are first generated and then through MATLAB's 'inpolygon' function all those outside the surface are excluded.

Determine the direction of the ray

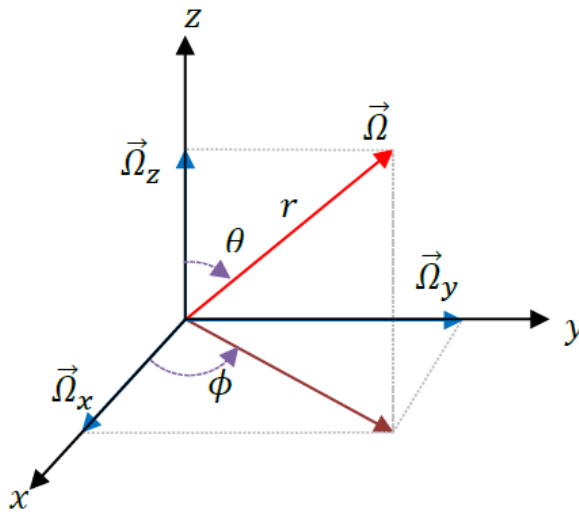


Figure 45: Ray direction definition [14]

$$\begin{cases} \Omega_x = r * \sin\theta * \cos\phi \\ \Omega_y = r * \sin\theta * \sin\phi \\ \Omega_z = r * \cos\theta \end{cases}$$

(54)

Where $\Omega = [\Omega_x, \Omega_y, \Omega_z]$ is the ray direction, $r = 1$, θ is the polar angle which change from 0 to $\pi/2$ for a hemispherical emission and change from 0 to π for spherical emission, φ is the azimuthal angle which change from 0 to 2π .

Two random numbers, ξ_1 and ξ_2 , are generated with MATLAB's 'rand' function, and they are used to define the polar angle and azimuthal angle.

$$\theta = \text{asin}(\sqrt{\xi_1}) \text{ (Hemispherical emission)} \quad \theta = \text{acos}(1 - 2 * \xi_1) \text{ (Spherical emission)}$$

$$\varphi = 2 * \pi * \xi_2$$

(55)

The equation (55) is used to calculate θ because multiplying ξ_1 by $\pi/2$, or π , would not result in a uniform distribution, but there would be a concentration of points in the directions $\theta = 0$ and $\theta = \pi$. Figure 46 and Figure 47 show the intersection of the rays emitted by the centre of the element in yellow with a sphere of unit radius.

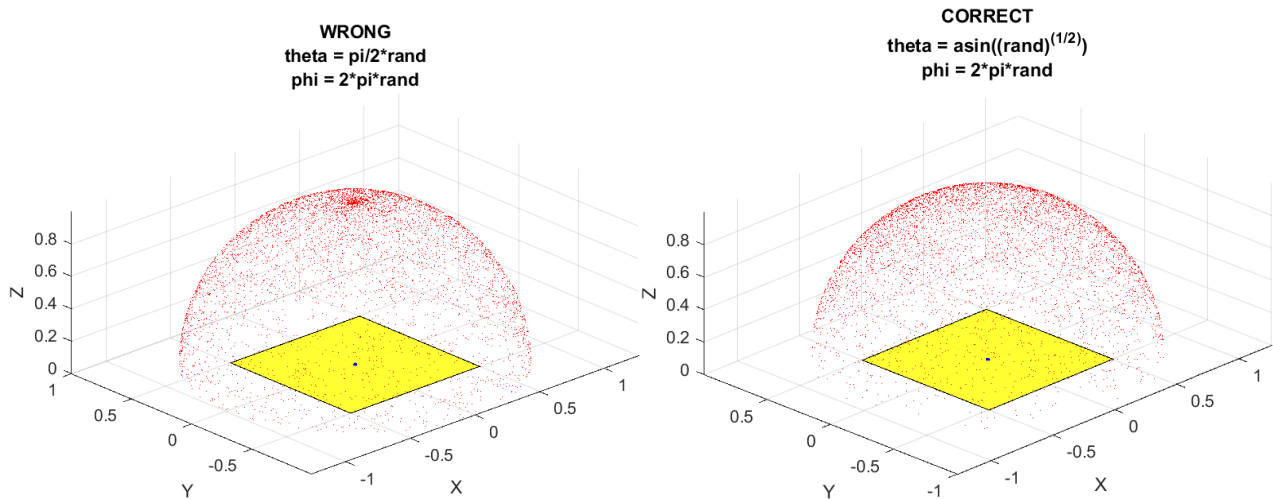


Figure 46: Hemispherical distribution, non-uniform (left), uniform (right)

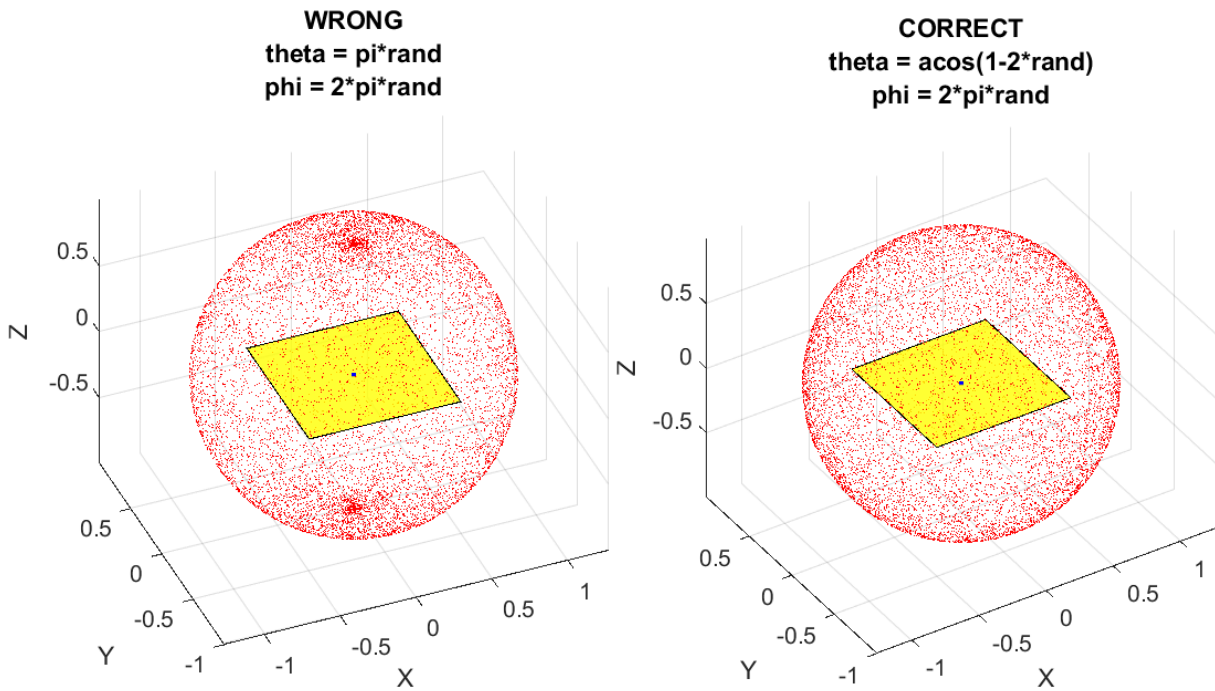


Figure 47: Spherical distribution, non-uniform (left), uniform (right)

Point inside polygon

Another issue related to this method is determining whether a point is contained within a surface that is arbitrarily oriented in space. To address this, a custom function has been implemented. It takes as input the area of the surface, the coordinates of the vertices that enclose the surface, and the coordinates of the intersection point between the ray and the plane containing the surface. The function then calculates the areas of the triangles formed by connecting two vertices of the surface and the test point, sums them up, and if the sum is greater than the input area within a certain tolerance, the point is considered external to the surface; otherwise, it is considered internal.

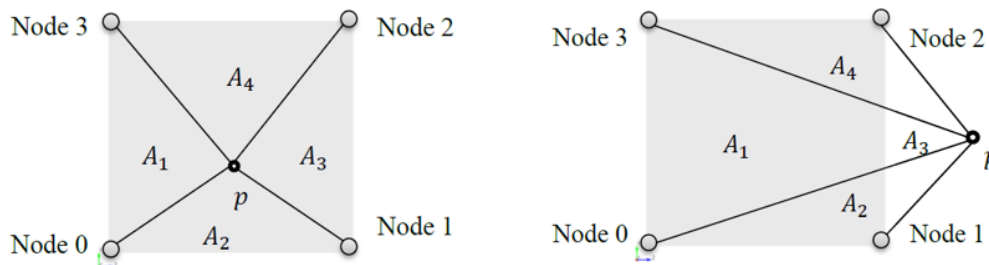


Figure 48: Left the point is inside; Right the point is outside [14]

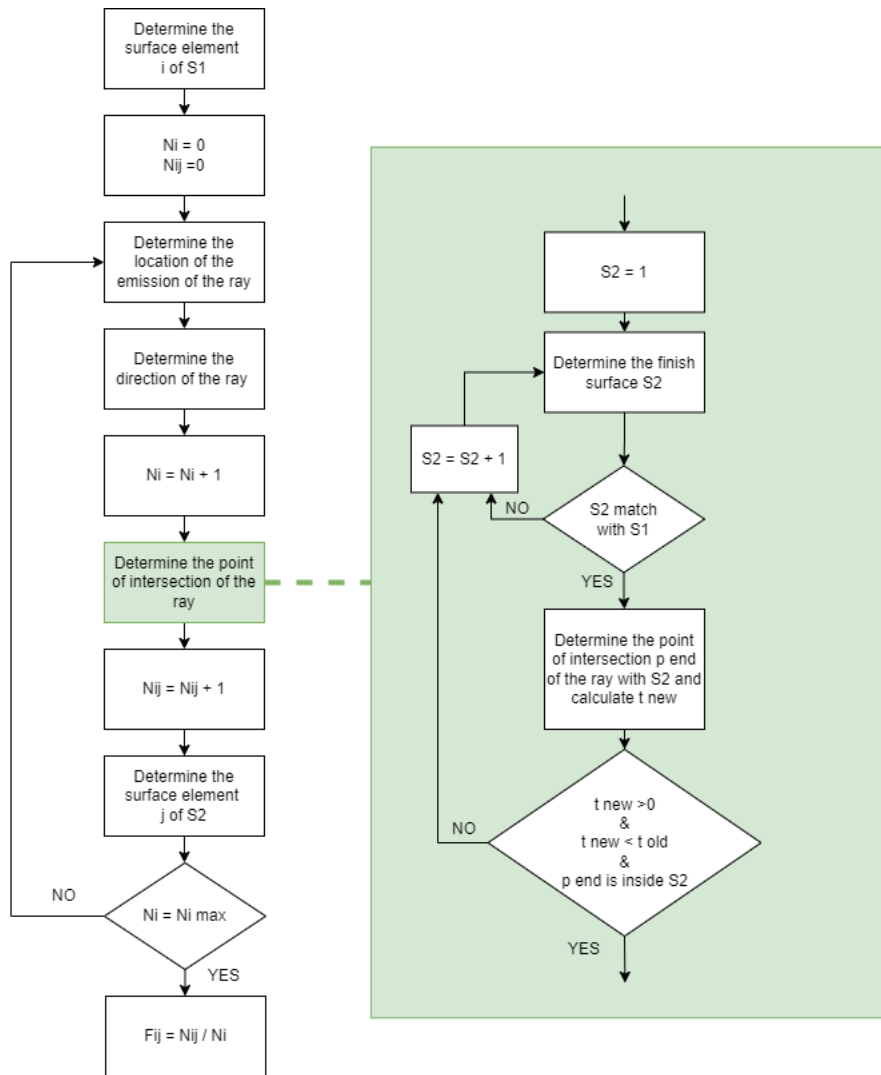


Figure 49: MCRT New Version First Iteration Flowchart

MCRT New Version Second Iteration

Vectorization in MATLAB refers to the process of executing operations on entire arrays or matrices instead of individual elements using loops. It takes advantage of the optimized operations on arrays and MATLAB's parallel computing capabilities to improve code execution speed [15]. By avoiding explicit loops and using operations on arrays, vectorization reduces the overhead associated with loop initialization, condition checks, and index updates. This leads to faster execution times as calculations are performed on larger data sets in a single operation. It reduces the chances of introducing errors and facilitates code maintenance and debugging.

Vectorization is particularly effective when dealing with large data sets or when performing repetitive calculations as in the case of the MCRT method. In general, vectorization in MATLAB helps increase execution speed by eliminating the need for explicit loops, optimizing memory access, using hardware acceleration, and taking advantage of MATLAB's optimized array operations and parallel computing capabilities.

First, the loop used to iterate each surface was replaced by operations on arrays. This allowed simultaneous calculations to be performed on all surfaces using multidimensional arrays, reducing the need for individual iterations. Second, the intersection calculations between rays and surfaces were vectorized. Instead of running a cycle for each ray and surface, matrix and elementary operations were used to compute the intersections of all rays and surfaces at once. This eliminated the need for nested cycles and significantly improved efficiency. Similarly, the view factor calculations between emitting and receiving elements were vectorized. Instead of nested loops, array operations were used to calculate the view factors of all elements simultaneously.

An additional step was to optimize the function that determines whether a point lies within a polygon. Previously, the function analyzed one point at a time, slowing down execution. To overcome this problem, a native MATLAB function was used that takes a series of points as input and simultaneously determines whether they are within the assigned polygon.

Overall, by applying vectorization, the algorithm was able to achieve faster execution times by performing computations on whole arrays and matrices, reducing dependence on explicit loops and taking advantage of MATLAB's optimized array operations and parallel computing capabilities.

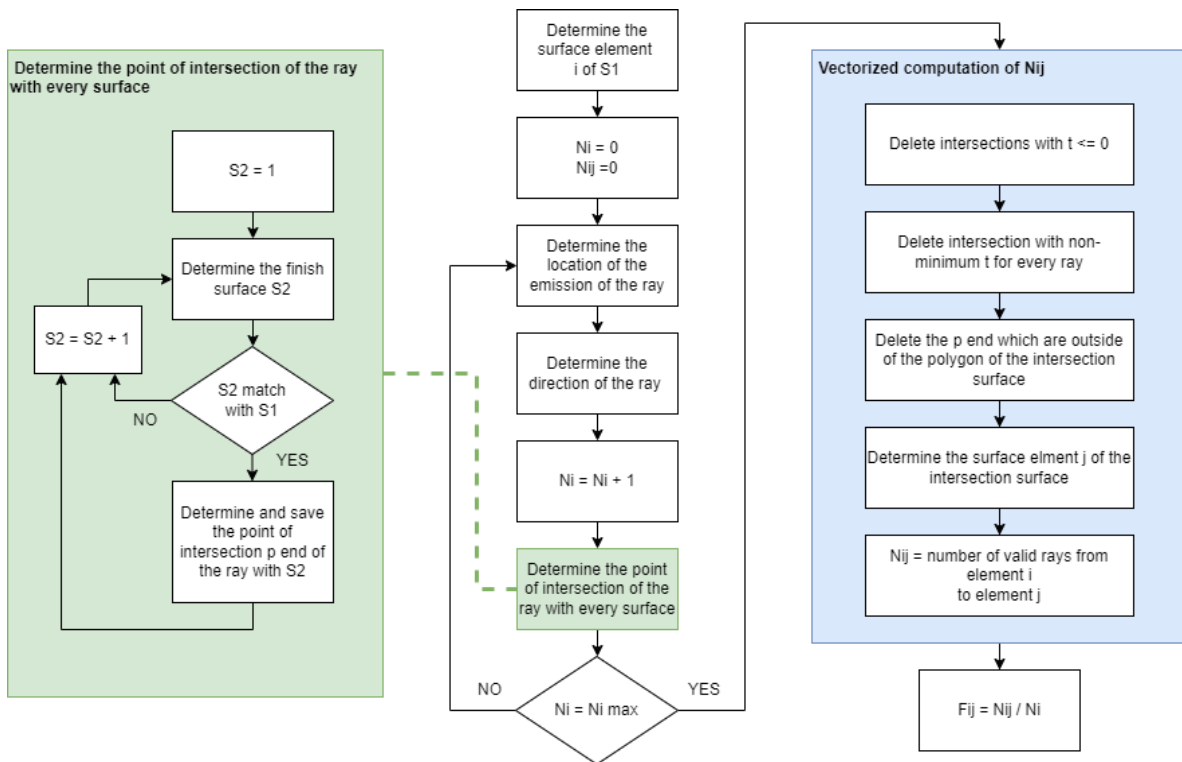


Figure 50: MCRT New Version Second Iteration Flowchart

MCRT Reflection Tab

In the MCRT method, the inclusion of reflection was introduced in the first iteration of the new version. However, it was not optimized with the vectorization technique; in fact, the execution time remains relatively long, considering also the increase in computation time that the introduction of reflection into the algorithm implies. Due to this reason, it was not incorporated as the default method for calculating view factors in the GMM Tab. Instead, a separate tab was dedicated to it at the end of the GUI. Through this tab, users have the option to choose one of the solutions proposed by the optimization process and use it to perform a complete analysis again. However, this time, the MCRT method with reflection is used for calculating the view factors. Similar to the Analysis and Post-processing Tab, this tab also provides the ability to visualize the results in the form of temperature trends and heat maps.

With a separate tab for the MCRT method with reflection, users can explore and compare different analysis approaches, including optimized solutions. This allows users to flexibly choose the method best suited to their specific needs, taking into account factors such as accuracy and computational efficiency.

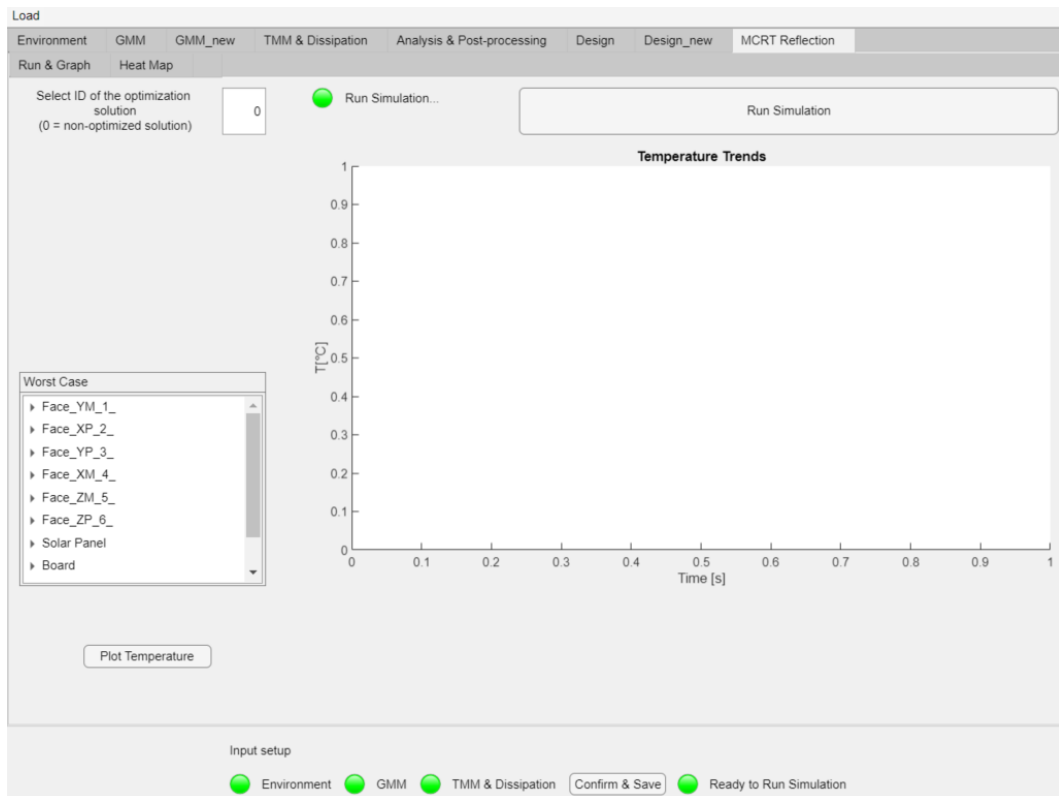


Figure 51: MCRT with Reflection Tab Layout

Introduction of Reflection

The idea behind applying reflection in the MCRT method is to interpret the absorptivity of a surface as the probability that an incident ray on it is actually absorbed. This introduces a statistical interpretation of the optical properties of a surface as explained in Chapter 2

The algorithm has been modified as follows:

1. Identify the receiving surface for the ray emitted from node i and the point of intersection of the ray with that surface.
2. Generate a random number, R_a , using the rand function in MATLAB.
3. If $\alpha \geq R_a$, the ray is absorbed, and the algorithm continues by identifying the receiving node on the surface.
4. If $\alpha < R_a$, the ray is reflected, and the direction of the reflected ray is calculated.
5. The surface that reflects the ray becomes the new starting surface for a new ray, and the search for the new receiving surface continues.
6. Once found, generate a new random number and compare it with the absorptivity coefficient.
7. Repeat steps 4, 5, and 6 until the surface with $\alpha \geq R_a$ is found.
8. Once found, identify the receiving element j for the ray, as in the previous algorithm.
9. Update the counter N_{ij} .

The flowchart of the algorithm used is shown in the provided Figure 52.

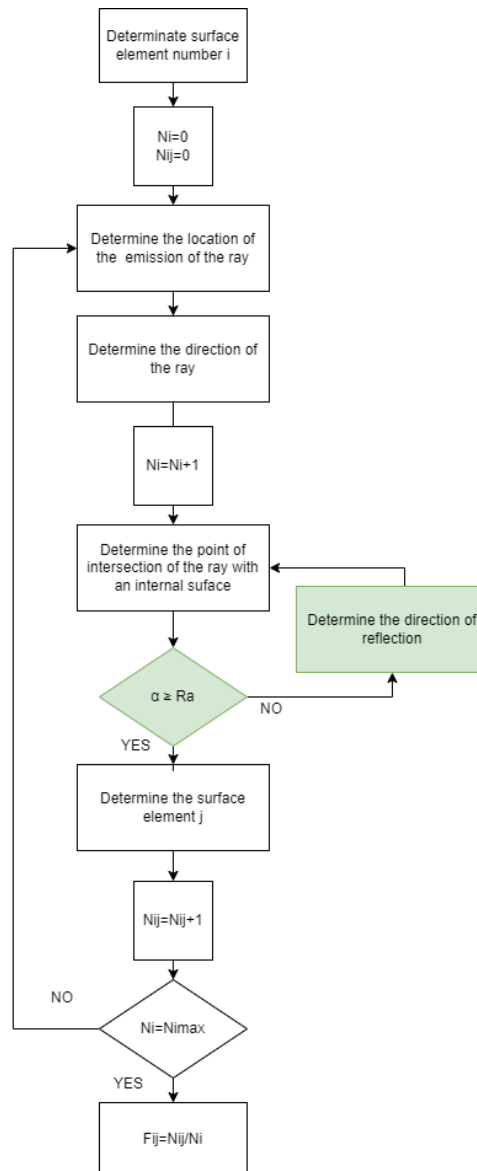


Figure 52: MCRT with Reflection Flowchart

Comparison with the previous version

In this subsection, a comparison is presented between the three algorithms in terms of execution speed and the accuracy of the results obtained by comparing the computed temperatures in the three cases with those obtained by analyzing the same model using the commercial software THERMAL DESKTOP.

For all simulations, the same environmental inputs, as shown in Table 8, were used, along with the same geometric model depicted in Figure 53.

Orbital Parameters	
Solar Constant	1367 [W/m ²]
Albedo coefficient	0.36
Planet IR flux	234 [W/m ²]
Eccentricity	0
Semi-major axis	6871 [km]
Inclination	97.5 [deg]
RAAN	107 [deg]
Argument of periapsis	0 [deg]
Simulation date	02/04/2020
Attitude	
Nadir pointing	-Z
Velocity pointing	-Y

Table 8: Environment Parameters for MCRT Comparison

Item Name	Colour	Sizes	Nodes	Center
Structure	blue	100x100x100	4x4x4	50,50,50
B1	red	50x50	3x3	50,50,20
B2	cyan	50x50	3x3	50,50,40
B3	magenta	50x50	3x3	50,50,60
B4	yellow	50x50	3x3	50,50,80

Table 9: GMM Parameters for MCRT Comparison

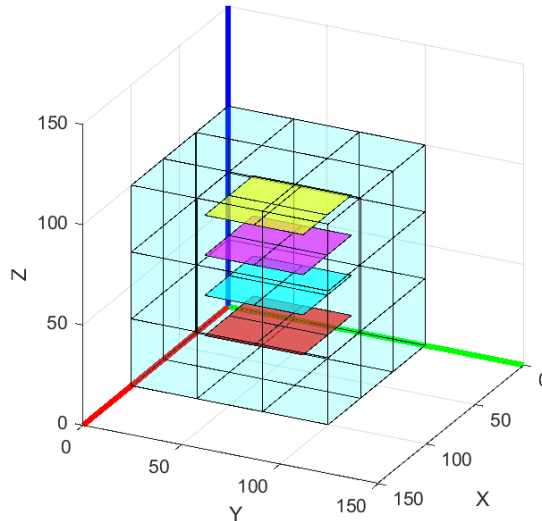


Figure 53: GMM Model for MCRT Comparison

From an initial comparison regarding the execution times of the three versions of the algorithm, it is immediately noticeable that even with the New First Iteration Version, the code's execution times are reduced by more than 70%, as shown in Table 10. This emphasizes how even adequate preprocessing of data structures is highly advantageous in terms of reducing execution times.

The New Version Second Iteration demonstrates a time saving of 99%, showcasing how leveraging the optimization of the MATLAB environment for matrix calculations is the best strategy for solving problems of this kind.

Regarding the algorithm implementing reflection, it is still faster compared to the first version, but since vectorization has not been applied, it remains slower than the New Version Second Iteration.

MCRT Version	Time [s]	Time Saving [%]
Previous Version	261.68	0
New version First iteration	67.05	74.38
New version Second iteration	2.39	99.09
New version with Reflection	71.04	72.85

Table 10: Comparison in MCRT Run Time

Table 11 presents the results regarding the temperature calculations.

$$Max Error = \left| \frac{T_{max} - T_{TD}}{T_{TD}} \right| \qquad Min Error = \left| \frac{T_{min} - T_{TD}}{T_{TD}} \right| \qquad (56)$$

Name Item		B1	B2	B3	B4	Structure
Thermal Desktop	T Min (°C)	11.339	11.443	11.614	11.160	9.648
	T Max (°C)	13.557	13.387	13.039	13.397	16.087
Previous Version	T Min (°C)	11.143	11.541	11.739	11.407	9.746
	T Max (°C)	13.760	13.556	13.582	13.840	16.357
	Min Error %	1.727	0.853	1.071	2.212	1.022
	Max Error %	1.498	1.259	4.160	3.306	1.678
New version First Iteration	T Min (°C)	11.327	11.418	11.594	11.056	9.606
	T Max (°C)	13.455	13.457	13.129	13.281	16.134
	Min Error %	0.105	0.220	0.175	0.931	0.431
	Max Error %	0.748	0.520	0.685	0.862	0.295
New version Second Iteration	T Min (°C)	11.324	11.421	11.577	11.059	9.603
	T Max (°C)	13.688	13.511	13.106	13.429	16.202
	Min Error %	0.134	0.199	0.320	0.906	0.461
	Max Error %	0.967	0.922	0.514	0.239	0.715
MCRT with Reflection	T Min (°C)	11.339	11.437	11.595	11.092	9.602
	T Max (°C)	13.620	13.450	13.082	13.425	16.201
	Min Error %	0.002	0.056	0.167	0.612	0.470
	Max Error %	0.464	0.466	0.331	0.216	0.711

Table 11: Comparison of all the MCRT algorithm version with TD

The analysis of the data shows negligible error values calculated on the maximum and minimum temperature peaks. The previous version of the algorithm also shows very low errors, but the new versions are able to implement a calculation that is not only more efficient but also more accurate. This is due to the updates made regarding the choice of the starting point of the rays and the uniform distribution in which they are emitted. In conclusion, the results obtained show that the updates made to the code significantly improve its performance.

Chapter 4

Validation and Case Study

Comparison with Thermal Desktop

In this section, the results of the comparisons between the S2T2 software and the commercial code THERMAL DESKTOP® are presented. It is one of the most widely used tools by thermal engineers to determine the temperatures of a spacecraft. To perform this comparison, four simple models were prepared in both S2T2 and TD, consisting of a 1U structure with an additional item to be analyzed. For each item, four cases were analyzed:

Case1: Power consumption off, additional conduction off

Case2: Power consumption on, additional conduction off

Case3: Power consumption off, additional conduction on

Case4: Power consumption on, additional conduction on

Additionally, for each item and each case, two simulations were conducted using S2T2: one using MCRT new version second iteration, and the other using MCRT with reflection.

Regarding the power dissipation, a thermal load of 1W was applied. For the conduction analysis, a link with $k = 52$ [W/(k*m)], $A = 1$ [cm²], and $L = 5$ [mm] was used.

The simulations were conducted using the orbit parameters provided in Table 12.

Orbital Parameters	
Eccentricity	0
SMA	6871 [km]
Inclination	97.5 [deg]
RAAN	10 [deg]
Argument of Periapsis	0 [deg]
Simulation Date	05-Apr-2021
Attitude	
Nadir	-Z
Velocity	-Y

Table 12: Orbit parameters for item comparison

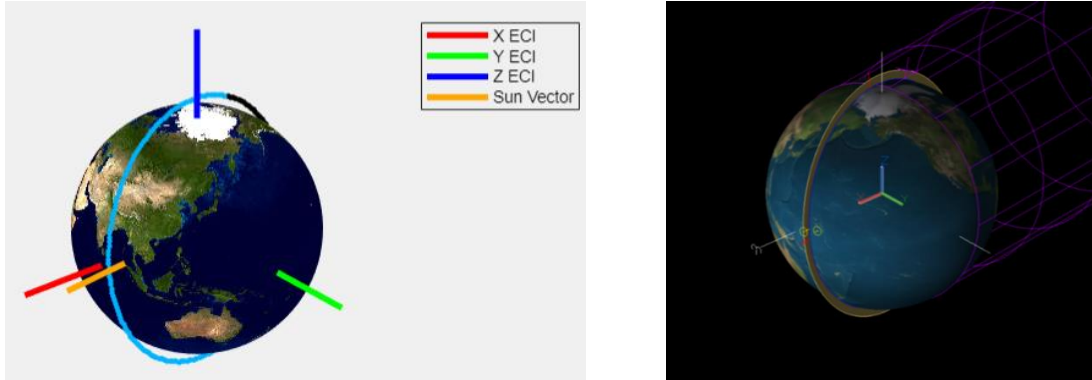


Figure 54: Orbit representation S2T2 (left), TD (right)

For each item, a table is presented comparing the temperatures calculated using MCRT New Version Second Iteration, MCRT with Reflection, and Thermal Desktop. The tables include the temperature difference calculated for both code versions, as well as the relative error calculated as follows:

$$Relative\ error = \left| \frac{\Delta T}{T_{max}^{TD} - T_{min}^{TD}} \right| \quad (57)$$

Board

Case1

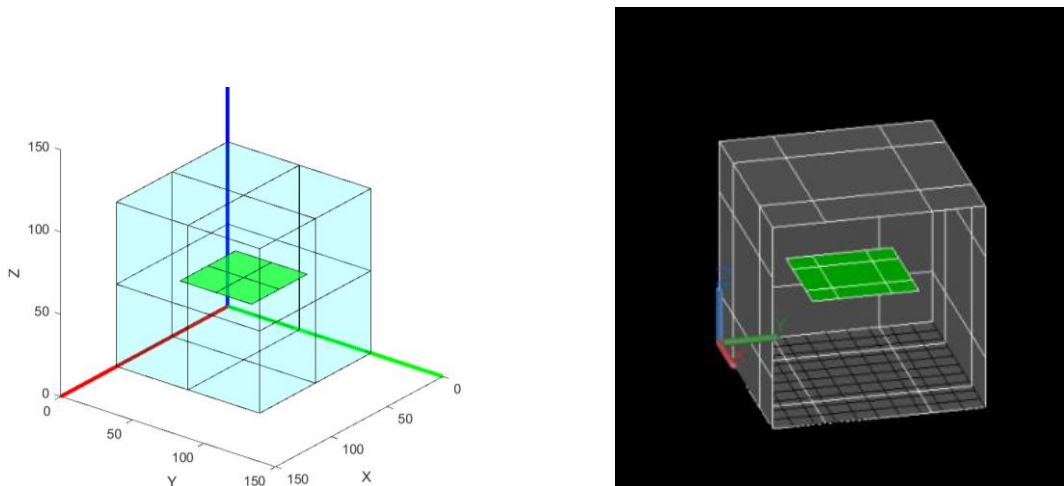


Figure 55: Board comparison S2T2 (left), TD (right)

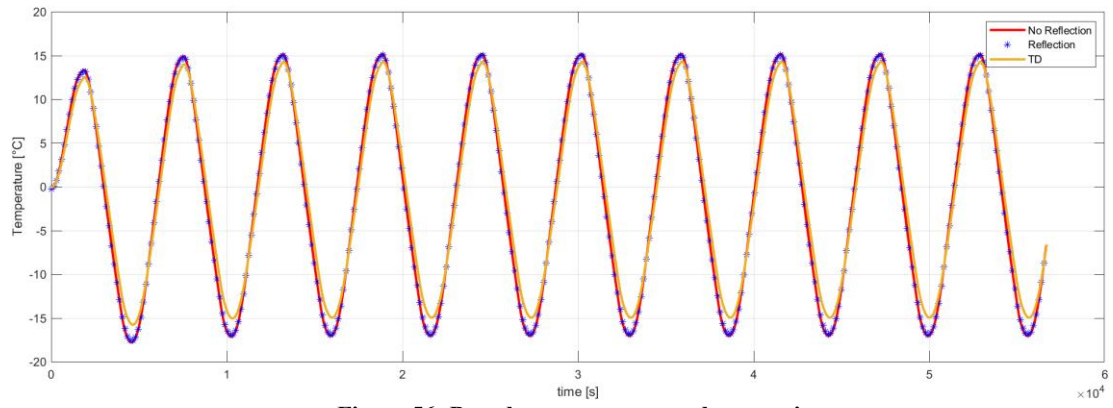


Figure 56: Board temperature trend comparison

Case 2

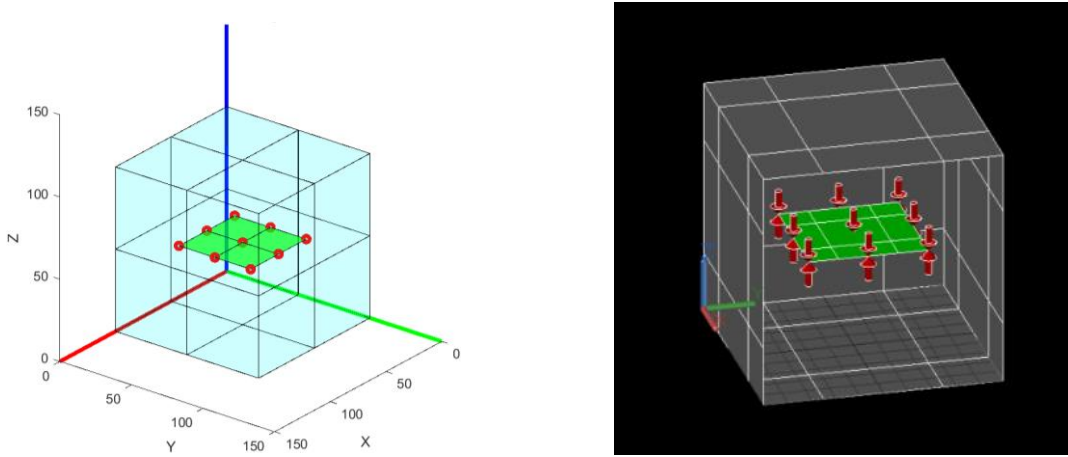


Figure 57: Board with dissipation comparison S2T2 (left), TD (right)

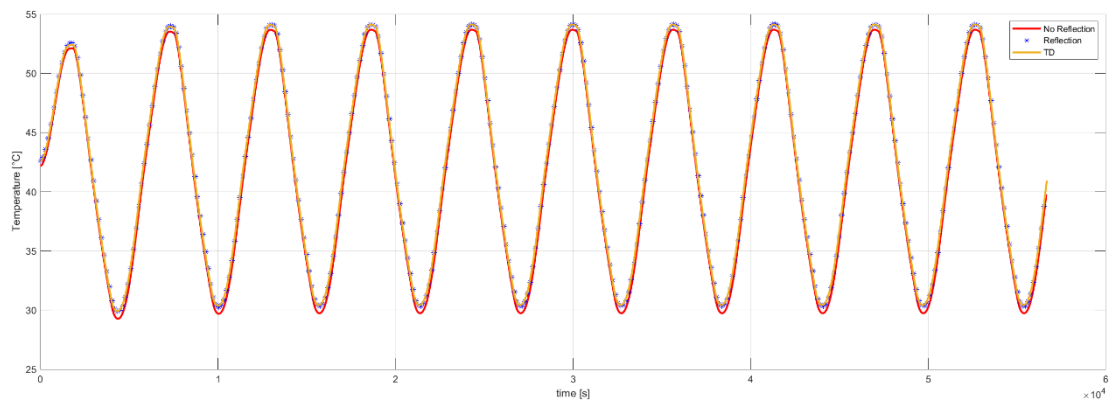


Figure 58: Board with dissipation temperature trend comparison

Case3

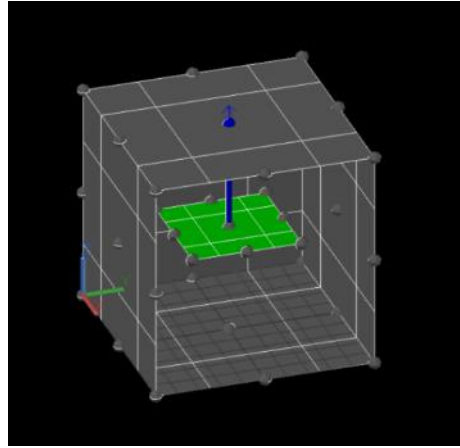
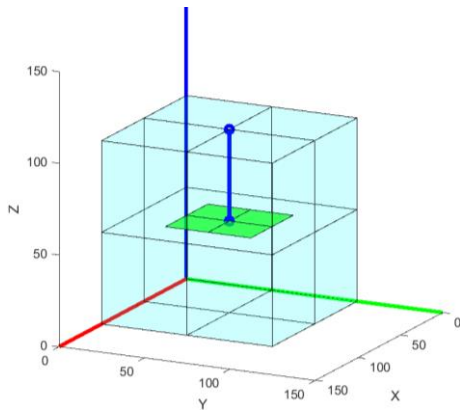


Figure 59: Board with additional conduction comparison S2T2 (left), TD (right)

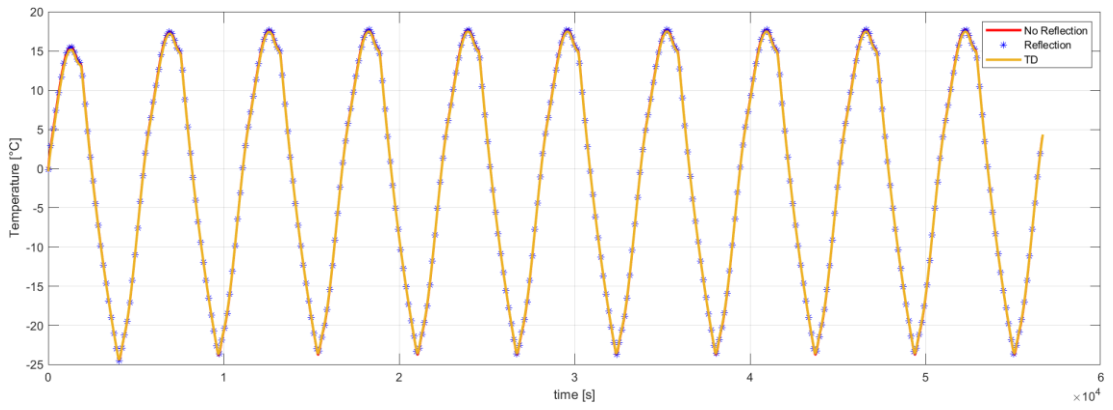


Figure 60: Board with additional conduction temperature trend comparison

Case 4

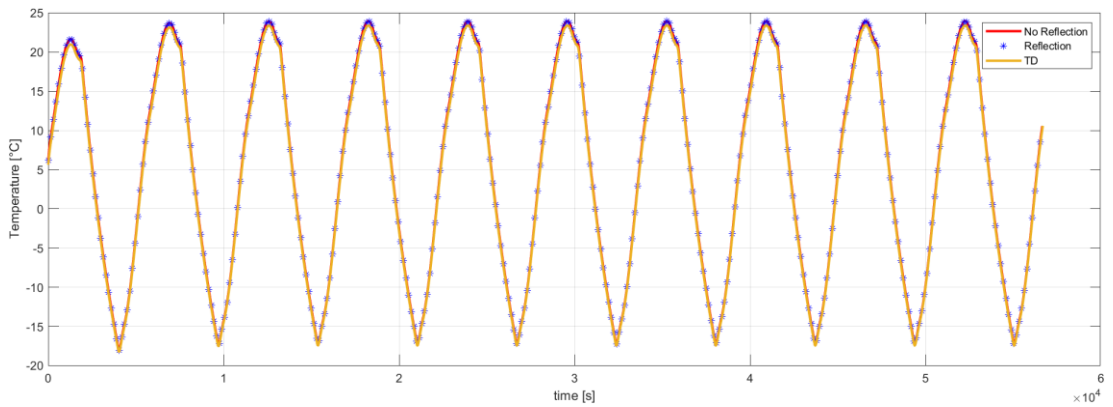


Figure 61: Board with dissipation and additional conduction temperature trend comparison

		Thermal Desktop [°C]	S2T2 no Ref [°C]	ΔT [°C]	Relative Error [%]	S2T2 [°C]	ΔT [°C]	Relative Error [%]
Case1	Min	-16.23	-17.77	1.54	5.09	-17.61	1.38	4.58
	Max	13.92	15.20	1.28	4.25	15.10	1.18	3.91
Case2	Min	30.24	29.32	0.93	4.00	30.32	0.08	0.34
	Max	53.45	53.75	0.30	1.30	54.48	1.03	4.45
Case3	Min	-24.39	-24.46	0.07	0.16	-24.46	0.07	0.16
	Max	17.50	17.75	0.25	0.60	17.75	0.25	0.60
Case4	Min	-18.83	-18.91	0.09	0.20	-18.88	0.05	0.13
	Max	23.40	23.78	0.38	0.89	23.78	0.38	0.89

Table 13: Board results

In the case of the boards, it can be seen from Table 13 that in all four cases, the maximum relative error is around 5%, with values of ΔT barely exceeding 1°C.

Parallelepiped

Case1

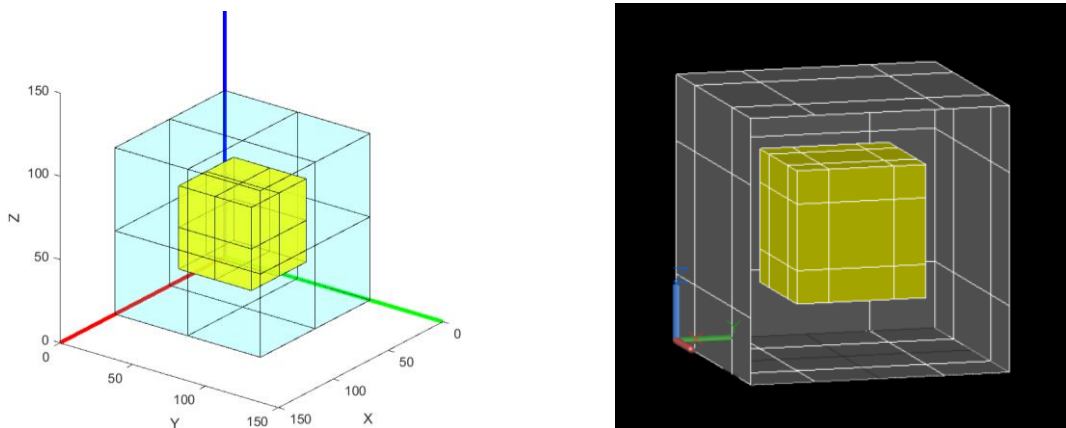


Figure 62: Parallelepiped comparison S2T2 (left), TD (right)

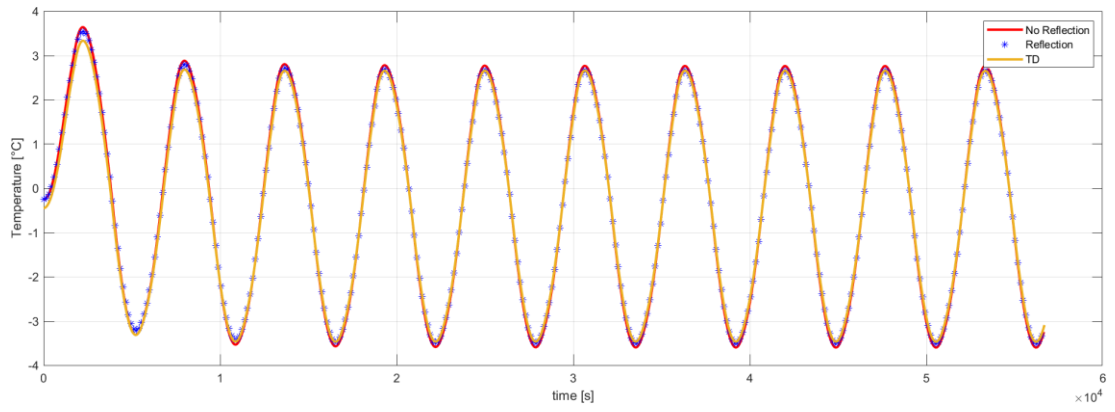


Figure 63: Parallelepiped temperature trend comparison

Case2

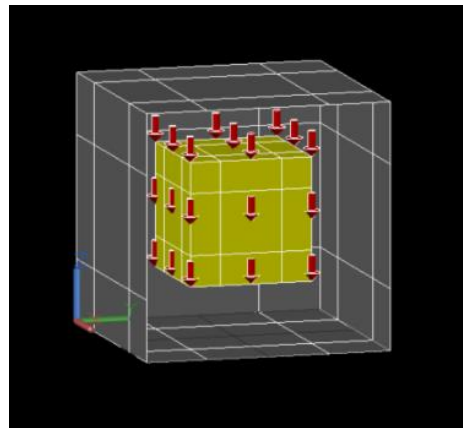
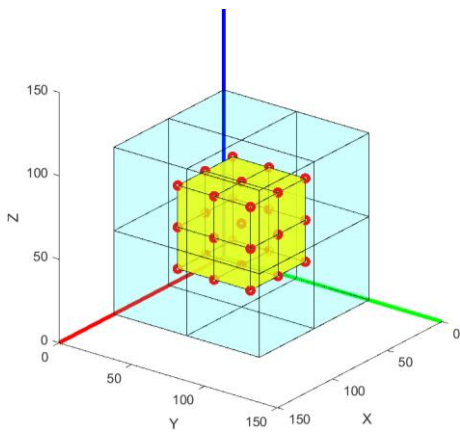


Figure 64: Parallelepiped with dissipation comparison S2T2 (left), TD (right)

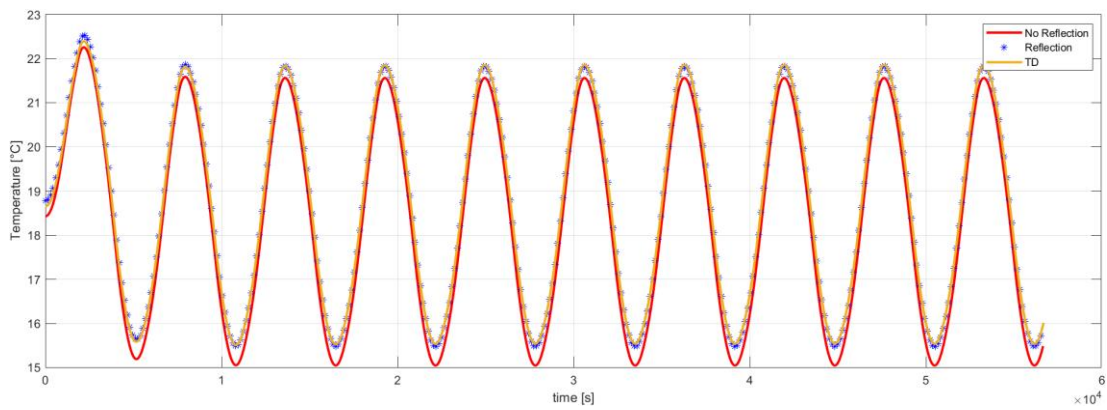


Figure 65: Parallelepiped with dissipation temperature trend comparison

Case3

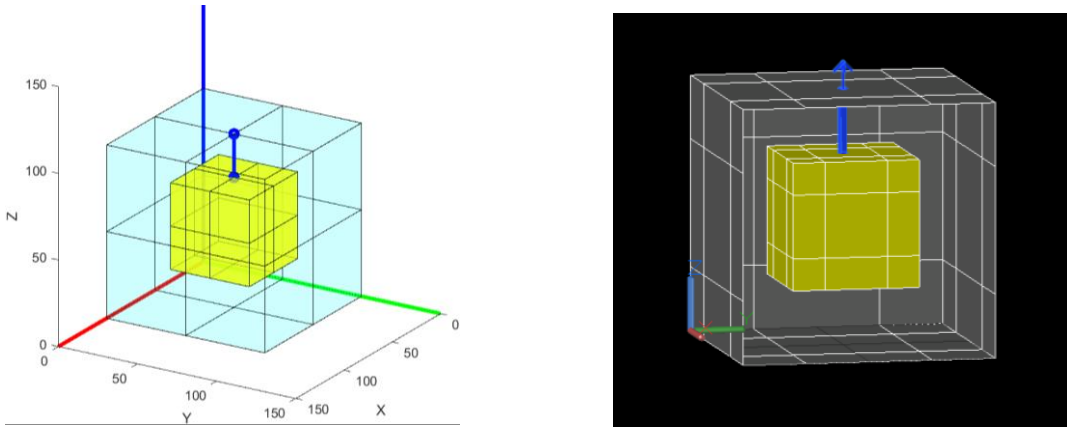


Figure 66: Parallelepiped with additional conduction comparison S2T2 (left), TD (right)

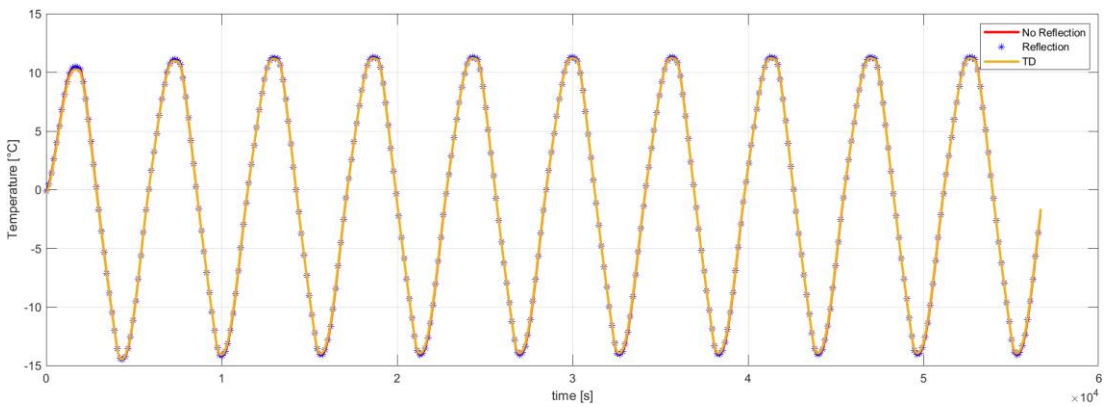


Figure 67: Parallelepiped with additional conduction temperature trend comparison

Case4

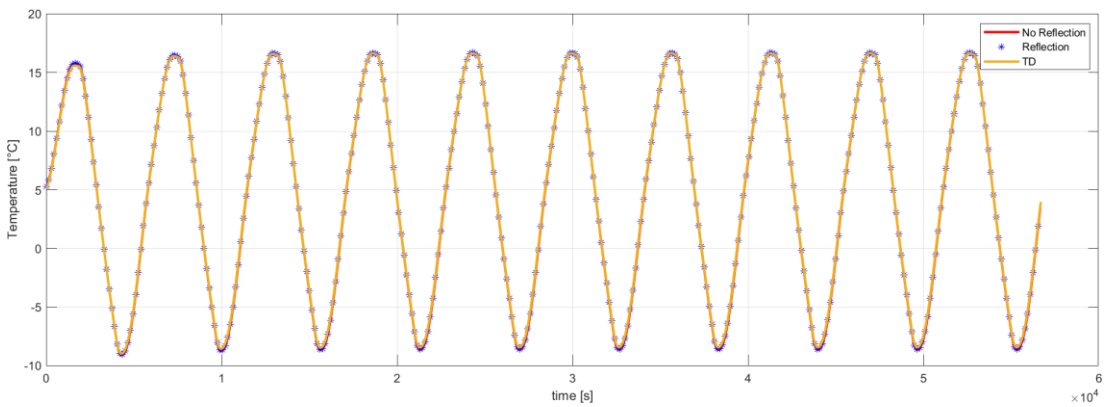


Figure 68: Parallelepiped with dissipation and additional conduction temperature trend comparison

		Thermal Desktop [°C]	S2T2 no Ref [°C]	ΔT [°C]	Relative Error [%]	S2T2 [°C]	ΔT [°C]	Relative Error [%]
Case1	Min	-3.47	-3.60	0.13	1.89	-3.51	0.04	0.57
	Max	3.34	3.64	0.31	4.49	3.55	0.21	3.15
Case2	Min	15.51	15.04	0.47	6.76	15.47	0.03	0.50
	Max	22.41	22.27	0.14	2.00	22.54	0.14	2.00
Case3	Min	-14.47	-14.42	0.05	0.19	-14.41	0.06	0.22
	Max	11.24	11.27	0.02	0.10	11.26	0.02	0.07
Case4	Min	-9.08	-9.04	0.04	0.16	-9.04	0.05	0.18
	Max	16.66	16.70	0.04	0.14	16.70	0.04	0.14

Table 14: Parallelepiped results

In the case of the parallelepiped, it is interesting to observe Figure 65, it shows the effectiveness of reflection. With the introduction of dissipation, in fact, the radiative exchange between structure and parallelepiped plays a fundamental role. The trend in the case without reflection has a small error, in the order of 6%, with completely negligible ΔT . However, the almost perfect superposition of the S2T2 trends with reflection and TD permits to appreciate the increase in accuracy obtained with the introduction of this new algorithm.

Cylinder

Case1

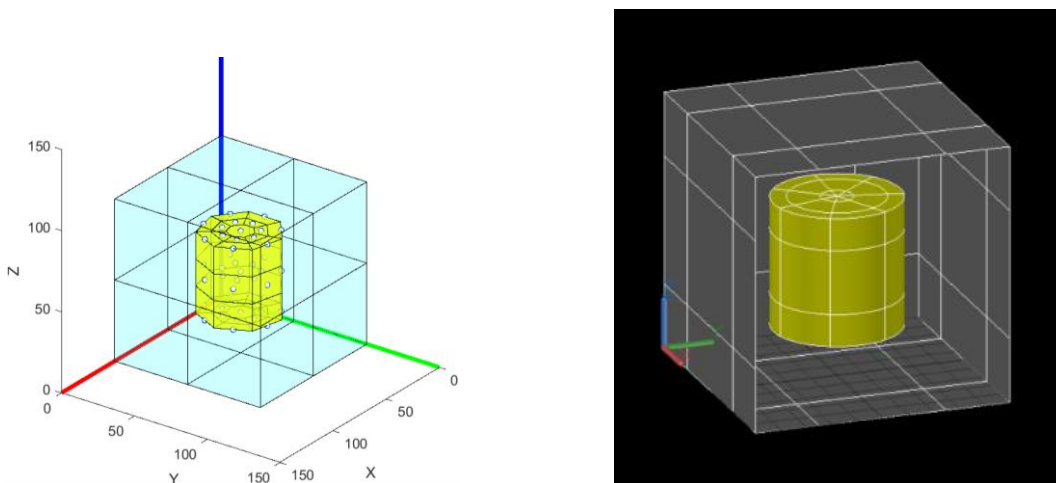


Figure 69: Cylinder comparison S2T2 (left), TD (right)

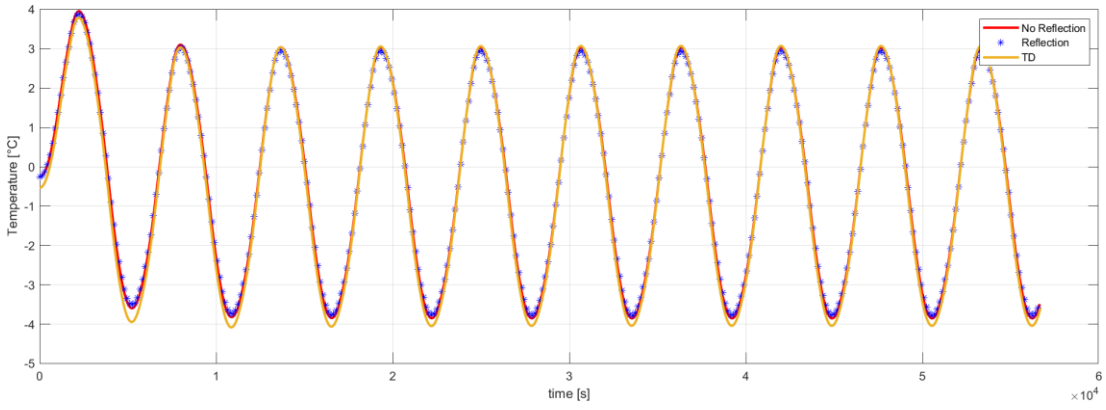


Figure 70: Cylinder temperature trend comparison

Case2

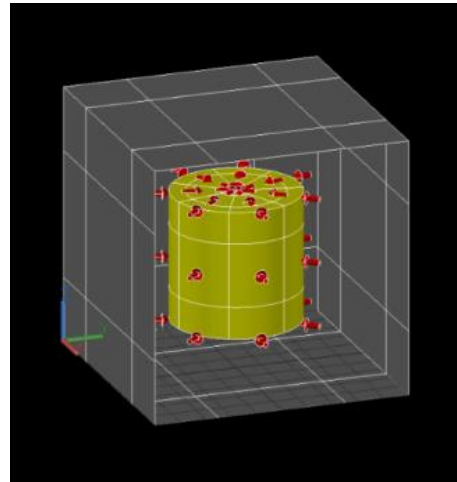
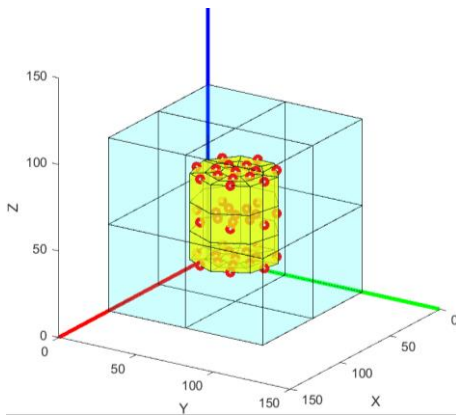


Figure 71: Cylinder with dissipation comparison S2T2 (left), TD (right)

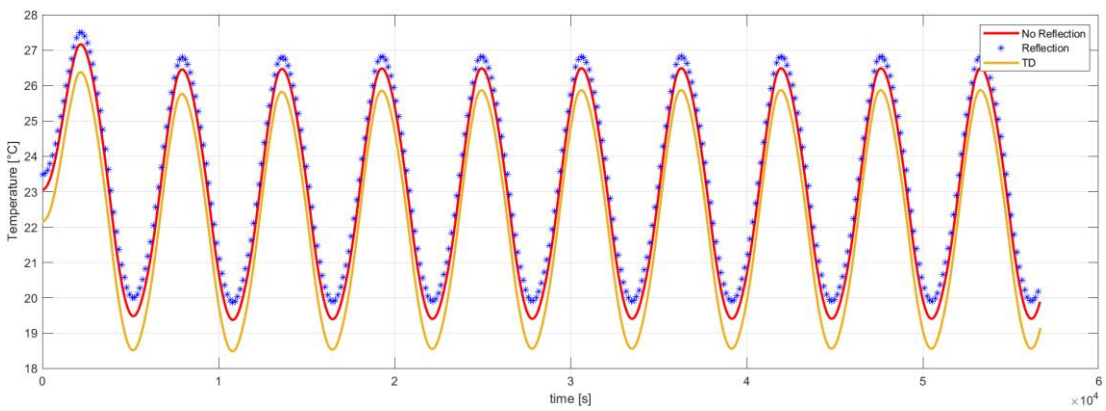


Figure 72: Cylinder with dissipation temperature trend comparison

Case3

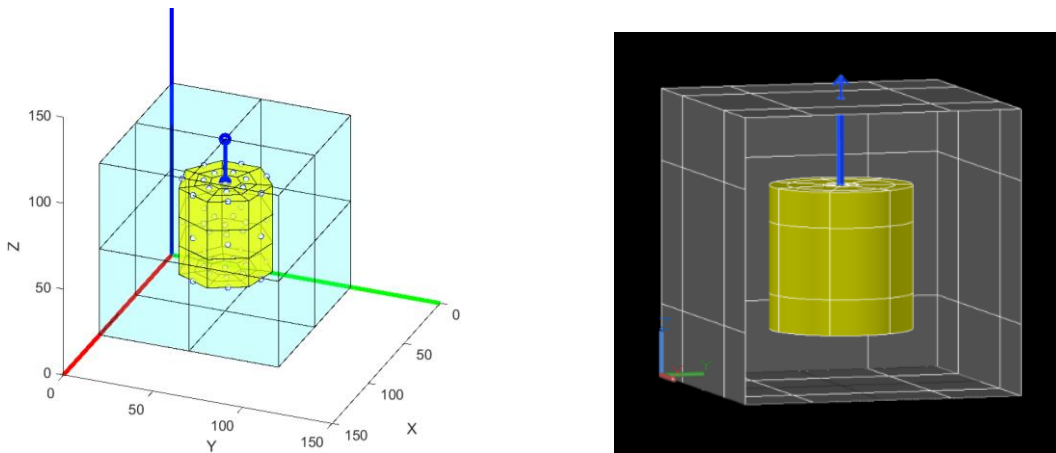


Figure 73: Cylinder with additional conduction comparison S2T2 (left), TD (right)

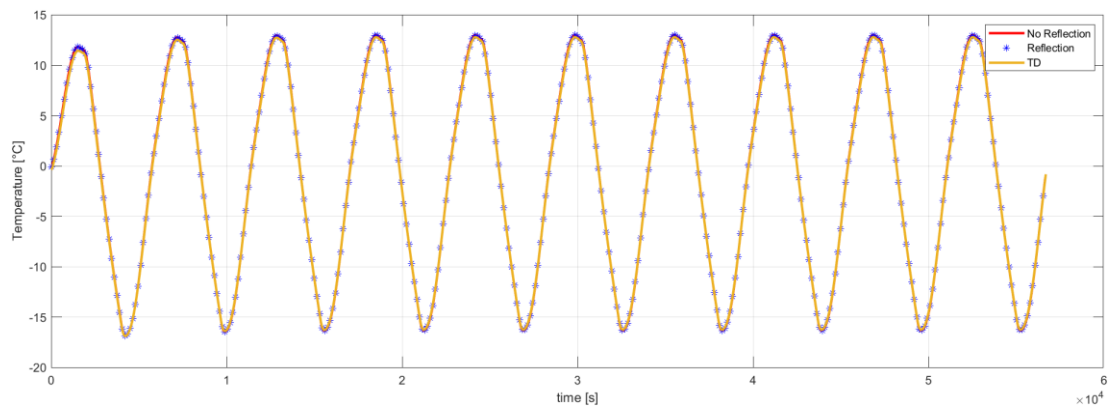


Figure 74: Cylinder with additional conduction temperature trend comparison

Case4

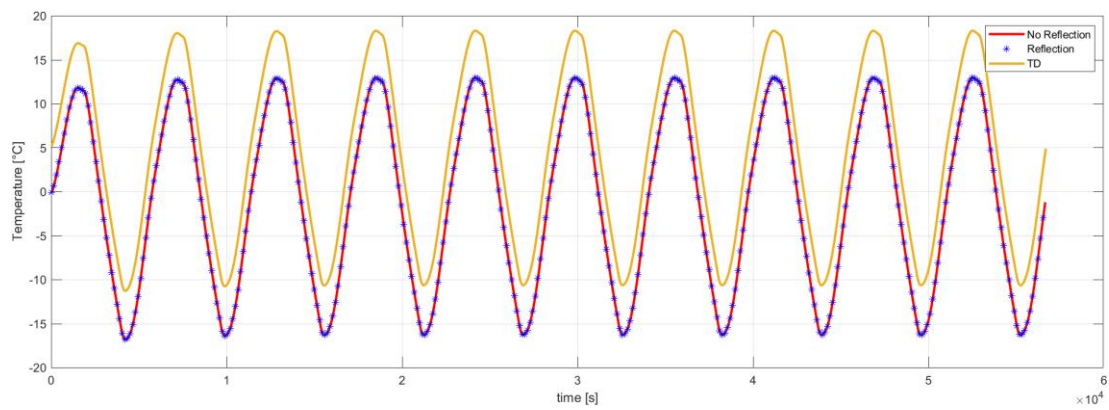


Figure 75: Cylinder with dissipation and additional conduction temperature trend comparison

		Thermal Desktop [°C]	S2T2 no Ref [°C]	ΔT [°C]	Relative Error [%]	S2T2 [°C]	ΔT [°C]	Relative Error [%]
Case1	Min	-4.08	-3.85	0.23	2.91	-3.78	0.30	3.87
	Max	3.79	3.95	0.17	2.13	3.88	0.09	1.18
Case2	Min	18.48	19.37	0.89	11.26	19.87	1.39	17.57
	Max	26.39	27.17	0.79	9.96	27.52	1.13	14.31
Case3	Min	-16.90	-16.84	0.06	0.20	-16.83	0.07	0.22
	Max	12.81	12.99	0.18	0.60	12.98	0.17	0.59
Case4	Min	-11.48	-16.83	5.36	17.97	-16.83	5.35	17.96
	Max	18.32	12.99	5.34	17.91	12.98	5.34	17.92

Table 15: Cylinder results

Regarding the cylinders, in case 2 the relative error is rather high, although the calculated ΔT is about 1.4°C, the largest error is present in case 4 where the ΔT exceeds 5°C. These errors are due to the geometric difference between the models; in S2T2, the cylinder is represented as a prism, so its surfaces are planar, whereas, in the case of TD, the model has curved surfaces. This inevitably leads to an error in the calculation of the view factors and thus in the radiative exchange between the item and the structure. That said, the results fall within a margin of 15°C as suggested by ECSS for the initial project stages [16].

Solar Panel

Case1

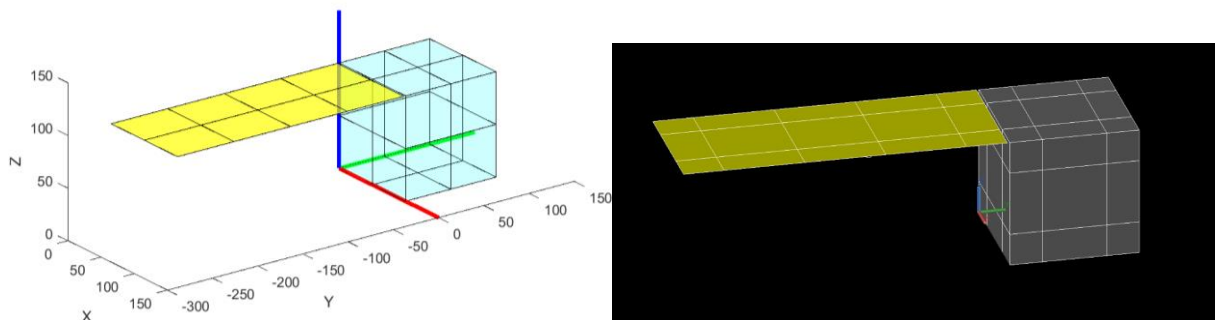


Figure 76: Solar panel comparison S2T2 (left), TD (right)

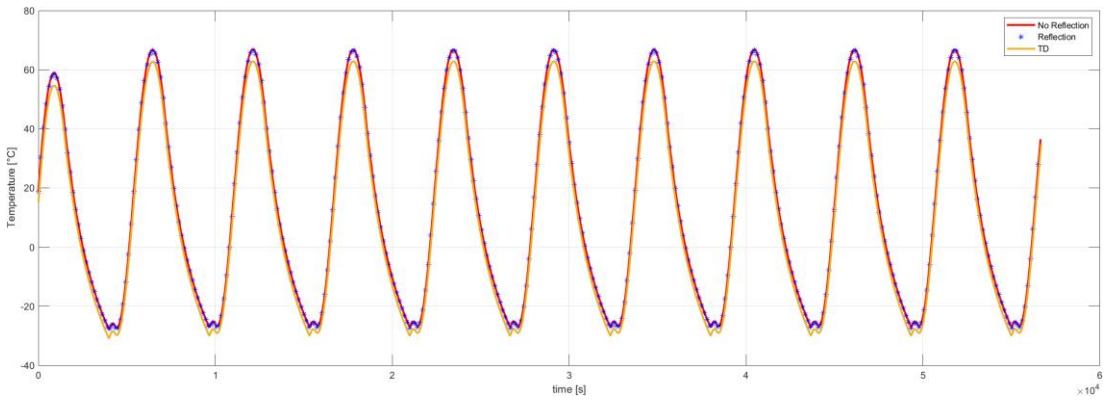


Figure 77: Solar panel temperature trend comparison

Case2

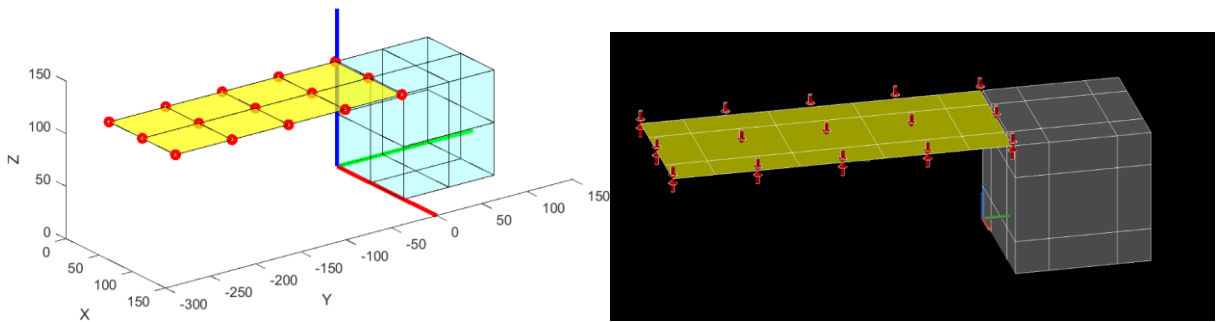


Figure 78: Solar panel with dissipation comparison S2T2 (left), TD (right)

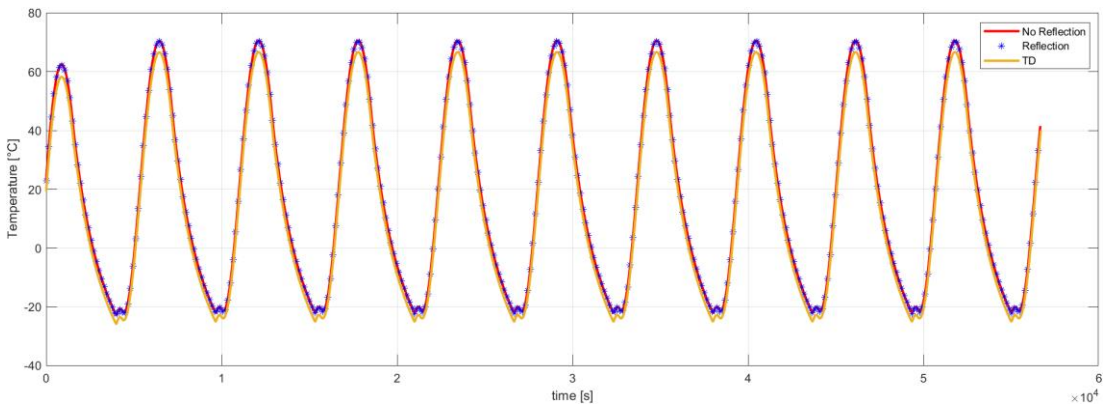


Figure 79: Solar panel with dissipation temperature trend comparison

Case3

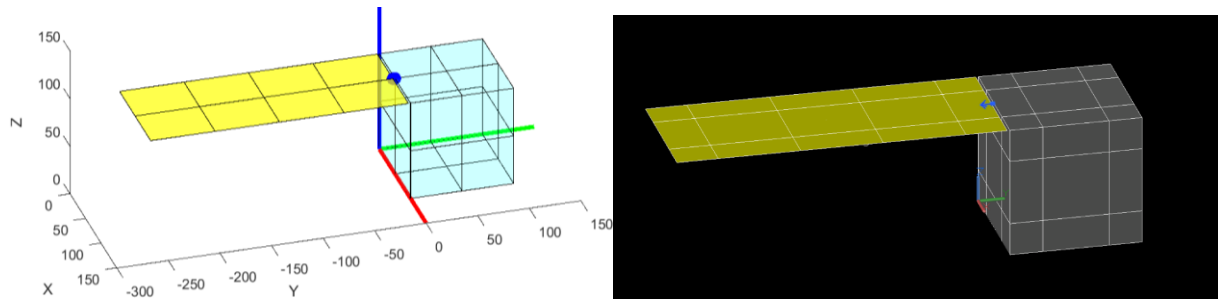


Figure 80: Solar panel with additional conduction comparison S2T2 (left), TD (right)

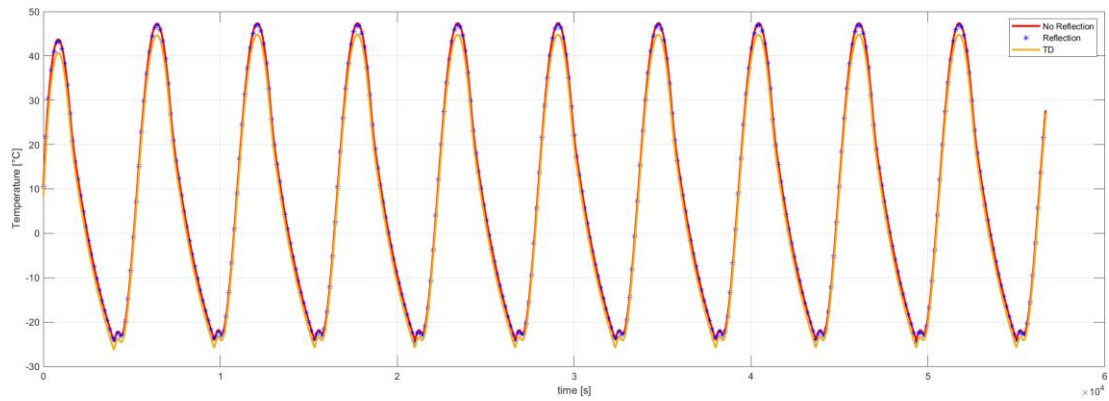


Figure 81: Solar panel with additional conduction comparison S2T2 (left), TD (right)

Case4

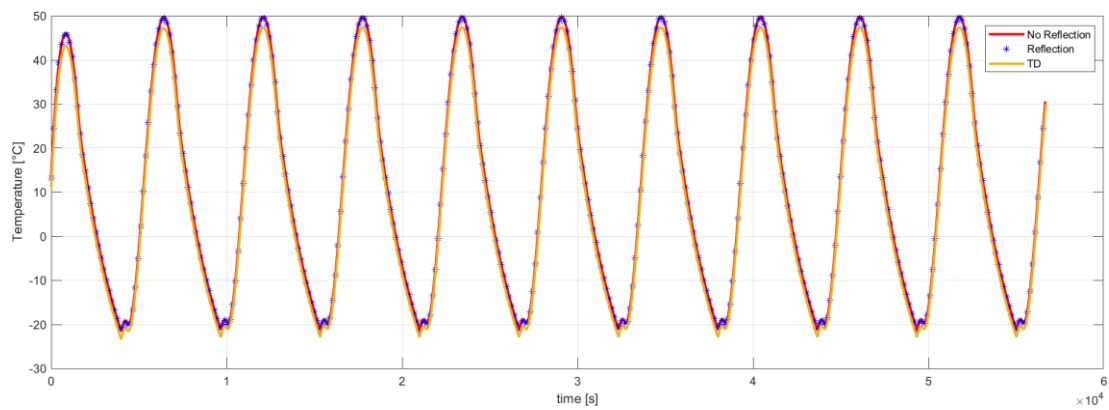


Figure 82: Solar panel with dissipation and additional conduction temperature trend comparison

		Thermal Desktop [°C]	S2T2 no Ref [°C]	ΔT [°C]	Relative Error [%]	S2T2 [°C]	ΔT [°C]	Relative Error [%]
Case1	Min	-30.83	-27.80	3.04	3.23	-28.17	2.66	2.83
	Max	63.14	67.37	4.24	4.51	67.05	3.91	4.16
Case2	Min	-25.81	-22.90	2.92	3.15	-23.21	2.60	2.81
	Max	66.81	70.97	4.16	4.49	70.69	3.88	4.19
Case3	Min	-26.59	-24.78	1.81	2.44	-25.10	1.49	2.01
	Max	47.68	50.05	2.37	3.19	49.75	2.07	2.78
Case4	Min	-23.42	-21.69	1.73	2.34	-21.92	1.50	2.03
	Max	50.38	52.64	2.26	3.06	52.45	2.07	2.80

Table 16: Solar panel results

For the analysis of solar panels, Table 16 shows low relative errors with a maximum in case 2 of about 4.5%. This error is attributable to the difference between the two models; in the case of the solar panel, the difference with the model implemented in TD is the calculation of external heat fluxes. The difference between the two models lies in the computation of the S/C-Earth view factors: while in TD this is intrinsically performed using a Monte Carlo ray tracing method, in S2T2 it is performed in an analytical way, using the approximation of flat plate absorbing and emitting on one side [16] and solving the problem of satellite self-shadowing by casting a single ray from every surface element of the S/C to the centre of the heat source, which in this case is the Earth. Rays that, on their path, intersect other satellite surfaces determine the shadowed elements, for which the view factor with the heat source is set to 0.

Spei-Satelles Mission

Mission Objectives

The Spei Satelles mission originates from the will to diffuse a message of hope by Pope Francis to all people in the world. This message of hope, shared for the first time the 27th of March 2020 during the COVID pandemic and known as *Statio Orbis*, has been transcribed into a miniaturized chip in binary language by the Italian National Council of Researches (Consiglio Nazionale delle Ricerche – CNR). The miniaturized chip is referred to as “Nanobook” and it is hosted onboard the SpeiSat spacecraft. Hence, the SpeiSat symbolically becomes “a guardian of hope”, as the name Spei Satelles translates from Latin.

Technically speaking, Spei Satelles is a telecommunications mission that sends messages that are received and shared with people through a network of amateur ground stations. Therefore, the main mission objective is to transmit sentences of hope from space to ground. The sentences are transmitted in Italian, English and Spanish.

Furthermore, as a secondary mission, the spacecraft aims at collecting data to characterize the CubeSat behavior and the space environment. A Sensing Suite, equipped with an Inertial Measurement Unit, magnetometers and about 30 temperature sensors, is integrated within the spacecraft to fulfil the secondary mission objectives. The data collected will be used to: validate the thermal and attitude models that supported the analyses during the design, to assess the behaviour of several platform items, and to characterise the magnetic environment.

The Spei Satelles mission has five objectives.

Primary mission objectives:

1. To host the Nanobook and bring it to LEO.
2. To transmit text messages of hope to ground stations. The messages are sentences collected in a file saved on the onboard computer memories. They are transmitted in three languages: Italian, English and Spanish.

Secondary mission objectives:

3. To characterize the internal and external thermal environment of the spacecraft.
4. To characterize the internal magnetic field of the spacecraft and map the Earth magnetic field.
5. To characterize the angular motion of the spacecraft.

Mission Phases

The description of the Concept of Operations (ConOps) is reported in detail in this section. The scenario is divided into phases and each phase is further split into sub-phases. For each phase and sub-phase, specific objectives have been identified, together with initial and final events/conditions, environmental conditions, and duration, as summarized in Table 17.

MISSION PHASE	MISSION SUB-PHASES	DESCRIPTION
Integration & pre-launch (IPLP)	Transportation to launch base (TRP) Integration in the PSL12U deployer (DIP – deployer integration phase) Integration in the ION carrier (IIP – ION Integration Phase) Integration on Falcon9 LV (LIP – Launcher Integration Phase)	Objective: to get ready for launch into orbit Duration: < 1 months Initial condition / start event: SpeiSat shipped to VSFB (CA, USA) Final condition / end event: SpeiSat integrated into the PSL12U deployer onboard the ION carrier and installed on Falcon9 LV Environment: VSFB
Launch and Early Operations Phase (LEOP)	Launch Phase (LAP) Pre-Separation Phase (PSP) Separation Phase (SEP) Commissioning Phase (CMP)	Objective: to get ready to start the mission in orbit Duration: < 3 months (target < 6 weeks) Initial condition / start event: Falcon9 Liftoff Final condition / end event: in-orbit commissioning completed Environment: launch + orbit
Mission Operations Phase (MOP)	Primary Mission Phase (PMP) Extended Mission Phase (EMP) (TBC)	Objective: to execute the mission Duration: > 6 months (target > 1 year) Initial condition / start event: command from ground to start nominal operations Final condition / end event: mission completion Environment: orbit
End-of-Life Phase (ELP)	Decommissioning Phase (DEP) Disposal Phase (DSP)	Objective: to dismiss the spacecraft after mission completion Duration: < 25 years (target < 5 years) Initial condition / start event: mission accomplished Final condition / end event: SPEISAT burned up in Earth atmosphere Environment: orbit

Table 17: SPEI SATELLES High-level ConOps

The operations timeline in Figure 83 shows the main steps planned for every mission phase and event. After the launch on 12th of June 2023, the ION spacecraft is released and the operator company will notify the spacecraft orbit TLEs and the estimated SPEISAT separation time. Using the Two-Line Element set, the Flight Dynamics Team will perform the orbit determination of the ION spacecraft. From the orbit determination and the estimated separation time of SpeiSat, the Operations Team will review the Mission Operations Plan to adjust the communications windows with the ground stations for the Separations Phase and the Commissioning Phase.

At the first telemetry signal acquisition from the ground station, the Commissioning Phase starts. The Operations Team will monitor the spacecraft's health status from the spacecraft telemetry, through the data provided by the Sensing Suite and the spacecraft and establish two-way

communication to execute the commissioning procedure. The transition in contingency mode can be commanded from ground in case of need. After the initial six months from the SpeiSat separation, the mission could be extended, with the same tasks as for the nominal mission.

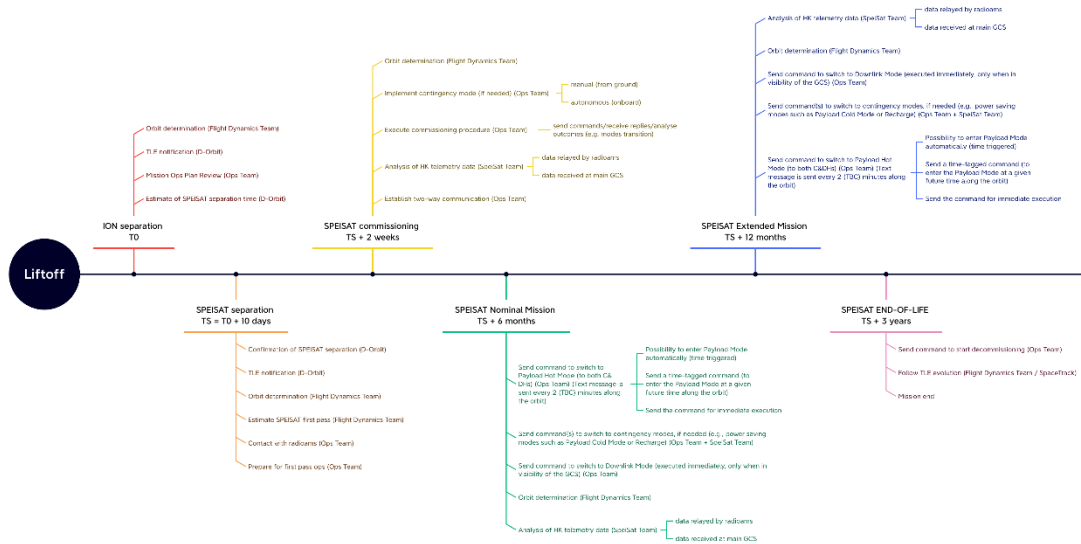


Figure 83: Spei Satellites operations time line

Spacecraft Architecture and Configuration

The Spei Satelles satellite is a 3U CubeSat designed upon the platform developed at Politecnico di Torino in the framework of its CubeSat programme.



Figure 84: Final configuration of SPEISAT

The spacecraft was designed to guarantee the full redundancy of the transmission function; therefore, the SpeiSat is equipped with two independent C&DHs and communication systems. The

ensemble of one C&DH and one communication system constitutes a BUS. The two BUSES are interfaced and coordinated thanks to an interface and distribution system of onboard functions (Backplane). The two BUSES are independent for most of the functions; however, the BUS1 can turn off the BUS2 to save power during specific mission phases. Furthermore, the two BUSES alternate for the transmission and their arbitration is coordinated by the arbitration circuit located on the Backplane. The Backplane also performs the function to distribute power among all subsystems, interfacing the Electrical Power System with all other components.

The EPS is constituted of four solar panels body mounted on the external faces of the spacecraft and a lithium-ion battery pack.

The spacecraft is equipped with a magnetic attitude stabilization system made of permanent magnets and hysteresis rods to stabilize the attitude and dump attitude oscillations.

A Sensing Suite equipped with an IMU and up to 32 temperature sensors is used to monitor the state of health of the platform and to collect the data required to fulfil the scientific goals of the secondary mission.

As the payload, the platform symbolically hosts the nanobook provided by CNR, while the sentences to be transmitted are saved in a file stored in both the C&DHs' memory.

These systems are installed in an Al 7075 aluminium alloy structure suitably treated with Surtec plus hard anodizing where required (e.g., rails).

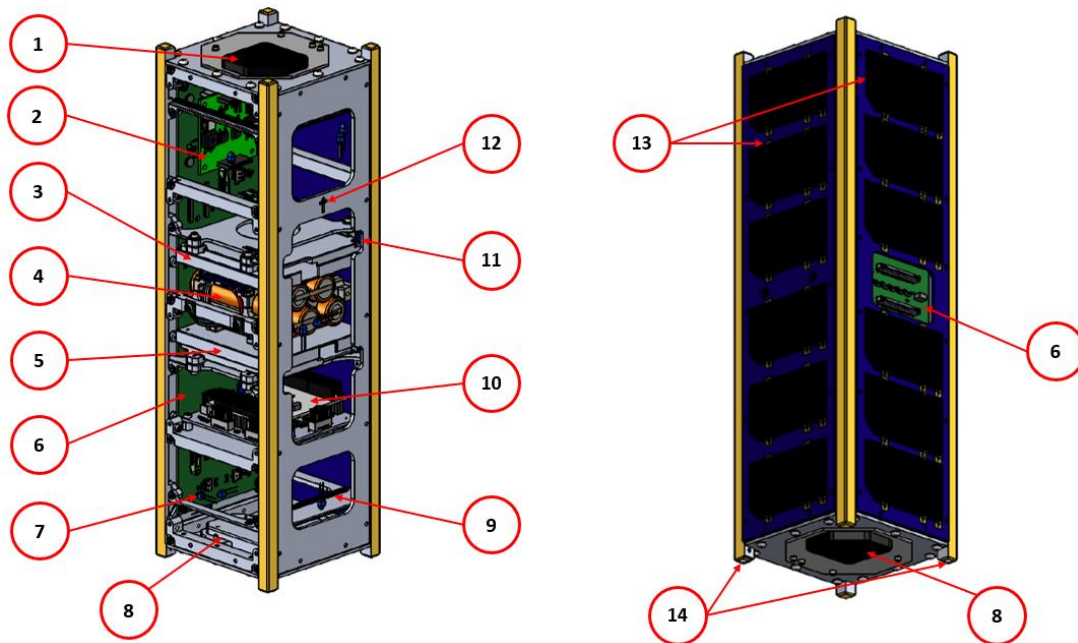


Figure 85: Spei Satelles architecture

Element #	Quantity	Component
1	1	ComSys 2
2	1	DET
3	1	Command & Data Handling 2
4	1	Battery
5	1	Command & Data Handling 1
6	1	Backplane
7	32	Temperature sensor
8	1	ComSys 1
9	6	Hysteresis rod
10	1	Sensing suite
11	2	Permanent Magnet
12	1	Nanobook
13	4	Solar Panels
14	2	Deployment Switches

Table 18: List of components

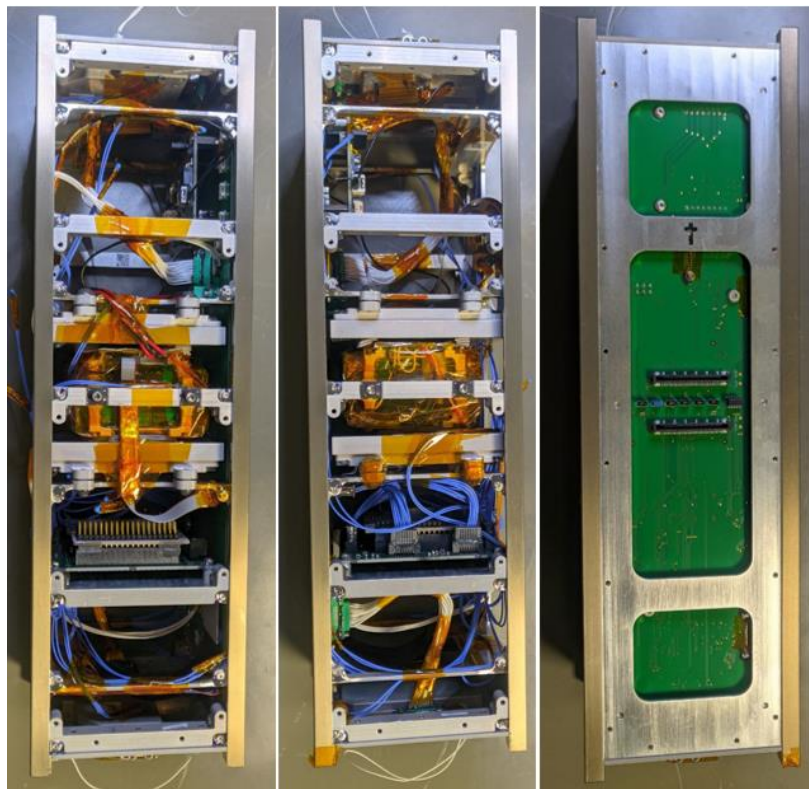


Figure 86: Internal view of faces -Y (left), +Y (central), +X (right)

Thermal Analysis

Requirement Temperatures

The first step for thermal analysis concerns defining the temperature requirements for each component installed on board. In particular, it is necessary to identify not only the operative temperature ranges of the components but also the survival temperature ranges. Operative temperatures indicate the limits in which the component can operate, while survival temperatures indicate the limits in which the component will not fail if it is kept off. Table 19: Temperature requirements.

Component	Operational MIN [°C]	Operational MAX [°C]	Survival MIN [°C]	Survival MAX [°C]
Antenna 1	-100	100	-120	120
Antenna 2	-100	100	-120	120
Backplane	-40	85	-55	125
Battery	0	40	-10	50
C&DH 1	-30	45	-40	75
C&DH 2	-30	45	-40	75
Solar Cells	-55	125	-65	150
ComSys 1	-30	60	-40	70
ComSys 2	-30	60	-40	70
DET	-40	80	-50	90
Sensing Suite	-40	80	-50	90

Table 19: Temperature requirements

Cold Case and Hot Case

At this point, it is necessary to identify the two thermal worst-case scenarios. This definition is derived from the analysis of the different mission phases and the comparison of the dissipations obtained in the different operative modes. Two extreme cases called Hot Case and Cold Case were identified. In the hot case, the S/C experiences the highest environmental heating, and it is in the operative mode with the highest power consumption, the Payload Hot operative mode. In the cold case instead, the S/C is exposed to the lowest environmental heating of its life and it is in the operative mode with the lowest power consumption, the Recharge operative mode. Figure 87 shows the different orbits for the two case studies, generated with the S2T2 software.

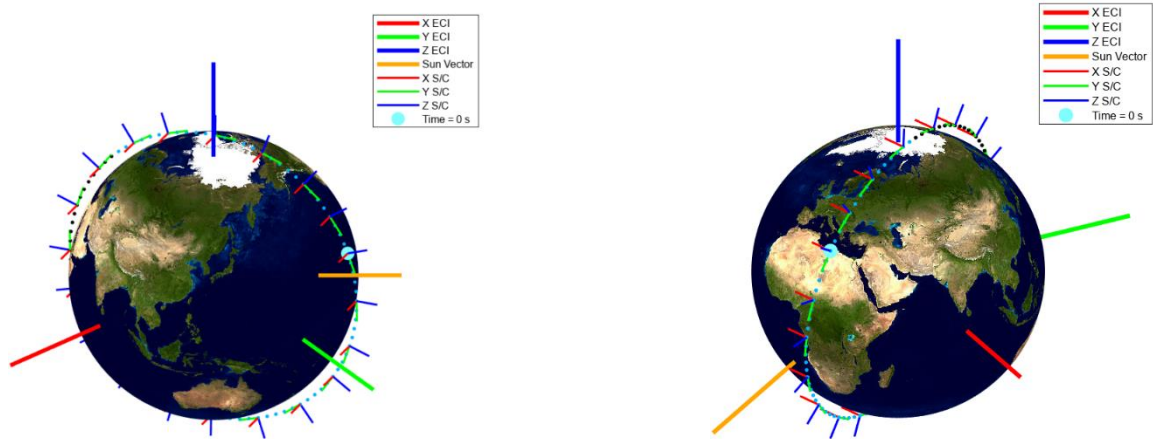


Figure 87: Cold Case Orbit (left), Hot Case Orbit (right)

Figure 20 collects the simulation data used for the analysis in the two cases. In Table 20 are also reported the S/C attitudes, which in the early stages of the project were considered fixed. At a later stage, a time-varying attitude was used, derived from the trajectory analysis.

Name	Aphelion (Cold Case)	Perihelion (Hot Case)
Date/Time [GMT]	5 Jul 2023 00:00:00.000	2 Jan 2024 00:00:00.000
Semi-major Axis (km)	6900.533728	6879.903852
Eccentricity	0.001612	0.000392
Inclination (deg)	97.388	97.633
RAAN (deg)	297.476	117.232
Arg of Perigee (deg)	156.415	147.934
True Anomaly (deg)	40.592	249.338
Mean Anomaly (deg)	40.472	249.38
Solar Flux [W/m ²]	1322	1414
Albedo	0.25	0.4
Earth IR Flux [W/m ²]	218	243
Nadir Attitude	Z-	Z-
Velocity Attitude	Y+	Y+

Table 20: Cold case and Hot case environment and attitude data

The selected operative modes for the two case studies are presented below:

- Payload Hot Mode: Both buses onboard computers are active, and the sensor suite is active and collecting data. Both buses send four consecutive messages. The first three messages contain the same payload hopeful sentence in Italian, English, and Spanish, while the fourth message contains a telemetry packet made up of the system and the sensor suite telemetry data. The four messages are alternated between the two buses so that each bus sends one sequence every 2 minutes.
- Recharge Mode: Only the BUS 1 onboard computer is active, while BUS 2 is shut down. The sensing suite is active and collects sensor data. BUS 1 transmits telemetry packets which contain the system telemetry data, the payload telemetry data, and the sensing suite data every

2 minutes. This mode of operation is triggered automatically when the battery voltage goes below 11.4 V. This mode of operation is timed and automatically reverts to the previous operative mode when the timer of 11 hours runs out. Its duration is designed so that it reverts to the previous mode when the battery is at full charge.

In Table 21 there are the power consumption for the two operative modes with also the duty cycles for each different phase.

	Recharge Power ON [W]	Recharge Power OFF [W]	Recharge Duty Cycle ON [%]	Recharge Duty Cycle OFF [%]	Recharge Average Power [W]	Payload Hot Power ON [W]	Payload Hot Power OFF [W]	Payload Hot Duty Cycle ON [%]	Payload Hot Duty Cycle OFF [%]	Payload Hot Average Power [W]
ComSys1	3.5	0.1	0.2	99.8	0.1	3.5	0.1	3.4	96.6	0.2
ComSys2	0.3	0.1	100	0	0.3	3.5	0.1	3.4	96.6	0.2
DET	0	0	0	0	0	0	0	0	0	0
BackPlane	0.4	0	100	0	0.4	0.4	0	100	0	0.4
C&DH1	0.9	0	100	0	0.9	0.9	0	100	0	0.9
C&DH2	0	0	0	0	0	0.9	0	100	0	0.9
Sensing Suite	0.2	0	100	0	0.2	0.2	0	100	0	0.2
Battery	0	0	0	0	0	0	0	0	0	0

Table 21: Recharge and Payload modes power consumption

Optical/Thermophysical Properties

The other inputs needed for the thermal analysis are the mechanical and optical properties of the components on the satellite. In particular, the optical properties of each surface finish are grouped in Table 22. In the early stages of the project, using S2T2 software, surface-weighted average optical properties were calculated, the formulas are given below [17]

$$\alpha_{effective} = \sum_{j=1}^N \left(\frac{A_j}{A_{total}} \right) \alpha_j \quad \varepsilon_{effective} = \sum_{j=1}^N \left(\frac{A_j}{A_{total}} \right) \varepsilon_j \quad (58)$$

Where A_j is the portion of external facing surface area of the j -th component [m^2], A_{total} is the sum of every A_j [m^2], α_j is the solar absorptivity of the single material and ε_j is the IR emissivity of the single material.

These formulas were used, for example, to determine the optical properties of the side faces of the satellite. They are formed by the overlapping of three different layers, the first being the structure, the second being the PCB, which represents the base of the solar panel, onto which the six solar cells are soldered, which constitute the third layer, as shown in Figure 88. This simplification was used

with S2T2 software and the first iteration of the model used on TD. For the last iteration performed on TD, individual layers were modelled as shown in the figure.

Material	Solar Absorptivity	IR Emissivity
Aluminium Alodine	0.42	0.06
SurTec 650	0.34	0.05
Black Anodized Aluminium	0.72	0.82
PCB Blue	0.89	0.9
Solar Cell	0.663705	0.85
PCB Green	0.88	0.7
Bare Aluminium	0.13	0.06

Table 22: Materials optical properties

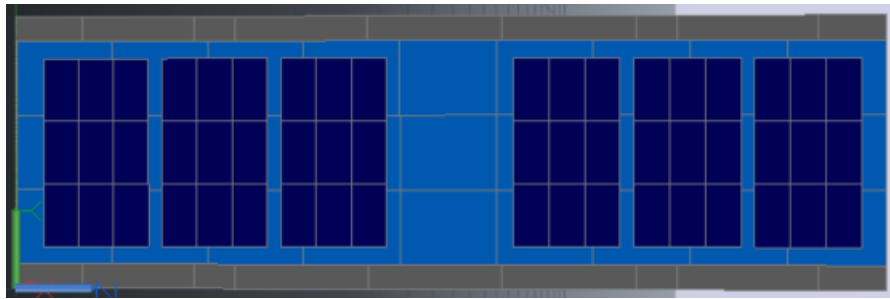


Figure 88: Lateral face with each layer modelled

The equation (59), which take into account the different materials of which the components are made, were used to calculate the average mechanical properties of each item [17]

$$cp_{effective} = \sum_{j=1}^N \left(\frac{M_j}{M_{total}} \right) cp_j \quad \rho_{effective} = \frac{M_{real}}{V_{modelled}} \quad (59)$$

Where cp_j is the specific heat of the j-th component material by which the item is made [W/m/K], M_j is the mass of the j-th component [kg], M_{total} is the total mass of the lumped component [kg], M_{real} is the real measured mass of the component [kg] and $V_{modelled}$ is the primitive shape volume by which the component is modelled [m^3].

Regarding thermal conductivity, it is necessary to distinguish between isotropic materials and laminated materials. In the isotropic materials k has a constant value over the whole volume, while in laminated materials, on the other hand, there are two different conductivities, k_{xy} pertains to in-plane conductivity, while k_z pertains to out-of-plane conductivity.

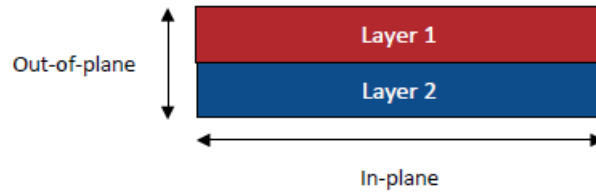


Figure 89: In-plane versus Out-plane

Specifically, all PCBs consist of one or more layers of FR4, two or more layers of copper, and two solder mask layers, which characterize the optical properties. The equation (60) was used to calculate these two conductivity contributions.

$$k_{xy\text{effective}} = \frac{1}{t_{total}} \sum_{j=1}^N (k_j t_j) \quad k_{z\text{effective}} = \frac{t_{total}}{\sum_{j=1}^N \left(\frac{t_j}{k_j} \right)} \quad (60)$$

Where t_j is the thickness of the j -th layer, t_{total} is the sum of every t_j [m], k_j is the isotropic conductivity of the j -th layer,

Table 23 contains the values of the mechanical properties of the single material used, while the Table 24 are reported the material assigned to each component.

Material	Conductivity (in plane) [W/m/K]	Conductivity (out of plane) [W/m/K]	Density [kg/m ³]	Specific Heat [J/kg/K]
Aluminium 7075	130	130	2810	960
PCB Skin	5.80903	0.2536	1952.2	586.146
PCB DET	28.8981	0.2699	2376.67	541.356
PCB Backplane	28.8981	0.2699	2376.67	541.356
PCB Sensing Suite	29.2744	0.27027	2383.58	540.758
PCB C&DH	28.8981	0.2699	2376.67	541.356
PCB ComSys	28.8981	0.2699	2376.67	541.356
Solar Cells	0.00329	60.6	5320	324
Battery	34.53	34.53	3002.28	667.37

Table 23: Material mechanical properties

Item	Material Properties	Surface Finishes
Structure	Aluminium 7575	SurTec 650
ComSys1	PCB ComSys	PCB White
ComSys2	PCB ComSys	PCB White
DET	PCB DET	PCB Green
BackPlane	PCB Back Plane	PCB Green
C&DH1	PCB C&DH	PCB Blue
C&DH2	PCB C&DH	PCB Blue
Sensing Suite	PCB Singer	PCB Green
Battery	Battery	SurTec 650 + PCB Blue (ZMAX=6)

Table 24: Materials assigned to each component

S2T2 Additional Conduction/Dissipations Plot

Once the various inputs for thermal analysis were collected, the next step was to create the satellite GMM. Table 25 groups the type of item used to model the geometries.

Component	Type of Item	Colour
Structure	Empty box	Light cyan
ComSys	Solar panel	Blue
DET	Board	Green
BackPlane	Board	Green
C&DH	Board	Magenta
Sensing Suite	Boards	Green
Battery	Parallelepiped	Yellow
Shelfs	Board	Black
Case of C&DH	Boards	White
Battery Stiffners	Parallelepiped	White

Table 25: Modelled items with S2T2

Conductive connections between the various components were modelled through node-to-node connections, as for the dissipations, they are evenly distributed over all the nodes of the item, as shown in Figure 90.

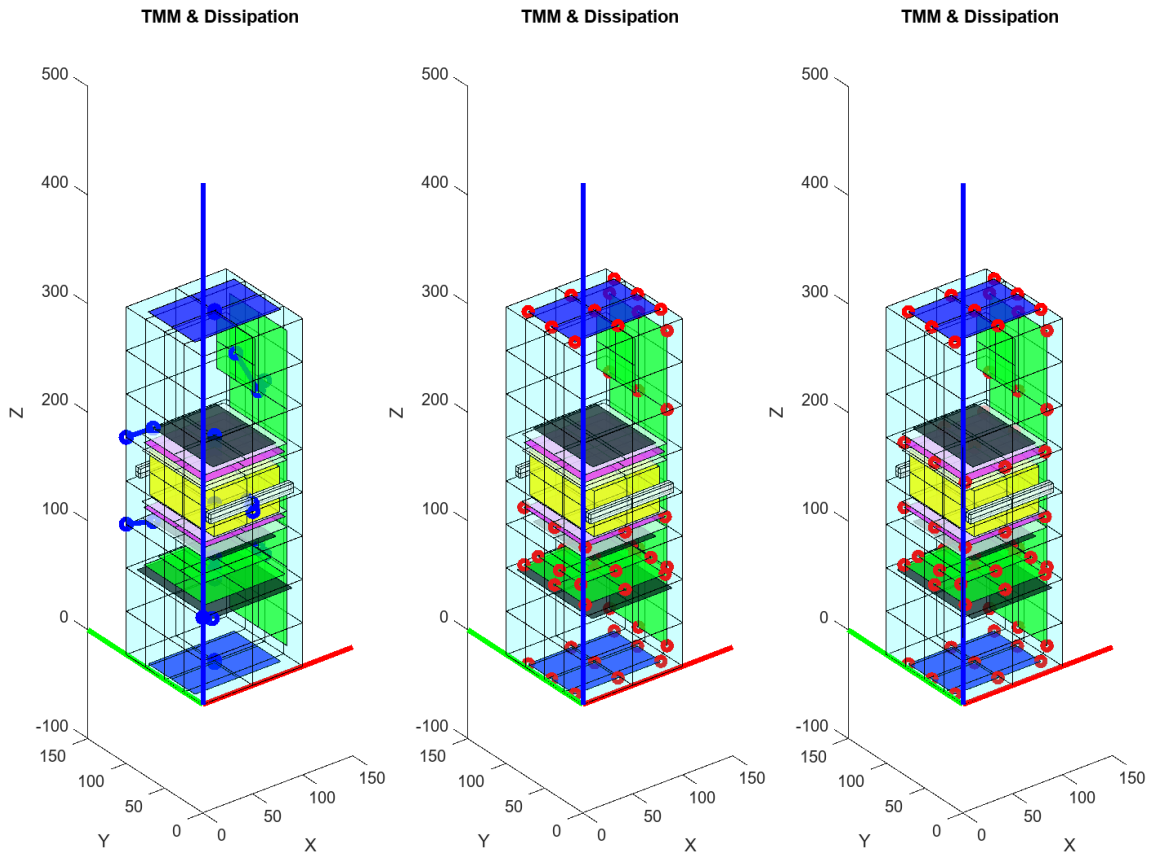


Figure 90: Additional conduction (left), Cold case dissipation (middle), Hot case dissipations (right)

Comments and Results

After the definition of all the inputs and the finalization of the thermal model in S2T2 two transient analysis, one for the hot case and one for the cold case were performed. To validate the S2T2 model and the new release of the S2T2 application in general a TD model was created, trying to keep this as close as possible to the representation of S2T2. In particular, the validation model created in TD, with respect to the S2T2 model, features:

- Same representation of internal components, using identical geometries, which naturally leads to the same number of nodes with the same distribution between the two models.
- Same optical and thermophysical properties, considering isotropic materials.
- Same representation of the structure and solar panels, using average uniform properties.
- Same Keplerian orbit.
- Same constant attitude.
- Same node-node conductors, with the same starting node, ending node and conductance value.
- Same constant, time-average heat loads.

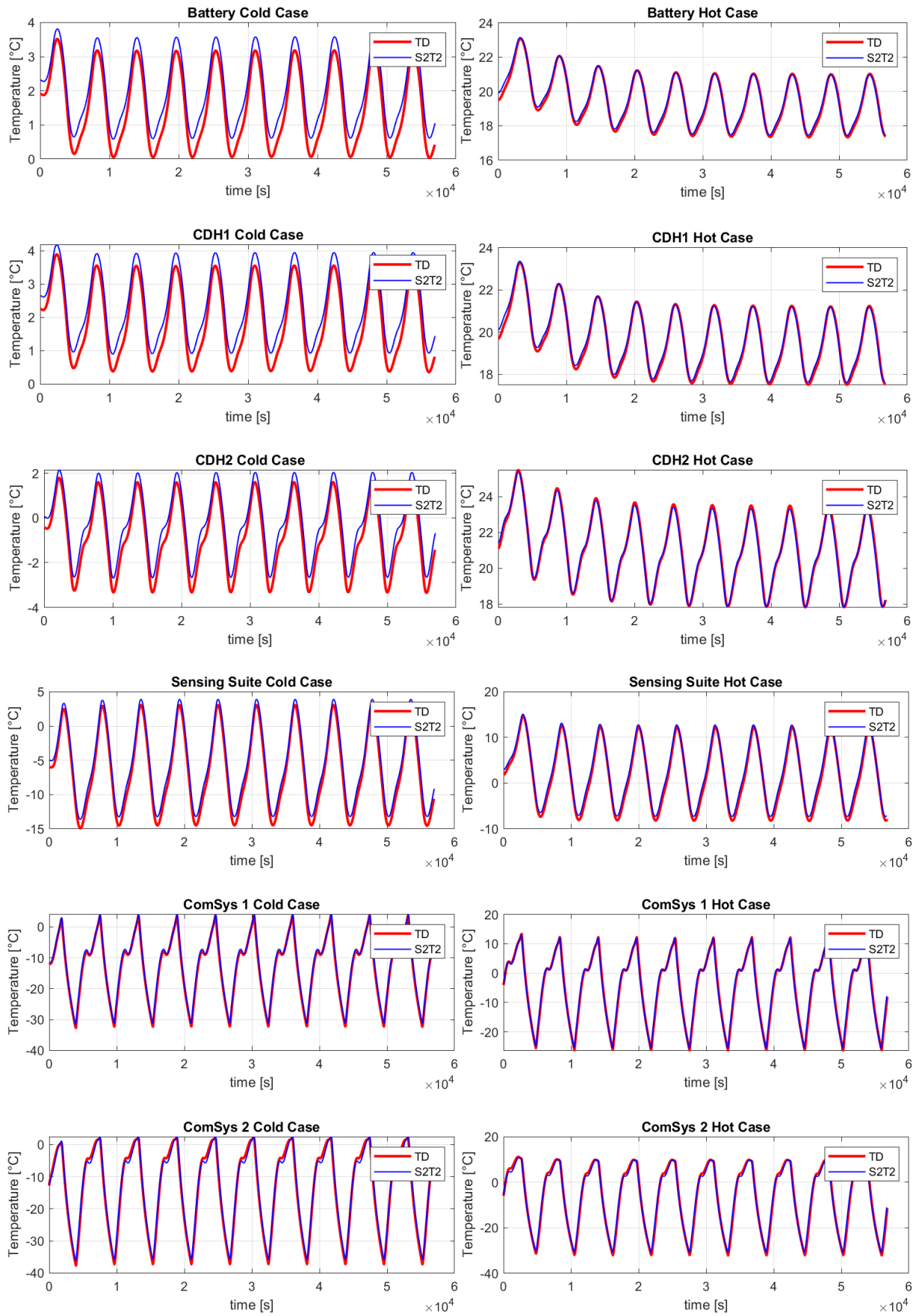


Figure 91: Temperature trends comparisons, cold case (left) and hot case (right)

The temperature trends of the most important component of SpeiSat, namely the battery, the two C&DHs, the Sensing Suite and the two ComSys, are displayed in Figure 91. The results from TD (red) and S2T2 (blue) are overlapped, to show the high level of accuracy reached by the new version of S2T2, even with the high number of geometries of SpeiSat, arranged in a complex configuration. The plots on the left are relative to the cold case, while the ones on the right are relative to the hot case.

For the majority of the components, it is evident from the plots that the temperatures never exceed a difference of 1°C, with the only exception of the two ComSys which, since they are external equipment they are subject to much wider oscillation and thus the difference between the two model increases too, reaching an absolute error of ~1.5°C. Overall another positive aspect of the S2T2 simulations is the shape of the temperature oscillation, which closely matches the one computed by the commercial software.

To better understand the entity of the accuracy of S2T2, Table 26 and Table 27 were generated. For each of the two cases and for each component are listed the minimum and maximum computed temperatures, with both software (excluding the first 5 orbits, to avoid convergence error from the steady-state temperatures). In the second to last column, the absolute error is given in terms of temperature difference between S2T2 and TD, while the last column contains the relative error of S2T2 with respect to TD, computed with the following formula:

$$Relative\ error = \left| \frac{\Delta T}{T_{max}^{TD} - T_{min}^{TD}} \right| \quad (61)$$

Cold Case					
Item		TD [°C]	S2T2 [°C]	ΔT [°C]	Relative Error [%]
Battery	Min	0.02	0.60	0.58	18.29
	Max	3.18	3.58	0.40	12.74
C&DH1	Min	0.36	0.93	0.57	17.71
	Max	3.55	3.94	0.39	12.27
C&DH2	Min	-3.35	-2.67	0.68	13.77
	Max	1.60	2.04	0.44	8.89
Sensing Suite	Min	-14.58	-13.27	1.31	7.42
	Max	3.08	3.92	0.84	4.74
ComSys1	Min	-32.32	-31.31	1.01	2.80
	Max	3.72	4.06	0.35	0.96
ComSys2	Min	-37.30	-35.83	1.47	3.73
	Max	2.07	2.39	0.33	0.83

Table 26: Cold case results

Hot Case					
Item		TD [°C]	S2T2 [°C]	ΔT [°C]	Relative Error [%]
Battery	Min	17.32	17.43	0.11	3.03
	Max	21.05	21.01	0.04	1.04
C&DH1	Min	17.50	17.60	0.11	2.82
	Max	21.27	21.23	0.04	1.13
C&DH2	Min	17.83	17.84	0.01	0.24
	Max	23.52	23.35	0.17	2.99
Sensing Suite	Min	-8.32	-7.38	0.93	4.54
	Max	12.26	12.75	0.49	2.40
ComSys1	Min	-26.33	-25.64	0.69	1.79
	Max	12.25	11.96	0.30	0.77
ComSys2	Min	-32.23	-30.98	1.24	2.95
	Max	9.90	9.85	0.05	0.11

Table 27: Hot case results

It is interesting to note that the magnitude of the absolute error depends on the amplitude of the oscillations: for many components the larger the oscillation is, the larger is the ΔT . This can be explained by considering the different approach for the computation of the environmental heat sources. The approximated method of S2T2 carries a small error in the value of incoming heat, mainly in the heat coming from the central planet. The effect of this error is then amplified when the components are subject to high temperature variations, for example when they are exposed to highly variable heat exchanges, such as the external components of a satellite in an orbit with an alternation between sunlight and eclipse, like SpeiSat.

On the other hand, the relative error depends heavily on the difference between the peaks and valleys of the temperature trends (it is the term on the denominator of the equation (61), thus it can be predicted that the items that experience lower oscillations will have, on average a higher relative error. This is the case of the Battery and C&DHs which have relative errors higher than 10%. Due to TCS design choices, those components were conductively insulated from the rest of the spacecraft, using low conductivity polymeric bushes and washers on the bolts; this has the beneficial effect of dampening the temperature oscillations, by limiting the amount of heat exchanged at their interfaces.

To further investigate the effects of this insulation on the internal components and the overall temperature distribution of the satellite, different heat maps were generated with S2T2. Below are displayed 3 different views (one for each row) of the same extreme instants: on the left the temperature distribution of the coldest instant of the cold case simulation is shown, while on the right the hottest moment of the hot case simulation is shown instead. The top two images are an external view of SpeiSat, the middle two show the internal components, while the bottom ones combine the internal view with the external one, using transparency.

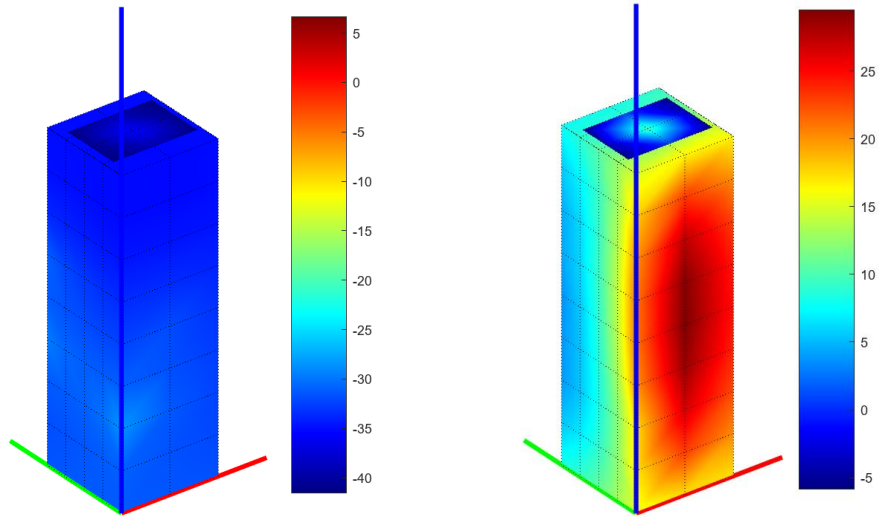


Figure 92: External heat map, Cold case (left), Hot case (right)

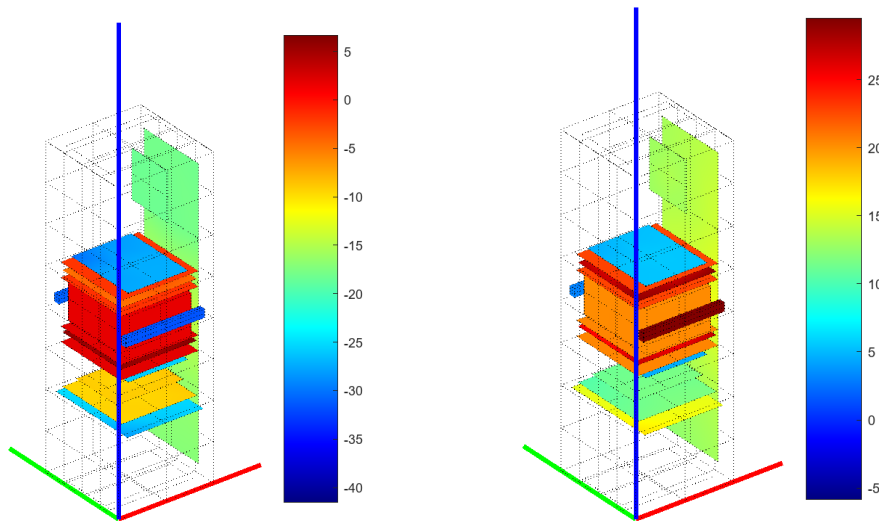


Figure 93: Internal heat map, Cold case (left), Hot case (right)

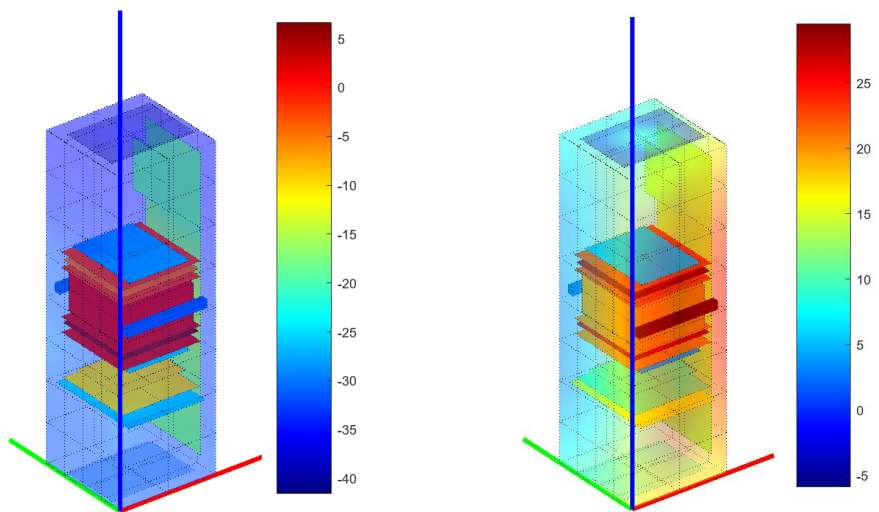


Figure 94: External-Internal view heat map, Cold case (left), Hot case (right)

From the previous heat maps it is clear how the insulation plays a fundamental role in keeping the temperature of the battery above its operative temperature: this was in fact the rationale behind the design choice. By creating a central hot “core” insulated from the rest, the heat produced by the C&DHs is used to keep the battery warm, always above 5°C without ever activating the integrated 4W battery heaters. To favour the heat transfer between the two C&DHs and the battery (which does not dissipate heat on its own) a conductive interface material, a thermal pad, was used to conductively couple these components.

Thanks to these design choices the temperatures of the battery, the C&DHs and the aluminium cases of the C&DHs reach similar values, with low amplitude oscillations. Instead, the bolted interfaces of these components with the primary structure experience high temperature differences because of the insulating elements used.

Design Optimization

To test the design optimization features of S2T2 several multi-objective optimization runs were performed. It was chosen to focus the analysis on the cold case rather than the hot case, because it was the most challenging one for SpeiSat, since the very first phases of the design. To optimize the TCS of the satellite different degrees of freedom were available:

- The optical properties of the structure of the satellite can be changed to a certain extent: the external faces chosen for the optimization were the Z+ and Z- faces of the satellite, where the surface finishes of the aluminum (α_{ext} and ϵ_{ext}) part can be selected with more freedom, the lateral faces instead are more constrained, due to the presence of solar panels and solar cells. For the internal side of the structure the emissivity ϵ_{int} was optimized for every one of the six faces. The bounds set for these variables are 0.05 (lower bound) and 0.9 (upper bound).
- The possibility of adding up to 2 additional conductance links, possibly in the form of thermal straps, was evaluated: the starting item group of the link was set to the following items: primary Structure, DET, Backplane, Sensing Suite, and Secondary Structure elements. The ending group was set to be equal to the starting group; the items were selected based on the ease of applying a thermal strap on them. The bounds for the cross-sectional area of the link were set to 0 mm² and 100 mm², while the conductivity of the link entered was 385 W/m/K (copper conductivity).
- Heater with constant power was optimized for the two coldest components, ComSys1 and ComSys2, as well as for the battery, to investigate how much power would be required to keep it near the middle of its operative range. The ComSys were allowed a maximum power of 1 W, while the batteries were set with 4 W of upper bound on heater power, to match the integrated heater power of the equipment available during design.

The optimizations were conducted with the three best-performing algorithms implemented in S2T2: RVEA, MOEA-D and RSA [6]. Each optimization was conducted with a maximum of 20000 cost function evaluation, a population size of 200, a time step of 60 s for the post processing of the optimal solutions and 5 orbits for the transient analysis. To avoid losing solutions in the post processing the pruning of the transient result exceeding operative temperature was not performed,

however, the post processing was conducted only on the solution on the final Pareto front of each optimization run.

After entering all the correct inputs, the optimization took about $400 \div 500$ s for each algorithm and ~ 30 s for each transient analysis performed in the post processing.

RVEA returned a total of 73 solutions, 48 of which were non-dominated across all algorithms, MOEA-D returned 200 solutions with 173 non-dominated ones and RSA outputted 200 solutions, 53 of which non-dominated. From this number it can be seen that every algorithm managed to find a niche of solutions where they were optimal with respect to the other, with MOEA-D covering the largest portion of the final Pareto front [6].

The three objectives (costs) to be optimized were the weighted average distance from optimal temperatures (defined as the midpoint between minimum and maximum operative temperatures), the total heater power and the total volume of copper needed to create the conductance links generated by the optimizers.

The following figure shows the distribution of solutions in the objective space, comparing the three algorithms. The visualization is 2-dimensional for ease of interpretation: the third objective, the volume of straps material is not plotted.

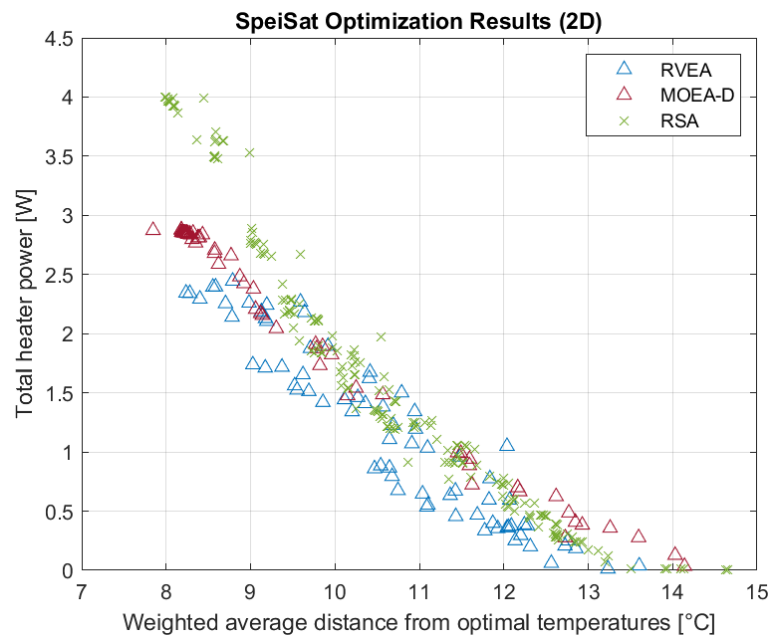


Figure 95: First two objectives (distance from optimal temperatures and total heater power) of the final Pareto fronts generated by RVEA, MOEA/D and RSA in the SpeiSat optimization.

Overall RVEA confirmed to be the best algorithm for finding a high fraction of non-dominated solutions, however in this optimization the cardinality of the final solution set of RVEA was lower

than the other, this could be fixed by tuning the parameters of the algorithms for the specific optimization performed.

MOEA-D found the highest number of non-dominated solutions, however, because it does not use reference vectors like the other two algorithms it suffers from a clustering perspective: many solutions are clumped in the top-left portion of the objective space and the general distribution is unbalanced, with many large holes towards the centre of the objective space.

RSA, thanks to its adaptive normalization of the archive and its extensive use of reference vectors managed to arrive at a highly balanced distribution, outperforming the other two algorithms in terms of spacing of the solutions. On the other hand, it showed more difficulty in advancing towards low costs solutions with respect to RVEA and MOEA-D and ended with a lower portion of dominated hypervolume.

To compare in a quantitative way the performance of the SpeiSat case study 4 performance metrics were evaluated: NR, IGD, MS and HR [6]. The results are displayed in the following table (note that while IGD and HR are better the lower the values are, for the other two, marked with an asterisk, the score should be maximized): The best values for each metric are highlighted in bold text.

	NR*	IGD	MS*	HR
RVEA	0.1745	0.08764	0.8152	0.02720
MOEA-D	0.6291	0.1170	0.6758	0.08957
RSA	0.1964	0.05769	0.9210	0.10684

Figure 96: Performance metrics of the 3 algorithms used in the SpeiSat design optimization.

The quantitative results confirm the observation made from the visual investigation of the objective space: MOEA-D won on the fraction of the final non-dominated solution, RVEA was the best one in terms of Hypervolume and Hypervolume Ratio, while RSA finished on top in terms of spacing and distribution, as witnessed by the MS and IGD metrics.

Two plots, in Figure 97 and Figure 98, of the final non-dominated design points, across all algorithms are given below, on the left there is a plot with the same axis as before, while on the right there is a 3d plot which simultaneously shows the cost of the optimal solution for each of the three objectives.

From the shape of the final Pareto front is clear that the front recalls a planar geometry or a line in the 2d case: this visually shows the effect of competing objectives: lower temperature differences are possible, but they often come with the cost of adding complexity in the system with the installation of thick thermal straps, or at the price of increasing the power dissipated on board by heaters-like elements.

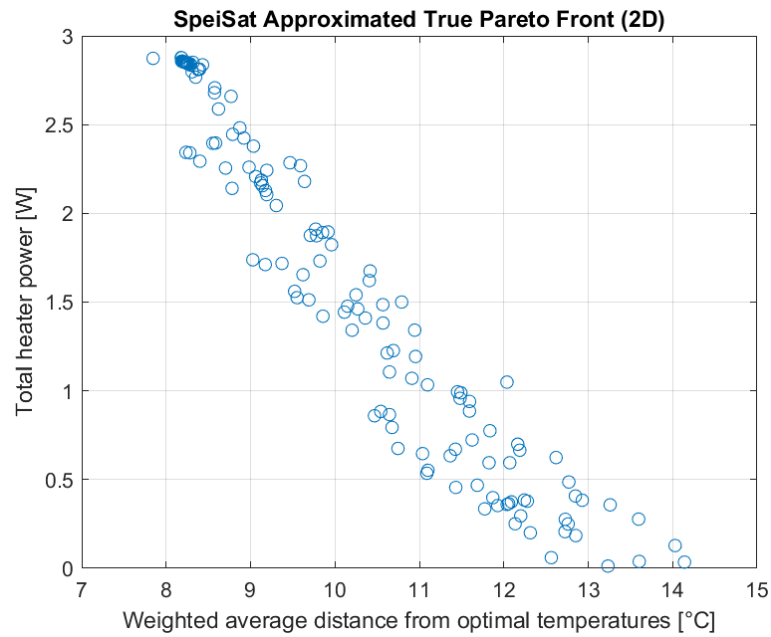


Figure 97: 2-dimensional representation of the approximated true Pareto front for the SpeiSat design optimization. The data points correspond to the non-dominated solutions, across all algorithms.

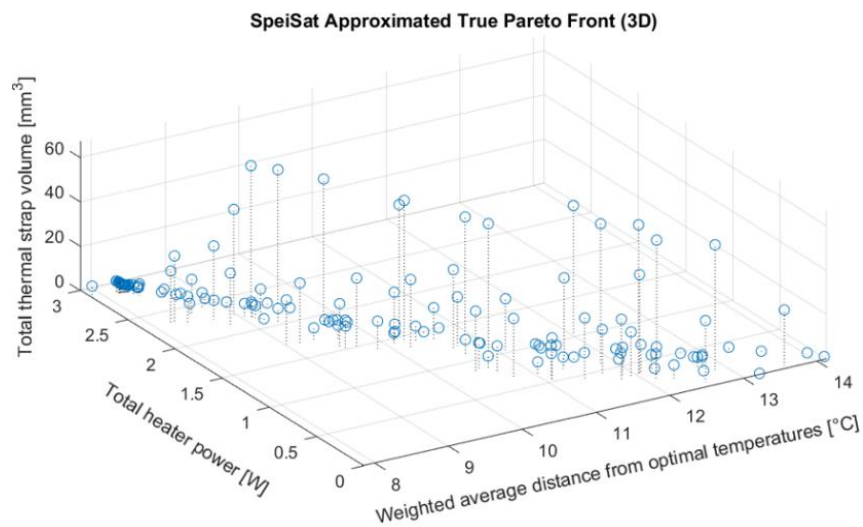


Figure 98: 3-dimensional representation of the approximated true Pareto front for the SpeiSat design optimization. The data points correspond to the non-dominated solutions, across all algorithms.

From the observation of the final Pareto front the final trade-off solution was selected: the rationale was to try and keep the temperature closer to the optimal ones, while also keeping the TCS design simple, which is crucial in the first phases of design. The design point chosen is a solution found by the RVEA algorithm, having cost [10.79, 1.501, 0.04427] for the first, second and third objectives respectively. The optimal properties of this solution are listed in Table 28.

Alpha Z-	Alpha Z+	Eps_int Y-	Eps_int X+	Eps_int Y+	Eps_int X-	Eps_int Z-	Eps_int Z+	Eps_ext Z-	Eps_ext Z+
0.8394	0.8954	0.0506	0.0572	0.2743	0.0540	0.1497	0.1264	0.0519	0.0528

Table 28: Optical properties of the final optimized solution chosen for SpeiSat.

On the external Z faces a material with high α/ϵ is needed, based on the numerical results ($\alpha/\epsilon = 16.17$ for the Z- face and $\alpha/\epsilon = 16.96$ for the Z+ face). The IR emissivity ϵ is desired to be low both on the internal and the external side of the structure, to retain as much heat as possible inside the satellite, increasing steady-state temperatures. In the real case, a surface finish of SurTec 650 was chosen to satisfy this need, the ratio α/ϵ of this treatment is high, with a BoL value of 6.8, which was determined to be enough to satisfy the requirement of SpeiSat. Regarding the heaters, the solution chosen had the following average powers:

Heater avg power [W] (ComSys1)	Heater avg power [W] (ComSys2)	Heater avg power [W] (Battery)
0.0553	0.903	0.542

Table 29: Heater power in the final optimized solution chosen for SpeiSat

ComSys1 basically is not heated, while ComSys2 has a high dissipation of almost 1 W. In the simulations ComSys2 is the coldest component because it is always oriented towards deep space and does not receive albedo or IR heat from the Earth, furthermore, the alternation of sunlight and eclipse mean that the temperature oscillations have very high amplitude. The choice to heat this component is thus well motivated: in the next design iterations of SpeiSat, to match this prediction one of the shunt resistors of the DET was placed on the Z+ face of the satellite, near ComSys2, to compensate for the low temperature. This design choice, however, is not without problems: although the shunt resistors of the DET have a peak power dissipation of around 1 W they are not actively controllable, and their operation depends on the power budget, in fact, they typically operate when the battery state of charge is near 100%. One situation in which they could be useful is at the end of the recharge operative mode of the cold case: after the battery reaches full capacity all the excess power available on board is dumped inside the satellite as heat, which is beneficial for SpeiSat which, on average, suffers more from cold scenarios.

Another reason because this solution from RVEA was chosen is the almost absence of thermal straps, the cross-sectional areas for the two links resulted, in fact, in 0 mm² and ~1 mm² which from the thermal point of view are negligible and can be ignored without significant repercussions. The absence of additional straps has also the favorable effect of simplifying the configuration and design of SpeiSat, which is a key aspect to manage complex systems such as the system engineering of spacecraft, and also fits well with the decision of keeping a central hotter core insulated from the rest of the spacecraft.

Final Iteration with TD and Results

The S2T2 software is designed to achieve a level of detail typical of the first two project phases, shown in Figure 99, namely phases A and B. However, since the Spei Satelles project aims to produce a working satellite, and then reach phase E exhibited in the same figure, it was necessary to produce a thermal model that was more accurate and faithful to reality.

To do this, it was necessary to use a tool that would allow a higher level of detail to be achieved. Table 30 shows all the upgrades that were implemented to reach the latest iteration of the SpeiSat thermal model.

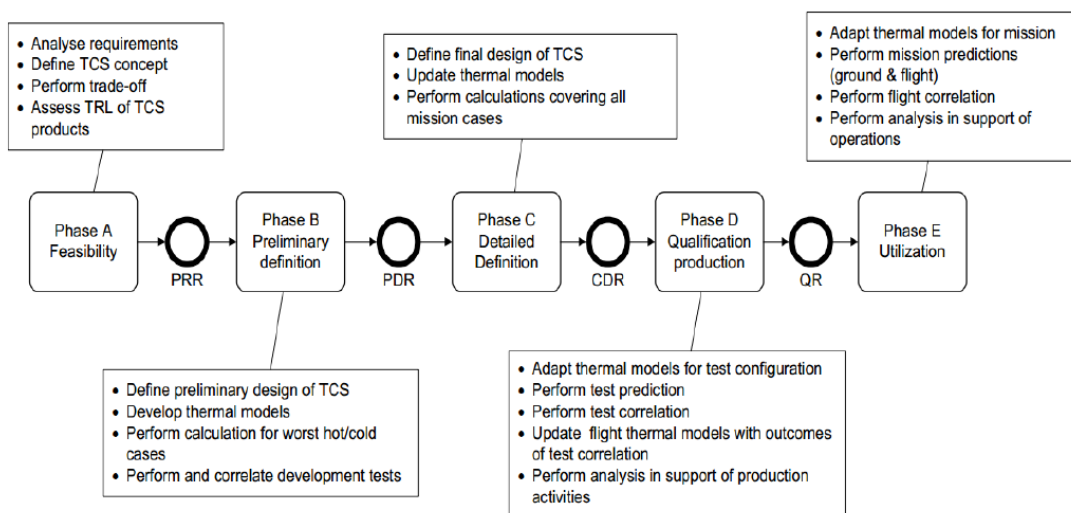


Figure 99: Project phases for TCS

The model shown in Figure 100 was then produced. With the exception of the ComSys, the other internal components maintained approximately the same geometry as the previous model, except for an increase in the number of nodes, especially regarding the battery model. Two new components, namely the antennas, were introduced, additionally, the model of the external structure was completely revised. For this last iteration in fact primary and secondary structures were made as similar as possible to the CAD model, as can be seen in Figure 101. The possibility of deactivating nodes was used to create openings in the structure, thus making the radiative exchange between solar panels and internal components more realistic. This same technique was also used to create the umbilical opening for the access port so that components such as the back plane could participate in radiative exchange outside of the satellite.

It was also possible to easily create contacts between different surfaces, meaning that conductive exchanges involving all nodes on a surface were created.

Another upgrade implemented on the latest model is the ability to create dissipations with a temporal law, to make the heating of some internal components more realistic.

Model	S2T2/First iteration	TD/Last iteration
View factors between central body/planet and external-facing surfaces	Computed with the analytical approximation of “Flat plate absorbing and emitting on one side” [ECSS-E-HB-31-01_Part3A, Section 5.2.1]	Computed with Monte Carlo Ray Tracing method
S/C self-shadowing	Computed by casting a single ray from every surface element towards the centre of the heat source	Computed with the Monte Carlo Ray Tracing method
Attitude	Nadir-Velocity pointing, constant	Derived from trajectory analysis
Orbit	Keplerian	Derived from trajectory analysis
Structure, solar panels and solar cells model	Box-like structure, with surface-average optical and mass/volume-average thermophysical properties, taking into account primary structure, solar panel PCBs and solar cells	Box-like structure, with deactivated nodes to model holes, rectangular geometries for each solar panel and each solar cell
Case of C&DHs	Simplified representation: only two rectangular geometries for each C&DH case	Detailed representation: two sides of the C&DH case modelled using two box-like geometries with one face open
Secondary structure	Simplified representation: only support elements of the main component are modelled	Detailed representation: many secondary structure features are modelled
ComSys boards	Modelled using only one rectangular geometry	Modelled using two rectangular geometries, one for the “octagonal” board and one for the transceiver board
Deployable antennas	Not modelled	Combination of 3D brick-like geometries and 2d rectangular geometries
Hole for umbilical access port	Not modelled	Modelled deactivating nodes of one of the solar panels
PCB material	Isotropic material, average properties of the laminate	Laminate material
Edge/centred nodes	Edge nodes for every component	Combination of edge nodes and centred nodes
Number of nodes	Total of 336 nodes	Total of 1273 nodes
Conductors and contactors	Only node-node conductor	Combination of node-node conductor and surface-surface contactor
Heat loads	Constant, time-averaged heat loads	Constant and time-dependent heat loads
Heaters	Not modelled	Battery heater, with proportional law, switch-on and switch-off temperatures

Table 30: Difference between S2T2 and TD models

TD also offers the opportunity to model heaters within the model, that is, to program certain nodes so that they dissipate a certain amount of power only if their temperature is below a certain threshold.

Whereas in S2T2 it is possible to model only Keplerian-type orbits or ideal orbits, TD, on the other hand, allows both orbit and attitude data to be imported from external tools; this involves both the ability to consider disturbances on the orbit but also to consider a more realistic attitude derived from more sophisticated models and analysis.

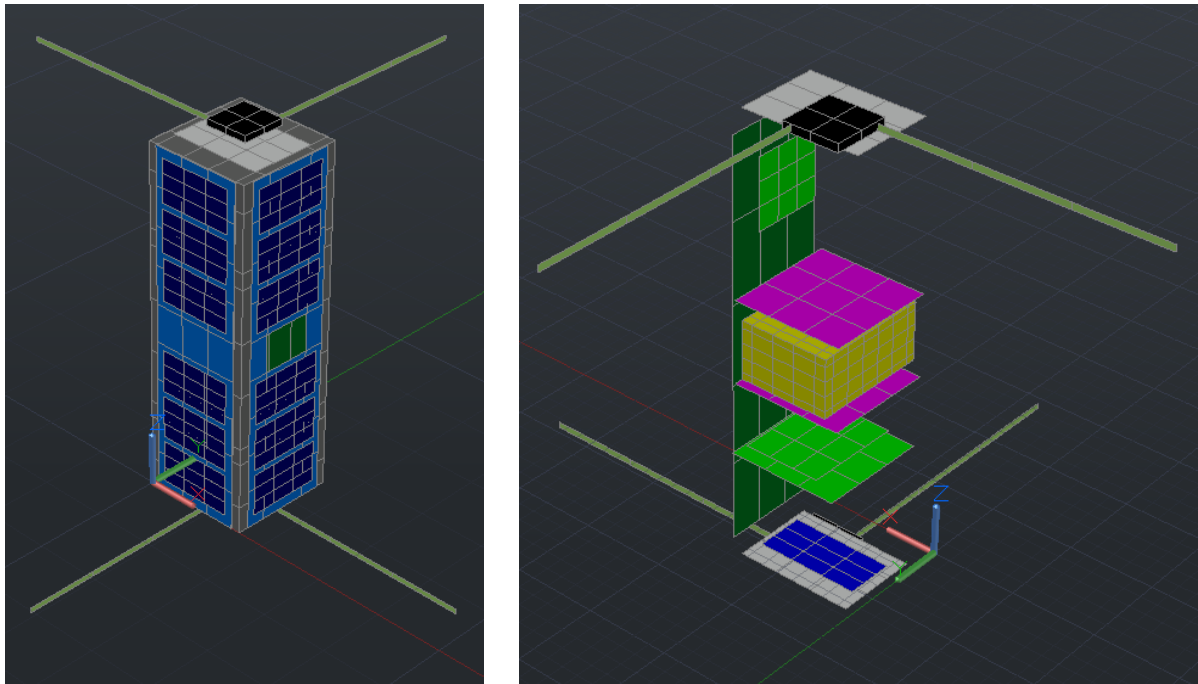


Figure 100: TD model for last iteration, external (left), internal (right)

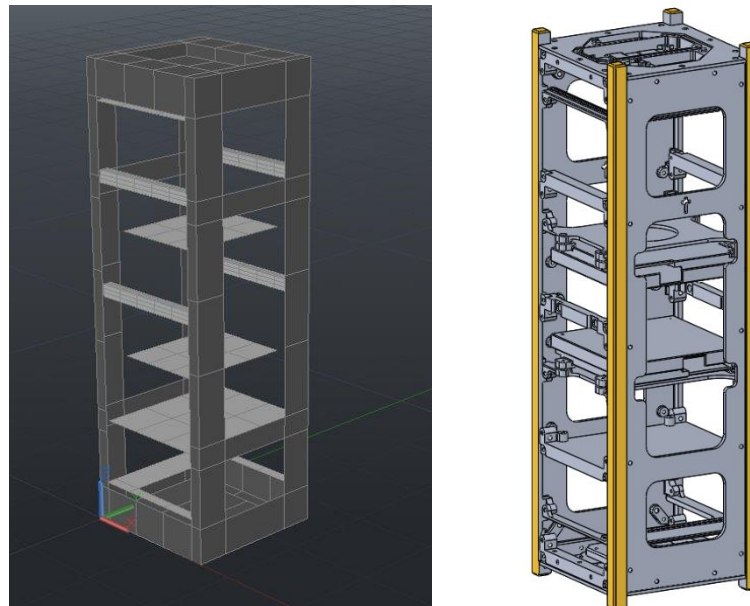


Figure 101: Comparison between TD model (left) and CAD model (right) regarding the primary and secondary structure

The results obtained for the hot case and the cold case are shown below.

A margin of 10°C (blue bar) was added to all temperature values obtained from the analyses (green bar) to consider all possible uncertainties in the model [16].

It can be seen that all components, both internal and external, fall within their operating ranges considering the margins as well, the only exception being the two ComSys for which considering the margins, the limit of the minor operating temperatures is exceeded.

It has not been possible to implement effective thermal control strategies for these components, the reasons are as follows, they are components that mainly face the outside of the satellite, so they dispose a lot of their heat in space. It has not been possible to vary the superficial finishes of these boards, which have a white colored solder mask, this greatly limits the absorption of radiation from the outside. In addition, they were only installed on the two smaller external faces namely the +Z and -Z faces, which having a very small surface area still limit the absorption of external radiation. Furthermore, given their remoteness from the other internal components it was not possible to create a thermal connection between them. All these reasons also imply very large temperature fluctuations. It can be observed from the temperature trend graphs, that in contrast to the other components, which have very narrow fluctuations, they have a temperature range in the order of 30°C.

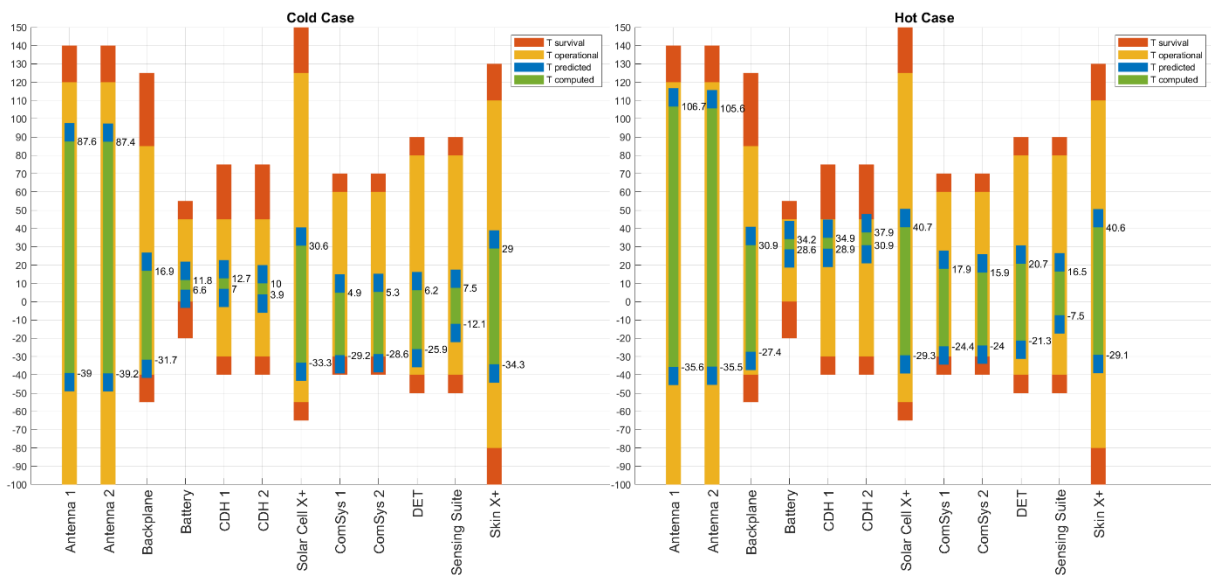


Figure 102: Min-Max results, Cold case (left), Hot case (right)

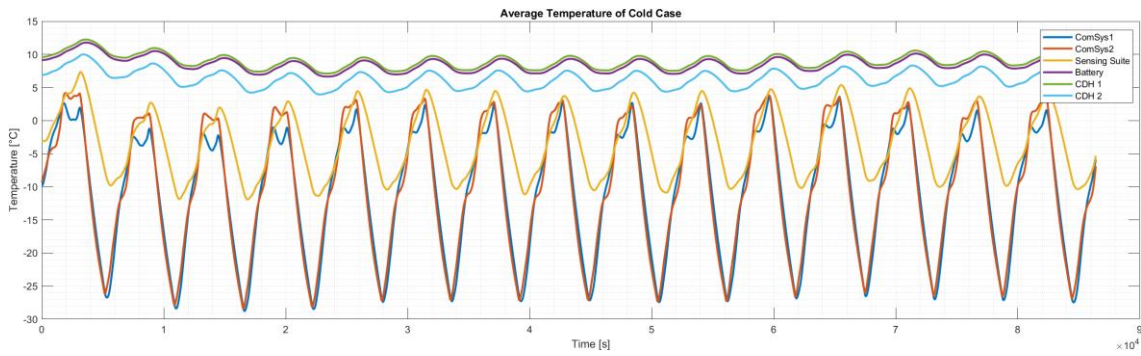


Figure 103: Temperature trends for Cold case

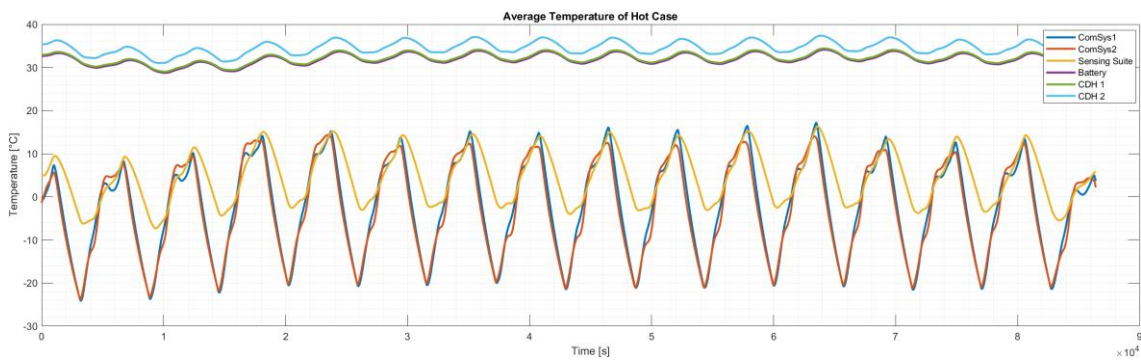


Figure 104: Temperature trends for Hot case

Data from Orbit

During the EOP many telemetries were collected and processed by the SPEI SATELLES Operations Team. The telemetry data includes the temperatures recorded by the Sensing Suite in the period from the 25th of June 2023 to the 18th of July 2023. Due to the discontinuous nature of the Ground Station operations, downlink requests were sent to SpeiSat on average 1 time a day, only for the passages with a high elevation over the MCC. During low elevation passages, the Ground Stations were kept in listening mode, recording the packets of telemetry data sent by SpeiSat every two minutes. This resulted in the availability of more than 250 data points which, once gathered together, were used to produce Figure 105. These graphs are not intended to be temperature trends, because the spacing of the telemetries is not uniform and many data points are clumped near the same time, but rather can be interpreted as scatter plots of the temperatures of the component during different instants of the EOP. Since the date of the cold case used for the numerical simulations is included in the aforementioned time period of telemetry availability, these last days of June and the first ones of July can be assumed as being a cold case for SpeiSat. The period, in fact, crosses the moment of minimum environmental heating, which corresponds to the aphelion of the Earth's orbit around the Sun.

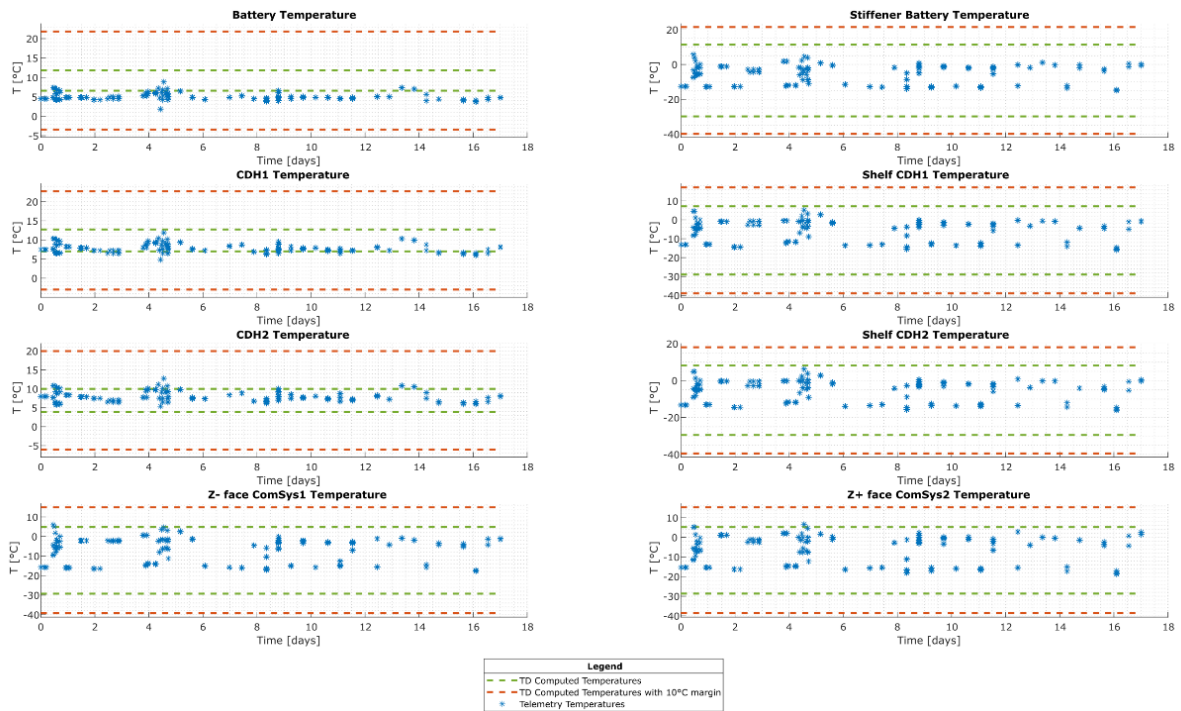


Figure 105: Telemetry data point received from SpeiSat between June 25, 2023, and July 12, 2023.

Although the environment of the first days of July matches the data used for the cold case, the satellite is not in the worst cold operative mode, the Recharge mode. During the EOP the satellite is power-positive, meaning that the total energy consumption on board is on average less than the energy generated by the solar panels: in this condition, the state of charge of the battery never falls below the threshold value, and thus the automating entering in Recharge mode is never triggered. The operative mode of SpeiSat for this period is more similar to the Payload Hot mode, because both C&DHs are active and the two buses transmit messages every two minutes, however, the telemetry packets are smaller than the packets needed to transmit mission data of the Payload Hot mode. For these reasons, the operative mode associated with the plots in terms of heat dissipation is intermediate between the Recharge mode and the Payload Hot mode.

In general, the temperatures of every component are inside the dashed lines of the plot, which represent the minimum and maximum temperature computed by numerical simulations (green dashed lines) with the addition of 10°C margins (red dashed lines), validating the predictions of the earlier design phases. The temperatures of the two ComSys, which were critical in the design phases, present narrower fluctuation with respect to the simulations, with most data points located between -15 °C and 5°C, validating the conservative assumptions made in the definition of the cold and hot case during the development of the numerical models.

Looking at the secondary structure elements, and in particular those where insulating elements were added to maintain the battery/C&DHs core warm; it is evident a temperature gap across the insulated bolted interfaces. Looking at the three graphs below, in Figure 106, Figure 107 Figure 108, it can be seen that for most data point this temperature discontinuity resulted in a gap between 5°C

and 15°C, which correlates well with the numerical simulations and prove that the design and final integration of the insulating element was performed correctly.

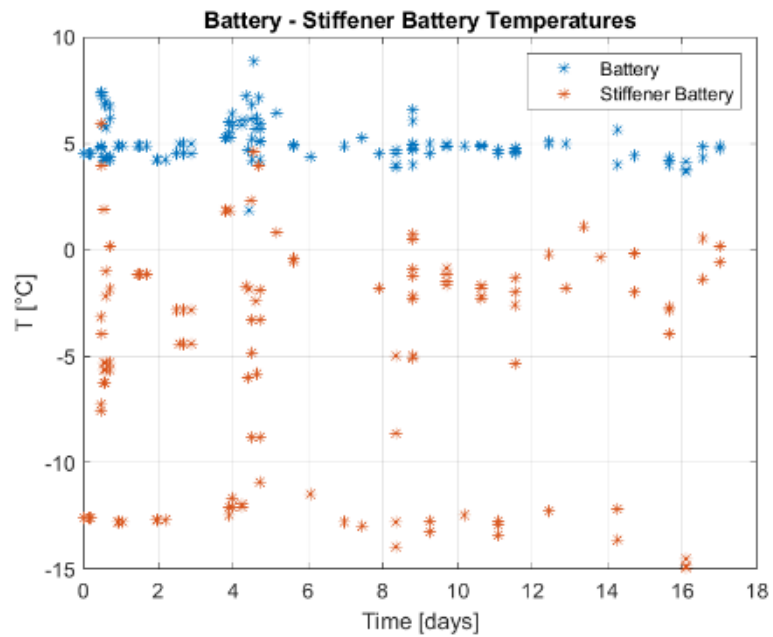


Figure 106: Temperature difference between the battery and its secondary structure support elements

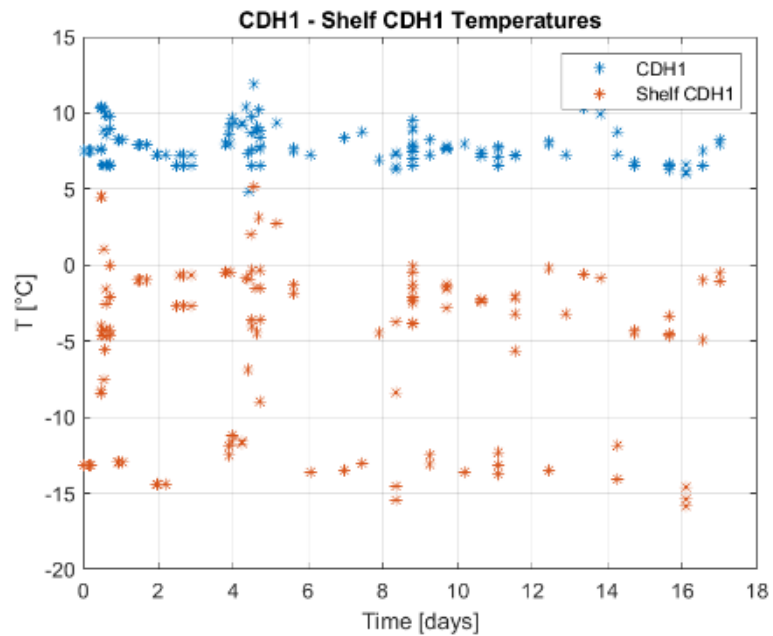


Figure 107: Temperature difference between C&DH1 and its secondary structure support element.

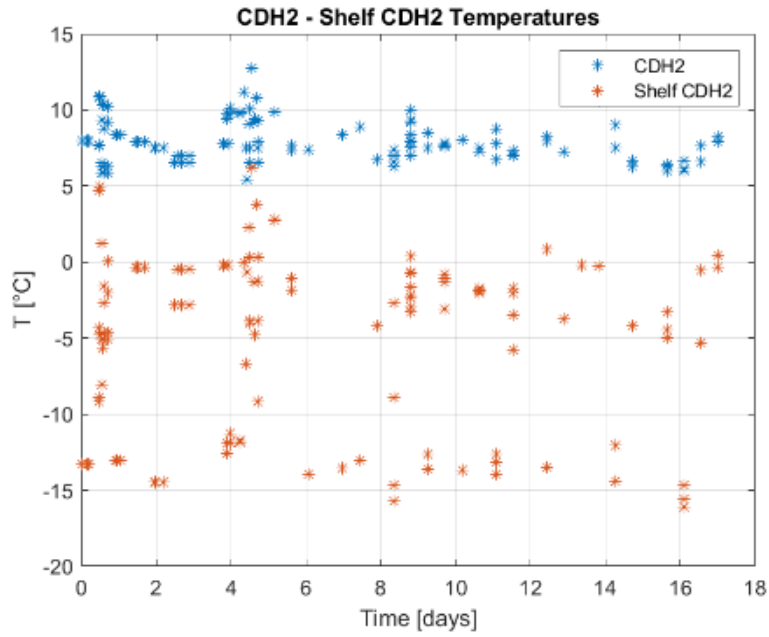


Figure 108: Temperature difference between C&DH2 and its secondary structure support element.

Figure 109, to Figure 112 instead illustrate the data collected by the Sensing Suite on July 13, 2023. The detailed temperature trends are overlaid over the green lines, which represent the items' minimum and maximum temperatures computed in TD for the cold case. Analogously to Figure 106 and Figure 108. The first three plots show the temperatures of the secondary structure element.

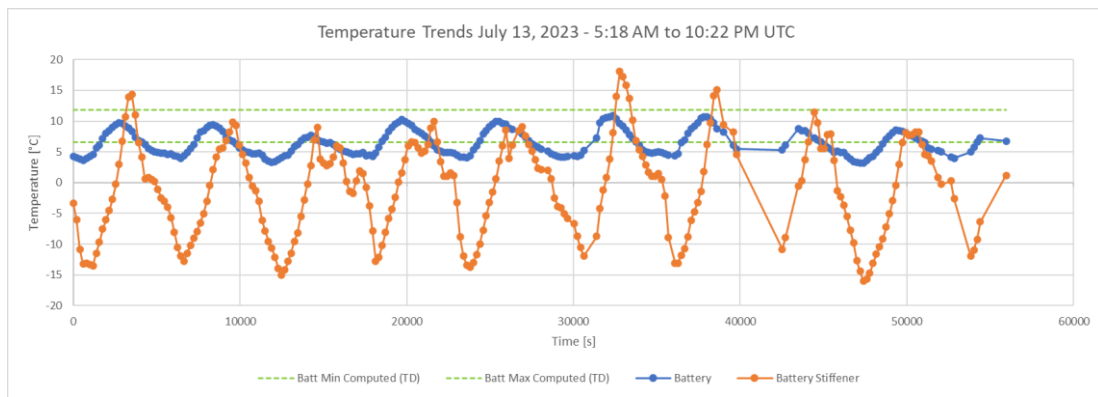


Figure 109: Temperature trends of SpeiSat Battery and Battery Stiffener. Data recorded on July 13, 2023.

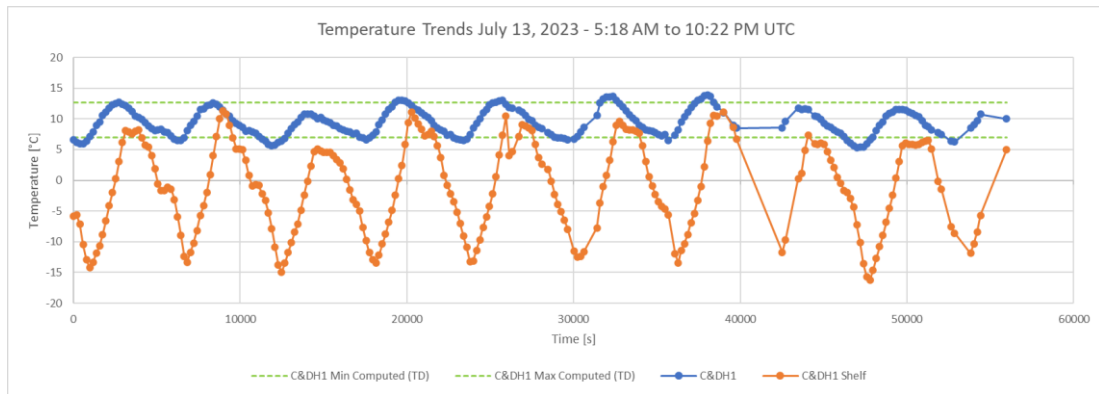


Figure 110: Temperature trends of SpeiSat C&DH1 and C&DH1 Shelf. Data recorded on July 13, 2023.

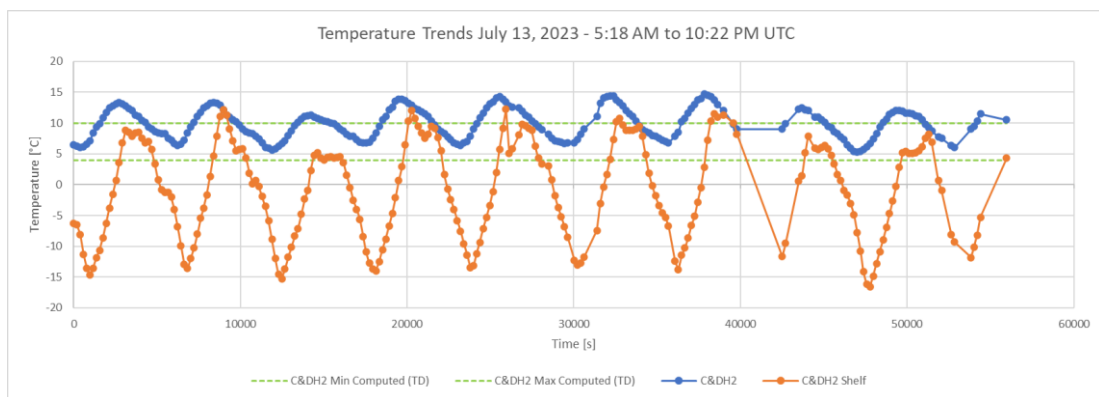


Figure 111: Temperature trends of SpeiSat C&DH2 and C&DH2 Shelf. Data recorded on July 13, 2023

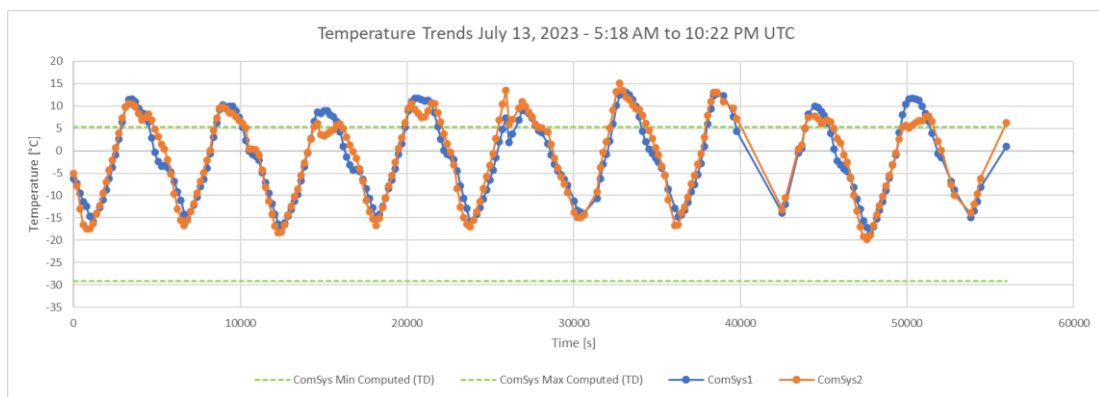


Figure 112: Temperature trends of SpeiSat ComSys1 and ComSys2. Data recorded on July 13, 2023

In the plots, more than 15 hours of temperature data are displayed, with a temporal resolution of about 195 seconds. From the oscillations, the effect of the alternation between eclipse and sunlight is clearly evident, however, the impact is not the same for all the items: the inner, most insulated components predictably present narrower fluctuations, while the external components and the

secondary structure show other minor fluctuation that adds up to the main one. The cause of these local, smaller oscillations, which vary from orbit to orbit and that were not present in the simulation, can be traced back to some secondary non-uniform effects such as the variable albedo and IR heating of different regions of the Earth but also on the attitude of the satellite, which cannot be easily predicted by numerical analysis given the passive stabilization system of SpeiSat. Overall, the shape of the trends is similar to the ones predicted using numerical simulation, however, the actual minimum and maximum temperature are different, mainly due to attitude discrepancies of the model compared to the real situation and also the different operative modes considered in TD for the cold case.

With more data points like the one plotted on the figures above, and with an approach that considers the temperatures recorded by all temperature sensors of SpeiSat, data like the one presented in these plots can be used to refine the thermal models of the satellite, improving the estimates of the conductance value across the mechanical interfaces (where contactors are simulated), the capacitance of the thermal nodes, and the heat fluxes between the components and from the environment. This technique is usually named *model correlation*.

One future development of the work presented in this thesis and the parallel one [6] is the complete model correlation of the GMM and TMM produced both using S2T2 and TD, improving the understanding of the thermal phenomena both on a qualitative extent and also on a quantitative level, gaining precious data which could be used in every design phase of future space missions.

Chapter 5

Conclusions

The aim of this thesis work was to develop software that would be useful to thermal engineers in the early stages of thermal control system design. The tool aims to be easy to use, streamlined, accessible, and it must allow reliable results to be obtained quickly.

As far as the GMM is concerned, it has been reworked with the aim of making the thermal models more accurate, but also and above all trying to make this section modular and easy to integrate with future work. The new geometries that can be implemented allow the user to create more complex models that are consistent with real systems, enabling a greater level of detail to be reached in the calculation of nodal temperatures. To enable the software to handle the new geometries, integration work was carried out on the entire code. In order to make the code modular, each geometry is treated separately from the others and with specific methods and functions, but producing consistently formatted outputs. This allows the GMM module to easily aggregate this data to create a global representation of the entire system.

The capacity of the software in the determination of radiative exchange has been improved by working on the algorithm that implements the MCRT method. It has been optimized both to considerably reduce the execution time and to improve the accuracy of the results. In fact, the software version that has been implemented makes it possible to preliminarily generate a large number of different models in a relatively short time, which was not possible with the previous version.

The implementation of the MCRT method with reflection makes it possible to achieve a very high level of detail and accuracy considering the project phase for which the software was designed.

Another important milestone was reached by improving the usability of the code. The graphical interface was improved so that the user is able to easily navigate through the various tabs, modify or integrate previous work sessions and, more generally, use the tool more fluidly and intuitively.

The software was then validated through, firstly, simple models useful for verifying the correct implementation of the changes made, then through a real case study, a preliminary thermal analysis carried out for the Spei Satelles mission. In order to verify that the software can also be used in professional contexts, the results obtained from S2T2 were compared with those obtained from one of the most widely used commercial software in the space industry, namely Thermal Desktop by C&R technologies.

Naturally, the models that can be implemented on S2T2 are consistent with the phase A project for which it was designed. As already mentioned in Chapter 4, concerning the case study, it still has

numerous limitations, and cannot replace a tool such as the one mentioned above for more advanced project phases.

The Spei Satelles space mission saw the author of this thesis and his colleague Davide Cosenza actively involved, in the roles of thermal analysts and thermal designers. This experience helped both of them to understand the main features that a tool such as S2T2 must have in order to be able to help the engineer in all phases of the project. Some of these have been implemented in the work of this thesis and that of his colleague Davide [6], others however have been listed below so that they can be the starting point for future work.

- New geometries could be added in the GMM tab: some candidates are cones, truncated cones or empty cylinders. The switch to curvilinear element needs to be investigated, to enhance the fidelity of the cylindrical and conical geometries. By taking advantage of the architecture created for the GMM and creating appropriate functions new geometries can be easily added.
- In this version of the software only the structure and solar panels can be considered as 'external elements', plus no 'box' type items are implemented as internal components. The idea is to let the user determine whether a component is internal or external.
- In some commercial software such as Thermal Desktop, there is the possibility of deactivating certain nodes in order to create openings in a component, such as in the case of the access port realized in the Spei Satelles model. This feature can be introduced by creating a dedicated function that post-processes the global data structures and eliminates the nodes to be deactivated.
- While the default computation of view factors with Gebhart's method has been greatly optimized, some work could still be done for the computation of view factors using the Monte Carlo Ray Tracing method with reflections. The idea is to apply vectorization techniques similar to what has been done for the calculation that uses Gebhart's method.
- The computation of planet-spacecraft view factors could be improved using the Monte Carlo Ray Tracing method, similar to what happens for the node-node radiative exchanges. This would further improve the accuracy of the results, at the cost of a lengthier evaluation of the environmental heat sources to do this, it is necessary to create a geometric model of the planet around which the satellite orbits.
- The spinning attitude, selectable in the Environment tab, needs a heavy rework: in the current state random angular velocities in the range of to are assigned to the body axes of the satellite when this option is selected. A more sensible approach would be to give the user the possibility to specify a constant angular velocity or an angular velocity temporal law for each axis of the spacecraft.
- When two case studies are considered simultaneously (hot and cold) there is a need of being able to specify different values for the solar constant, the albedo factor and the Earth IR irradiance, because usually the hot and cold case occurs in two different periods of the year. This could be implemented with three additional "edit field" components in the UI of the Environment tab.
- The possibility of specifying starting temperatures of the transient analysis could be added, instead of always using steady-state temperatures as the initial condition of the simulation.
- The introduction of time dependent heat load could be a great step towards closing the gap between S2T2 and other commercial software. With the same logic, the introduction of active heaters with user-defined control laws could greatly expand the capabilities of the software.

The main future developments concerning design optimization, the main topic of another thesis work, are summarized below. For greater clarity regarding the topics that follow, the reader is invited to consult Davide Cosenza's thesis [6].

- There are several methodologies available to enhance the performance of existing algorithms in multi-objective optimization. One promising possibility is the use of an ND-Tree-based update technique for online updating of a Pareto archive.
- Implementing vectorized evaluation of the cost function can significantly improve performance by testing multiple solutions simultaneously, leading to faster computation times.
- By applying hyperparameter optimization techniques, algorithms with tuneable parameters like RSA can be further improved by finding the best parameter values specific to the problem at hand.
- Additional decision-making algorithms, such as constraint programming and goal programming, can be implemented to select the best solution from the Pareto front, expanding beyond the weighted sum method.
- Another thermal control system (TCS) elements like cryo-coolers, heat switches, phase-change materials, thermal louvers, heat pipes, and variable emittance surfaces can be modelled and optimized in addition to the satellite structure.
- Including new objectives relevant to the additional TCS elements, such as the number of interfaces or thermal gradients, and higher-level metrics like cost and complexity, can provide a broader perspective for optimization.
- Pre-filtering unwanted solutions before the robustness analysis can help reduce computational waste, for example, by setting a threshold for the utility value or using explicit user-defined criteria.
- Single objective optimization, specifically targeting the optimization of optical properties in the satellite structure, can benefit from high-performance algorithms available in MATLAB libraries and scientific literature.
- The design variables in S2T2 can be expanded to optimize the optical properties of other components and not just limited to the satellite structure. Additionally, the specification of starting and ending groups for each thermal strap independently could be allowed.
- By optimizing for transient behaviour, rather than steady-state, more meaningful objectives can be achieved. However, the evaluation of the cost function for each solution would be computationally demanding, requiring compromises and trade-offs during the optimization process.

The following are some points, the development of which would lead to greater usability of the software.

- The improvement of data management can be explored: having the possibility to export all the satellite data in a spreadsheet, CSV or JSON format could improve the usability of S2T2 in contexts where multiple software is utilized. On the same line of thought, the data of S2T2 could also be ported automatically to other thermal analysis software like Thermal Desktop, using appropriate APIs.
- The UI of S2T2 can be further improved with more buttons and quality-of-life features. For example, more checks for the validity of the inputs could be added in order to help non-expert users. A help guide could even be added inside the software, to boost the accessibility of S2T2.

- For future source-code developments the utilization of a versioning software such as Git is strongly advised: a repository that is always up to date is the key to a long software life-cycle, opening the possibilities of reverting to previous versions, tracking changes and updating and managing multi-developer contributions.

As a final thought, the conclusion of the PhD thesis of the creator of S2T2 is recalled in this quote:

The author hopes that S2T2 can help the research community involved in thermal analysis and thermal management system design.

The author wishes the tool developed for this thesis work to be a valuable contribution to space research. He hopes that more and more people will become interested in this world and contribute to progress in this regard. Thermal analysis plays a key role in the success of space missions, and the author hopes that S2T2 will bring many young engineers closer to this way of thinking.

References

- [1] Nanosat.eu, «"Nanosat Database | Constellations, companies, technologies and more."» [Online]. Available: <https://www.nanosats.eu/>. [Consultato il giorno 4 April 2023].
- [2] NASA, State-of-the-Art Small Satellite Technology, Moffett Field, California, 2022.
- [3] BryceTech, «Smallsats by the Numbers,» 2022.
- [4] D. Calvi, Thermal analysis and control of small space platforms, Turin : Politecnico di Torino, 2021.
- [5] CalPoly, CubeSat Design Specification, San Luis Obispo, CA, 2022.
- [6] D. Cosenza, Development of a Tool for the Design and Verification of Thermal Control Systems of Small Sats, Turin: Politecnico di Torino, 2023.
- [7] D. G. Gillmore, Spacecraft Thermal Control Handbook.
- [8] NASA, Thermal Network Modelling Handbook, 2013.
- [9] J. R. Mahan, The Monte Carlo Ray-Trace method in radiation heat transfer and applied optics, 2018.
- [10] J. A. C. a. M. E. Korybalski, «"Algebraic methods for the calculation of,"» *Wärme- und Stoffübertragung*, vol. 7, n. 1, pp. 31-44, 1974.
- [11] B. Gebhart, «Surface temperature calculations in radiant surrounding of arbitrary complexity - for gray diffuse radiation,» *Int. J. Heat Mass Transf.*, vol. 3, n. 4, pp. 341-346, 1961.

- [12] S. L. Rickman, "“Form Factors , Grey Bodies and Radiation Conductances (Radks)”,”" in *Therm. Fluids Anal. Work. 2012*, Pasadena, California, 2012.
- [13] J. R. Wertz and W. J. Larson, *Space Mission Analysis and Design.*, 1992.
- [14] A. Ozturk, *Implementation of View Factor Model and Radiative Heat Transfer*, 2019.
- [15] MathWorks. [Online]. Available:
https://it.mathworks.com/help/matlab/matlab_prog/vectorization.html.
- [16] ECSS-E-HB-31-03A, Noorwijk, The Netherlands: ESA-ESTEC Requirement & Standards Division, 2016.